The Pennsylvania State University
The Graduate School

TOPOLOGY OPTIMIZATION OF FRAME STRUCTURES BASED ON HYSTERETIC FINITE ELEMENT MODELING

A Dissertation in
Civil Engineering
by
Navid Changizi

Submitted in Partial Fulfillment
of the Requirements
for the Degree of

Doctor of Philosophy

December 2020

The dissertation of Navid Changizi was reviewed and approved by the following:

Gordon P. Warn
Associate Professor of Civil and Environmental Engineering
Dissertation Advisor
Chair of Committee

Mary Frecker
Professor of Mechanical Engineering

Konstantinos Papakonstantinou
Assistant Professor of Civil and Environmental Engineering

Wen Shen
Professor of Mathematics

Patrick Fox
Professor of Civil and Environmental Engineering
Head of the Department of Civil and Environmental Engineering

Abstract

This dissertation presents new methods for the topology optimization of frame structures accounting material nonlinearity and dynamic excitation. Structural topology optimization is widely recognized as an important design tool in a wide range of disciplines including civil, aerospace, mechanical, materials, manufacturing and others. Its broad application is in part due to identifying solutions with efficient allocation of material for a given domain by combining structural mechanics with mathematical optimization. In the context of the optimal design of structures composed of truss or beam elements, studies reported in the literature have mostly considered linear-elastic material behavior. However, certain applications require consideration of the nonlinear response of the structural system, in particular under extreme loading such as earthquake or impact. Yet, the existing literature considering material nonlinearity has focused almost entirely on continuum structures whose solutions are not practical for civil structural applications. To this end, this work presents methods where the nonlinearity is incorporated into structural topology optimization through a hysteretic beam finite element model in which the inelastic deformations are governed by principles of mechanics in conjunction with, first order nonlinear ordinary differential equations, referred to as evolution equations. The evolution equations and the hysteretic variables govern the entire hysteretic response, including elastic, plastic, loading and unloading, and the approximation of the signum function with the hyperbolic tangent permits the derivation of analytical sensitivities that are differentiable everywhere and thus suitable for gradient-based optimization.

The concept is applied to design problems where the objective is to minimize the volume in the domain such that system-level displacement(s) satisfy a specified constraint value. This design problem is analogous to that of seismic design where volume is a proxy for cost and inelastic deformations are permitted, yet sufficient stiffness is required to limit the overall displacement of the system to a specified threshold to prevent loss of global stability. The methodology is first presented in the context of quasi-static loading, where the external forces are applied monotonically to evaluate the system's nonlinear response using a Newton solution scheme. The methodology is then extended to dynamic excitation, where the governing equations of motion and hysteretic evolution equations are combined and expressed as a system of first order ordinary differential equations, that is solved using the 4th order Runge-Kutta method. For the case of dynamic excitation, the displacement constraint is handled using a single p-norm which permits differentiation with respect to the design variables while returning an approximation of the maximum of the displacement response at specified node(s). Finally, for systems where the supplemental mass is much greater than the mass of the system itself, a Guyan type model condensation approach is integrated into the topology optimization to reduce the

system of governing equations of motion in terms of displacement degrees-of-freedom. For each design method, several numerical examples are defined and studied, to demonstrate the effectiveness of the proposed methods. Furthermore, to investigate optimality of the designs obtained from the proposed nonlinear design methods, comparable optimization problems assuming linear-elastic material are solved.

By employing the methodologies suggested in this dissertation, a closer modeling of actual structural system behavior is considered and incorporated in the topology optimization. It is suggested that these developments enable design solutions that are both efficient (minimal volume), practical, and yet robust to extreme loading.

Table of Contents

List of Figures

List of Tables

Acknowledgments

My deepest gratitude and appreciation to Professor Gordon P. Warn for giving me this wonderful opportunity to work in his group, and for being a great mentor to me. I am extremely thankful to get his guidance, encouragement, motivation and generous support throughout the course of my graduate studies at Pennsylvania State University.

I would like to express my thanks and appreciations to Professor Mary Frecker, Professor Konstantinos Papakonstantinou and Professor Wen Shen for their willingness to serve on my dissertation committee, and for their invaluable advice and suggestions that improved the quality of my dissertation.

This research was financially supported by National Science Foundation under Grant No. CMMI 135159. This support is gratefully acknowledged. All opinions, findings, and conclusions or recommendations expressed in this dissertation do not necessarily reflect the views of the National Science Foundation.

I would also like to thank my friends and colleagues for providing me with their delightful friendship and wonderful moments.

Last but not least, I am profoundly grateful to my family for their love, support, and continued encouragement over all these years.

Dedication

To my wife, Forough
To my mom and dad

Chapter 1
Introduction

1.1 Background

Topology optimization is widely recognized as an important design tool, owing to its ability to identify efficient material distribution within a domain, for a variety of design problems in a variety of disciplines (Sigmund, 1997; Guest and Prévost, 2006; Sigmund and Maute, 2013; Deaton and Grandhi, 2014). With respect to structural topology optimization, numerous contributions have been made, spanning from the earliest work by Miche (1904), to more recent developments and formulations to enable optimization, from analytical methods/solutions to computational frameworks (Bendsoe and Kikuchi, 1988; Ma et al., 1993; Sigmund, 1994; Duysinx and Bendsøe, 1998; Sigmund, 2007), stress-based formulations for linear-elastic quasi-static problems (Le et al., 2010; Holmberg et al., 2013; Changizi and Jalalpour, 2017b), and approaches to account for uncertainty in the system (Guest and Igusa, 2008; Jansen et al., 2013; Tootkaboni et al., 2012; Asadpoure et al., 2011) or in the external excitation (Kogiso et al., 2008; Dunning et al., 2011; Gomez and Spencer, 2019). Many of these prior contributions have been in the context of linear-elastic material behavior and/or static load conditions. However, such conditions are not always valid, for example for the optimal seismic design of structures (Lavan and Levy, 2005; Levy and Lavan, 2006; Aydin et al., 2007) or designing a system for crashworthiness (Pedersen, 2004; Patel et al., 2009; Cavazzuti et al., 2011), where nonlinearity, either material and/or geometric, and/or the dynamic nature of the excitation and response should be explicitly considered.

Over the past few decades, a considerable amount of literature has appeared in the area of topology optimization considering nonlinear behavior in recognition that particular design applications must account buckling and/or plasticity (Buhl et al., 2000; Yoon and Kim, 2005; Gomes and Senne, 2014; Nakshatrala et al., 2013; Li et al., 2017). In the context of material nonlinearity, some studies have investigated the topology optimization of systems with nonlinear-elastic and hyper-elastic materials in continuum (Klarbring and Strömberg, 2013; Luo et al., 2015) and discrete truss systems (Ramos and Paulino, 2015; Zhang et al., 2017b, 2018). However, the assumption of nonlinear elastic material behavior is not suitable when inelastic deformations are expected, specifically for designing frame structures to resist lateral and extreme loading conditions, thus the focus here is on plasticity. Much of the research on plasticity has focused in particular on continuum structures. For continuum structures and rate-independent plasticity, contributions have been made with respect to deriving analytical sensitivities for history dependent problems for finite strains under static conditions (Tortorelli, 1992; Maute et al., 1998; Nakshatrala et al., 2013; Zhang et al., 2017a), dynamic conditions (Nakshatrala and Tortorelli, 2015) and both material and kinematic nonlinearities (Kleiber, 1993; Tsay and Arora, 1990; Schwarz et al., 2001; Wallin et al., 2016). However, continuum solutions provide only a conceptual design for civil structures since these structures are typically constructed with discrete structural elements and standard shapes/cross-sections. Relative to continuum, there are few studies in the literature that have considered discrete/beam elements along with material nonlinearity. Pedersen (2003) proposed a formulation for rate-independent plasticity and beam elements using the ground structure approach (Dorn, 1964; Bendsoe and Sigmund, 2004), where the plasticity was concentrated at the end hinges of each element. Pedersen later extended this method using plastic zone model for crashworthiness design (Pedersen, 2004), however, some assumptions simplified the model of the beam element employed in these studies. More recently, there is a growing body of literature on damage resistant design of structures whereby continuum damage mechanics is integrated into topology optimization where constraints are introduced into the design problem to avoid material damage in the structure (James and Waisman, 2014, 2015; Li et al., 2017, 2018; Alberdi et al., 2018). Although entirely employed in the context of continuum structures, these concepts could be transferred to beam elements for damage resistant design of frame structures.

Extensions to dynamic problems, although to a lesser extent, can be found in the literature. Broadly speaking, there are two approaches, those that seek to maximize/minimize frequencies of the structural design and those that seek to minimize, or maximize, a measure of the structures response. With respect to the former, formulations have been suggested to maximize the fundamental eigen frequency (Díaaz and Kikuchi, 1992; Ma et al., 1993; Pedersen, 2000) and maximize the lowest eigen frequency (Ma et al., 1993, 1994; Bendsøe and Díaz, 1994). Approaches that seek to minimize the frequency response over a range of frequencies have also been suggested (Ma et al., 1993; Zhao et al., 2019). Although frequency-based approaches offer computational efficiency as they involve repetitive solution of the eigen value problem, thus avoiding the need for transient analysis, they are restricted to the case of linear-elastic material. In contrast, approaches have been suggested that seek to directly minimize, or maximize, measures of the system's response, e.g., displacement (Tcherniak, 2002; Liu et al., 2015; Zhao et al., 2018; Zhu et al., 2018) or a norm of displacements (Allahdadian et al., 2012; Allahdadian and Boroomand, 2016) for a given time-varying excitation. For such cases where analytical solutions are not available, transient analysis is performed, however, often modal super-position schemes are employed to obtain the time-varying response of the structural design that also rely on the linear-elastic material assumption. Direct integration, e.g., using Newmark's method, has been employed in some of the literature (Min et al., 1999; Allahdadian and Boroomand, 2016; Behrou and Guest, 2017), to obtain the time-varying response and while direct integration is not strictly limited to linear-elastic material, many of the studies have invoked the linear-elastic assumption. At least one study utilized a state-space solution scheme, whereby the system of n second order ordinary differential equations (ODEs) is transformed into a system of $2n$ first order ODEs for a linear-elastic continuum systems under white-noise excitation (Gomez and Spencer, 2019). Of course, time-varying approaches are more computationally demanding, in comparison to frequency-based approaches, due to the need to compute the response of the system at each time-step. There are fewer studies that have relaxed the linear-elastic assumption, and consider material nonlinearity for the topology optimization with dynamic excitation, e.g., Pedersen (2004); Nakshatrala and Tortorelli (2015), by employing traditional plasticity theory.

Topology optimization employing conventional plasticity theory typically rely on a nested Newton solution scheme, e.g., Pedersen (2003); Nakshatrala and Tortorelli (2015); Li et al. (2017), the inner loop for determining the state of stress (elastic vs plastic) throughout the domain and an outer loop to minimize a residual for the global system of equations at each step in the analysis. However, as reported in the literature, these Newton solution schemes are susceptible to divergence during the nonlinear analysis when implemented in an optimization framework (Pedersen, 2003). It is suggested that the divergence issue can be attributed to the minimal area/density elements oscillating between elastic and elasto-plastic stress states as a result of a displacement increment, and/or loss of definiteness of the global tangent stiffness matrix. Once the Newton scheme diverges, the optimization process ceases since the response of the system cannot be determined. Various ad-hoc strategies such as line search, increment reduction, relaxation of convergence criteria and hybrid approaches have been investigated to alleviate the divergence issue with limited success (Pedersen, 2003). Even if the Newton scheme does not diverge, there can be a significant accumulation of error in the sensitivities due to the approximation of the tangent stiffness matrix and tolerable error in the response quantities. Furthermore, the nested solution scheme complicates the analytical sensitivities, and also results in significant computational demand to analyze the response of a given design iteration in the optimization process.

1.2 Motivation

Hysteresis has been widely modeled using first order nonlinear ODEs, in particular in the context of uniaxial springs for structural and mechanical systems (Bouc, 1967; Wen, 1976). More recently, this concept has been elegantly extended to be consistent with multiaxial plasticity postulates and integrated into a finite element (FE) modeling framework to develop a hysteretic beam FE model (Triantafyllou and Koumousis, 2011, 2012b), and other elements, where nonlinearity is governed by hysteretic variables. These hysteretic variables evolve according to a set of smooth first order nonlinear ODEs, commonly referred to as evolution equations (Sivaselvan and Reinhorn, 2000; Triantafyllou and Koumousis, 2011). Similar to the displacement-based FE approach (Bathe, 2006), the hysteretic FE model uses displacement interpolation functions to relate nodal displacement DOF to internal strain fields within each element. However, unique to the hysteretic FE approach, are the addition of associated hysteretic interpolation functions that distribute the plasticity along the length of the element. Such modeling approach has several primary potential benefits in the context of topology optimization. First, the set of smooth nonlinear first order ODEs are able to describe the entire hysteresis, including elastic, plastic, loading and unloading branches through the values of the hysteretic degrees-of-freedom (DOF) that means a single set of expression can describe the entire evolution of the inelastic deformations without the need for a return mapping algorithm as with conventional plasticity theory, and, with a simple mathematical approximation, the set of evolution equations are differentiable everywhere facilitating the derivation of analytical gradients for the use of gradient-based optimization algorithms. Second, the evolution equations, being first order ODEs, can be combined with the governing dynamic equations of motion, expressed in state-space form, to facilitate dynamic analysis of the combined system of equations using general ODE solvers such as Runge–Kutta methods, thus avoiding the need for linearization of the Jacobian and associated iterations at each time step in the dynamic analysis as with a Newton type solution. Third, the hysteretic FE formulation offers computational efficiency due to the constant elastic stiffness and hysteretic matrix, which are evaluated only once at the outset of each nonlinear analysis, and do not require updating throughout. Furthermore, this means their associated sensitivities with respect to the design variable, also only need to be evaluated for each nonlinear analysis. Fourth, the constant beam element elastic stiffness matrix and hysteretic matrix also permit a Guyan type condensation to reduce the dynamic DOF only to those with associated mass, for problems where the supplemental mass is much greater than the mass of the system being designed. In these cases, it is reasonable to consider only the supplemental mass in the governing equations, to reduce the number of unknown displacement DOF in nonlinear analysis and to save the computational demand throughout the optimization process.

As previously mentioned, having constant system matrices (stiffness and hysteretic), comparative to conventional plasticity theory, the hysteretic FE allows using a solution scheme other than Newton's method to evaluate the response, e.g., Runge–Kutta method, that is not based on a linearized tangent stiffness matrix. For dynamic excitation, the entire system of governing equations, that is the dynamic equilibrium and evolution equations, can be straightforwardly expressed as a set of nonlinear ODEs that can be solved using general ODE solver methods. This avoids a potential source of divergence due to the linearization of the tangent stiffness matrix and iterations at each step in the analysis as with the Newton method. Furthermore, owing to the smooth transition from elastic to plastic with the hysteretic FE approach, there should not be any oscillation of the stress state of minimal area elements due to displacement increments during the nonlinear analysis thus avoiding another potential source of divergence.

Because of these important beneficial features of the hysteretic FE, in this dissertation, new design methods are developed for topology optimization of frame structures composed of beam elements, where material inelasticity is modeled using a hysteretic beam FE formulation.

1.3 Research goals and scope

Accordingly, the main goal of this work is to integrate hysteretic FE modeling with topology optimization to develop and demonstrate new methods to obtain optimized designs of frame structures consist of beam elements considering material nonlinearity. Particularly, this dissertation develops new topology optimization design methods for: 1) quasi-static loading, 2) dynamic base excitation and 3) dynamic base excitation with model condensation.

Specific objectives, for each design method, include: (i) define the optimization design problem, (ii) devise or adopt an appropriate solution scheme consistent with the design problem to evaluate the nonlinear system response, (iii) derive the analytical sensitivities with respect to design variables to employ gradient-based optimization efficiently and (iv) apply the method on couple of applications to demonstrate the utility and effectiveness.

In this work, all optimization design problems seek to minimize the volume of the structural system, that can be considered a proxy for the cost, while constraining the system-level displacement at certain predefined node(s) of the structure to a specified value. This design problem is analogous to seismic design where the goal is to design a system with the least cost that permits inelastic deformations while limiting the overall displacement of the system to a drift limit.

1.4 Organization of the dissertation

This dissertation is organized in six chapters. After this introductory chapter, the remaining Chapters cover the following topics in detail:

Chapter 2 provides background information on the hysteretic model and the uniaxial hysteretic law, followed by multiaxial non-interaction and multiaxial interaction material models, and integration with the beam FE method.

Chapter 3 presents the design method for topology optimization of nonlinear frame structures for quasi-static loading condition. A Newton type solution scheme is developed, and a minimum volume design problem subject to a system level displacement constraint is proposed. Sensitivities with respect to design variables are obtained through direct differentiation and numerical examples are provided to demonstrate effectiveness of the proposed method.

Chapter 4 considers design of nonlinear frame structures for dynamic excitation with the developed sensitivities with respect to design variables, and proposes a design problem to minimize the volume subject to a system-level maximum displacement constraint at certain locations in the domain. The equilibrium and evolution equations are combined and expressed as a system of first order ODEs using state-space format, and the unknown DOF are solved using the 4th order Runge Kutta method. Several numerical examples are investigated, and optimized designs topology and performance are discussed.

Chapter 5 integrates the design method for dynamic excitation to consider a Guyan type condensation method. The discussion starts with the mathematical model for condensation, and design problem of minimum volume subject to a system-level displacement. Similarly, the unknown DOF are solved using the 4th order Runge Kutta method and sensitivities with respect to design variables are developed. Several numerical examples with different arrangements of the supplemental masses are presented and discussed.

Finally, **Chapter 6** summarizes the dissertation, lists the key finding and contributions, and discusses some directions for the future research.

Chapter 2 Hysteretic Finite Element Modelling

2.1 Overview

Hysteretic FE (Sivaselvan and Reinhorn, 2000; Triantafyllou and Koumousis, 2011) is a method for modeling structures in which the hysteretic response of the system is governed by mechanics principles in conjunction with first order, nonlinear ODEs, often referred to as hysteretic evolution equations. These hysteretic evolution equations were proposed to model the rate-independent hysteretic response of various natural (Bowman and Sans, 1985) and engineered systems, including structural elements (Song and Ellingwood, 1999; Foliente, 1995), base isolation devices (Constantinou et al., 1990; Ozbulut and Hurlebaus, 2011), dampers (Choi et al., 2001) and others. These hysteretic evolution equations have also been suggested for use in uniaxial stress-strain laws (Foliente, 1995) and later were extended to multi-dimensional plasticity (Sivaselvan and Reinhorn, 2000). More recently, Triantafyllou and Koumousis (2011, 2012b) extended the multi-dimensional plasticity framework further to develop a hysteretic displacement-based beam element, having capability of simulating beam behaviors. Triantafyllou and Koumousis have also suggested the multi-dimensional plasticity formulation utilizing hysteretic evolution equations for shell and solid elements (Triantafyllou and Koumousis, 2012a, 2014), herein we referred to these methods as hysteretic FE modeling.

This Chapter starts with the description of general hysteretic model, uniaxial hysteretic laws with evolution equations, and hysteretic model parameters. The discussion is followed by interaction of axial and bending moment, and a brief review of FE method for beam elements to model frame structures in topology optimization, for the benefit of remainder of the dissertation. Throughout this dissertation, a standard notation is followed, where boldface upper and lower case font denote matrix and vector quantities, respectively.

2.2 Hysteretic model

Hysteresis is a phenomenon observed in many fields of science (Vázquez et al., 1999; Angeli et al., 2004; Unger et al., 2014) and engineering (Bouc, 1967; Wen, 1976). Bouc (1967) introduced a smooth nonlinear ODE that was later extended by Wen (1976), to model the rate-independent response of hysteretic systems and is presented in Eq. (2.1a):

$$\dot{z} = \left(1 - |z|^n \left(\beta + \gamma \mathrm{sgn}\left(\dot{u}z\right)\right)\right)\dot{u} \tag{2.1a}$$

$$\frac{dz}{du} = \left(1 - |z|^n \left(\beta + \gamma \mathrm{sgn}\left(\dot{u}z\right)\right)\right), \tag{2.1b}$$

where z is the hysteretic variable, u is a dimensionless displacement, and n, β and γ are model parameters. The over dot indicates the derivative with respect to time. The hysteretic variable, z, ranges in value according to $-1 < z < 1$ depending on the displacement. Parameter n controls the smoothness of the transition from the elastic to inelastic region and must be greater than zero, and $\mathrm{sgn}(\cdot)$ is the signum function. Parameters β and γ control the relationship between the loading and unloading stiffness. Specifying the following constraints of $\beta + \gamma = 1$ and $-\gamma \leq \beta \leq \gamma$ for model parameters β and γ have been shown to result in a thermodynamically admissible model (Erlicher and Point, 2004) and are adopted in this study. To illustrate how the hysteretic evolution equations permit the smooth transition from elastic to inelastic branches, Eq. (2.1a) is divided by du/dt, the result of which is shown in Eq. (2.1b). When the value of z is small, the rate of change in z with respect to u is approximately equal to 1, meaning the system behaves as an elastic system. As the value of z approaches 1, with the constraint of $\beta + \gamma = 1$, the second term in the parentheses approaches 1 and the change in z with respect to u approaches zero. Hence, the hysteretic variable is no longer dependent on u, simulating inelastic behavior. Furthermore, when $\dot{u} > 0$, the change in z is proportional to $\dot{u}$ simulating 'loading', whereas when $\dot{u} < 0$, the change in z is proportional to the negative of $\dot{u}$ simulating 'unloading'. The values of β and γ are typically set equal to 0.5 resulting in equal loading and unloading stiffnesses as is common in metal materials such as steel.

More recently, these nonlinear ODEs have been suggested to describe the evolution of stress and strain for nonlinear FE modeling (Sivaselvan and Reinhorn, 2000; Triantafyllou and Koumousis, 2008, 2011, 2012a). In the subsequent sections, we present application of hysteretic model to describe material nonlinear behavior, specifically for beams.

2.3 Uniaxial hysteretic law

Assuming a prismatic beam element, the internal stress resultants are related to the strain and hysteretic deformation at a given point along the length of the beam element, x, according to hysteretic laws; for example for internal moment, the uniaxial hysteretic law is expressed as:

$$M(x) = \alpha_\phi EI\epsilon_\phi(x) + (1-\alpha_\phi)EIz_\phi(x), \tag{2.2}$$

where $M(x)$ corresponds to the resultant internal bending moment, $\epsilon_\phi(x)$ is the curvature and $z_\phi(x)$ is the hysteretic variable. Parameters E and I are the elastic modulus and moment of inertia of the beam element, respectively, whereas α_ϕ is ratio of post-elastic to elastic modulus for bending. The stress resultant in Eq. (2.2) can be viewed as the sum of two parallel components, the first represents the component contributing to the post-elastic kinematic hardening and the second is the nonlinear component simulating the hysteretic response. Analogous to the nonlinear relationship for dynamic systems governed by the hysteretic evolution equation shown in Eq. (2.1a), the hysteretic variable, $z_\phi(x)$ in Eq. (2.2), evolves according to a first order nonlinear ODE, commonly referred to as evolution equation, expressed as:

$$\dot{z}_\phi(x) = \left(1 - \left|\frac{M^h(x)}{M_c^h}\right|^n \left(\beta + \gamma \mathrm{sgn}\left(M^h(x)\dot{\epsilon}_\phi(x)\right)\right)\right)\dot{\epsilon}_\phi(x), \tag{2.3}$$

where $M^h(x)$ is the current hysteretic bending moment and M_c^h is the hysteretic bending moment capacity of the cross-section, as follows:

$$M^h(x) = (1-\alpha_\phi)EIz_\phi(x), \quad M_c^h = (1-\alpha_\phi)M_p, \tag{2.4}$$

where M_p stands for the plastic moment of a section. In Eq. (2.3), parameter n controls the transition between elastic and inelastic branches. In this study β and γ are both set equal to 0.5 that results in the loading and unloading branches having equal slope that is consistent with the stress-strain behavior of steel materials. As mentioned previously, one beneficial feature of hysteretic model is that the entire hysteretic response, whether loading, unloading, monotonic, or cyclic, is controlled by the evolution equation in (2.3). The evolution equation for axial deformation can be obtained by replacing moment variables with the appropriate axial variables and associated cross-sectional parameters, as presented in the subsequent subsection.

2.4 Non-interacting actions

Following the procedure described in Section 2.3 for a prismatic beam element, the internal axial force and bending moment at a given point x along the length of the element are given by the following set of hysteretic laws:

$$P(x) = \alpha_u Ea\epsilon_u(x) + (1-\alpha_u)Eaz_u(x) \tag{2.5a}$$

$$M(x) = \alpha_\phi EI\epsilon_\phi(x) + (1-\alpha_\phi)EIz_\phi(x), \tag{2.5b}$$

where $P(x)$ corresponds to axial force, α_u is the ratio of post-elastic to elastic modulus for axial force, a is the cross-sectional area, and $\epsilon_u(x)$ is the axial strain. Similarly, the first component in Eq. (2.5) contributes to the post-elastic kinematic hardening and the second component simulates the hysteretic behavior according to the hysteretic DOF ($z_u(x)$ and $z_\phi(x)$). The hysteretic DOF evolve according to a set of nonlinear ODEs (evolution equations) that for the axial deformation and curvature are expressed as:

$$\dot{z}_u(x) = \Big(1 - H_{1u}(x)H_{2u}(x)\Big)\dot{\epsilon}_u(x), \quad \dot{z}_\phi(x) = \Big(1 - H_{1\phi}(x)H_{2\phi}(x)\Big)\dot{\epsilon}_\phi(x), \tag{2.6}$$

where $H_{1u}(x)$ and $H_{1\phi}(x)$ are smooth functions given by:

$$H_{1u}(x) = \left|\frac{P^h(x)}{P_c^h}\right|^n, \quad H_{1\phi}(x) = \left|\frac{M^h(x)}{M_c^h}\right|^n. \tag{2.7}$$

In Eq. (2.7), $P^h(x)$ is the current hysteretic axial force and P_c^h is the hysteretic axial force capacity as follows:

$$P^h(x) = (1-\alpha_u)Eaz_u(x), \quad P_c^h = (1-\alpha_u)a\sigma_y, \tag{2.8}$$

where σ_y is the yield stress of the material. Furthermore, $H_{2u}(x)$ and $H_{2\phi}(x)$ in Eq. (2.6) are Heaviside functions expressed as follows:

$$H_{2u}(x) = \gamma \mathrm{sgn}\Big(P^h(x)\dot{\epsilon}_u(x)\Big) + \beta, \quad H_{2\phi}(x) = \gamma \mathrm{sgn}\Big(M^h(x)\dot{\epsilon}_\phi(x)\Big) + \beta. \tag{2.9}$$

To consolidate the notation into more compact expressions, the hysteretic laws shown in Eq. (2.5) are expressed in matrix format as:

$$\mathbf{m}(x) = \boldsymbol{\alpha}\mathbf{D}\boldsymbol{\epsilon}(x) + (\mathbf{I}_{2\times 2} - \boldsymbol{\alpha})\,\mathbf{D}\mathbf{z}(x) \tag{2.10}$$

$$\boldsymbol{\epsilon}(x) = \left[\epsilon_u(x) \ \ \epsilon_\phi(x)\right]^T, \quad \mathbf{z}(x) = \left[z_u(x) \ \ z_\phi(x)\right]^T, \tag{2.11}$$

where the matrices $\boldsymbol{\alpha}$ and $\mathbf{D}$ are expressed as follows:

$$\boldsymbol{\alpha} = \begin{bmatrix} \alpha_u & 0 \\ 0 & \alpha_\phi \end{bmatrix}, \quad \mathbf{D} = \begin{bmatrix} Ea & 0 \\ 0 & EI \end{bmatrix}. \tag{2.12}$$

In Eq. (2.11), $\mathbf{I}$ is identity matrix, and the components of $\mathbf{m}(x)$ are arranged as $\mathbf{m}(x) = [P(x) \ \ M(x)]^T$. Similarly, the evolution equations shown in Eq. (2.6) are compactly expressed in matrix format as follows:

$$\dot{\mathbf{z}}(x) = \Big(\mathbf{I}_{2\times 2} - \mathbf{S}(x)\Big)\dot{\boldsymbol{\epsilon}}(x), \tag{2.13}$$

where the matrix $\mathbf{S}(x)$ is defined in Eq. (2.14).

$$\mathbf{S}(x) = \begin{bmatrix} H_{1u}(x)H_{2u}(x) & 0 \\ 0 & H_{1\phi}(x)H_{2\phi}(x) \end{bmatrix}. \tag{2.14}$$

2.5 Interaction

Interaction of the stress resultants at the cross-sectional level can be considered through the evolution equations and an appropriate yield/capacity function (Triantafyllou and Koumousis, 2011); for example, interaction between the axial force and bending moment which is a common interaction model for beam elements. To this end, the evolution equations are expressed in a compact matrix format as follows:

$$\dot{\mathbf{z}}(x) = \Big(\mathbf{I}_{2\times 2} - H_1(x)H_2(x)\mathbf{R}(x)\Big)\dot{\boldsymbol{\epsilon}}(x). \tag{2.15}$$

In Eq. (2.15), $H_1(x)$ is a smooth function ranging in values from [0,1] and $H_2(x)$ is a Heavyside function, expressed as:

$$H_1(x) = \left|\Phi(x) + 1\right|^n, \quad H_2(x) = \gamma \mathrm{sgn}\Big(\mathbf{m}^{h,T}(x)\dot{\boldsymbol{\epsilon}}(x)\Big) + \beta, \tag{2.16}$$

where $\mathbf{m}^h(x)$ is the vector of hysteretic forces and $\Phi(x)$ is the yield/capacity function. For this study, the Orbison criteria (Orbison et al., 1982) for I-shaped sections is adopted

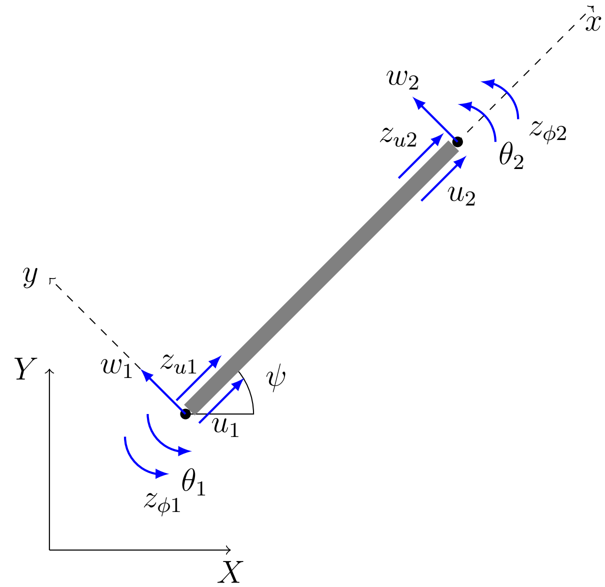

Figure 2.1: Illustration of a two-node beam element and corresponding displacement and hysteretic DOF

and its function form is:

$$\Phi(x) = 1.15P_r(x)^2 + M_r(x)^2 + 3.67P_r(x)^2M_r(x)^2 - 1, \tag{2.17}$$

where $P_r(x) = P^h(x)/P_c^h$ and $M_r(x) = M^h(x)/M_c^h$ represent the ratios of hysteretic force to hysteretic capacity for axial force and bending moment, respectively. The vector of hysteretic forces in Eq. 2.16 is arranged as $\mathbf{m}^h(x) = \left[P^h(x) \;\; M^h(x)\right]^T$. Last, $\mathbf{R}(x)$ in Eq. (2.15) is the interaction matrix and is expressed as:

$$\mathbf{R}(x) = \left(\left(\frac{\partial\Phi(x)}{\partial\mathbf{m}^h(x)}\right)^T \mathbf{D}\frac{\partial\Phi(x)}{\partial\mathbf{m}^h(x)}\right)^{-1}\left(\frac{\partial\Phi(x)}{\partial\mathbf{m}^h(x)}\left(\frac{\partial\Phi(x)}{\partial\mathbf{m}^h(x)}\right)^T\mathbf{D}\right), \tag{2.18}$$

where $\partial\Phi(x)/\partial\mathbf{m}^h(x)$ is the derivative of the yield function shown in Eq. (2.17) with respect to the hysteretic stress resultants given as:

$$\frac{\partial\Phi(x)}{\partial\mathbf{m}^h(x)} = \left[2.3\frac{P_r(x)}{P_c^h} + 7.34\frac{P_r(x)M_r(x)^2}{P_c^h} \quad 2\frac{M_r(x)}{M_c^h} + 7.34\frac{M_r(x)P_r(x)^2}{M_c^h}\right]^T. \tag{2.19}$$

2.6 Beam hysteretic FE model

To establish a topology optimization framework for frame structures considering material nonlinearity, an appropriate nonlinear beam FE model that is able to simulate the inelastic behavior of beam elements, including distributed plasticity and axial-moment interactions, is required. For this purpose, the hysteretic beam FE model suggested by Triantafyllou and Koumousis (2011, 2012b) is adopted. The hysteretic FE approach is the result of efforts by various researchers to extend hysteretic models governed by first order ODEs (Bouc, 1967; Baber and Wen, 1981; Baber and Noori, 1985; Foliente, 1995) beyond the uniaxial case toward established mechanics frameworks including an integrated hysteretic beam FE formulation (Triantafyllou and Koumousis, 2011, 2012b) and multiaxial plasticity (Casciati, 1989; Sivaselvan and Reinhorn, 2000). For a detailed derivation of the model formulations, beyond those presented in previous sections, the interested reader is referred to the aforementioned studies. The model employed here is based upon a two-node Euler-Bernoulli beam element as shown in Fig. 2.1. The beam element has six displacement DOF, namely longitudinal u, transverse w and rotation θ at each node. Unique to the hysteretic FE modeling approach are hysteretic DOF, $\mathbf{z}$, in addition to the traditional displacement DOF. For a nonlinear Euler-Bernoulli beam, there are two hysteretic DOF for each node, specifically z_u and z_ϕ corresponding to axial and curvature deformations, respectively. For compactness, a vector of the hysteretic variables, $\mathbf{z}$, is defined as a column vector assembly comprised of scalar hysteretic variables, z_u and z_ϕ. Thus, the element displacement and hysteretic DOF vectors can be defined as:

$$\mathbf{d}^{el} = \begin{bmatrix} u_1 & w_1 & \theta_1 & u_2 & w_2 & \theta_2 \end{bmatrix}^T \tag{2.20}$$

$$\mathbf{z}^{el} = \begin{bmatrix} z_{u1} & z_{\phi 1} & z_{u2} & z_{\phi 2} \end{bmatrix}^T, \tag{2.21}$$

where the superscripts e and l denote element-level and DOF with respect to the element local coordinates, respectively. Subscripts 1 and 2 correspond to the start and end nodes, respectively. Herein, superscripts e and l are only shown when necessary to differentiate element from system-level and local from global coordinates. As with the conventional displacement-based FE approach (Bathe, 2006), the hysteretic FE method employs displacement interpolation functions. However, there are additional hysteretic DOF and associated interpolation functions that differentiate the hysteretic FE modeling approach from the conventional FE formulations. Assuming no transverse force is applied between the element nodes, then applying the appropriate hysteretic boundary conditions, Eq. (2.21), the following interpolation functions for the hysteretic deformations at a point x, $z_u(x)$ and $z_\phi(x)$, corresponding to longitudinal and rotational deformations, respectively, are obtained as:

$$z_u(x) = \begin{bmatrix} 0.5 & 0.5 \end{bmatrix} \begin{bmatrix} z_{u1} \\ z_{u2} \end{bmatrix} \tag{2.22}$$

$$z_\phi(x) = \begin{bmatrix} 1 - \frac{x}{L} & \frac{x}{L} \end{bmatrix} \begin{bmatrix} z_{\phi 1} \\ z_{\phi 2} \end{bmatrix}, \tag{2.23}$$

where L is the length of element. The hysteretic interpolation functions in Eq. (2.22) serve to distribute the plasticity along the element length. Similar to the displacement-based FE approach, the conventional cubic displacement interpolation functions are used to relate nodal displacements to the local deformation fields at a given location along the length of the element but are omitted here for brevity (see Bathe (2006)). Following Triantafyllou and Koumousis (2012b), by substituting the interpolation functions and their derivatives into the variational principle of virtual work expressed for a given location along the length of the beam element, and then separating the elastic component from the hysteretic component, the following expression is obtained as:

$$(\delta \mathbf{d}^{el})^T \int_0^L \mathbf{B}^T \boldsymbol{\alpha} \mathbf{D} \mathbf{B} dx \cdot \mathbf{d}^{el} + (\delta \mathbf{d}^{el})^T \int_0^L \mathbf{B}^T \left(\mathbf{I}_{2\times 2} - \boldsymbol{\alpha} \right) \mathbf{D} \mathbf{N}_z dx \cdot \mathbf{z}^{el} = (\delta \mathbf{d}^{e,l})^T \mathbf{f}^{el}, \tag{2.24}$$

where $\mathbf{B}$ is the strain-displacement matrix derived from shape functions of the Euler-Bernoulli beam element as follows:

$$\mathbf{B} = \begin{bmatrix} \frac{-1}{L} & 0 & 0 & \frac{1}{L} & 0 & 0 \\ 0 & \frac{12x-6L}{L^3} & \frac{6x-4L}{L^2} & 0 & \frac{-12x+6L}{L^3} & \frac{6x-2L}{L^2} \end{bmatrix}, \tag{2.25}$$

and matrix $\mathbf{N}_z$ in Eq. (2.24), collects the hysteretic interpolation functions in (2.22) and expressed as:

$$\mathbf{N}_z = \begin{bmatrix} 0.5 & 0 & 0.5 & 0 \\ 0 & 1 - \frac{x}{L} & 0 & \frac{x}{L} \end{bmatrix}. \tag{2.26}$$

Performing the integration and enforcing the limits, the following element elastic stiffness matrix and hysteretic matrix are obtained:

$$\mathbf{K}^{el} = E \begin{bmatrix} \frac{\alpha_u a}{L} & 0 & 0 & \frac{-\alpha_u a}{L} & 0 & 0 \\ 0 & \frac{12\alpha_\phi I}{L^3} & \frac{6\alpha_\phi I}{L^2} & 0 & -\frac{12\alpha_\phi I}{L^3} & \frac{6\alpha_\phi I}{L^2} \\ 0 & \frac{6\alpha_\phi I}{L^2} & \frac{4\alpha_\phi I}{L} & 0 & -\frac{6\alpha_\phi I}{L^2} & \frac{2\alpha_\phi I}{L} \\ \frac{-\alpha_u a}{L} & 0 & 0 & \frac{\alpha_u a}{L} & 0 & 0 \\ 0 & -\frac{12\alpha_\phi I}{L^3} & -\frac{6\alpha_\phi I}{L^2} & 0 & \frac{12\alpha_\phi I}{L^3} & -\frac{6\alpha_\phi I}{L^2} \\ 0 & \frac{6\alpha_\phi I}{L^2} & \frac{2\alpha_\phi I}{L} & 0 & -\frac{6\alpha_\phi I}{L^2} & \frac{4\alpha_\phi I}{L} \end{bmatrix}, \tag{2.27}$$

$$\mathbf{H}^{el} = E \begin{bmatrix} \frac{(\alpha_u-1)a}{2} & 0 & \frac{(\alpha_u-1)a}{2} & 0 \\ 0 & \frac{(\alpha_\phi-1)I}{L} & 0 & -\frac{(\alpha_\phi-1)I}{L} \\ 0 & (\alpha_\phi - 1)I & 0 & 0 \\ -\frac{(\alpha_u-1)a}{2} & 0 & -\frac{(\alpha_u-1)a}{2} & 0 \\ 0 & -\frac{(\alpha_\phi-1)I}{L} & 0 & \frac{(\alpha_\phi-1)I}{L} \\ 0 & 0 & 0 & -(\alpha_\phi - 1)I \end{bmatrix}. \tag{2.28}$$

Importantly, as seen from the expressions in Eq. (2.28), both $\mathbf{K}^{el}$ and $\mathbf{H}^{el}$ are constant matrices and thus do not require updating throughout each nonlinear analysis. Instead of using a tangent stiffness matrix that is updated based on the state of deformation in the system, with the hysteretic FE approach, nonlinearity is represented by the hysteretic DOF, that, are updated at each force-step according to the chosen solution scheme. Both $\mathbf{K}^{el}$ and $\mathbf{H}^{el}$ must be transformed to the global coordinates system that is achieved through a straightforward transformation using following expressions:

$$\mathbf{K}^{e} = \mathbf{\Lambda}^T \mathbf{K}^{el} \mathbf{\Lambda}, \quad \mathbf{H}^{e} = \mathbf{\Lambda}^T \mathbf{H}^{el}, \tag{2.29}$$

where $\mathbf{\Lambda}$ is the conventional 6×6 transformation matrix for a beam element (Bathe, 2006). The global system-level matrices are assembled using Eq. (2.29) similar to the traditional FE method. Furthermore, the evolution equations are evaluated at the ends of a two node beam element, and are assembled for the structural system employing global quantities to relate $\dot{\mathbf{d}}$ to $\dot{\mathbf{z}}$ as follows:

$$\dot{\mathbf{z}} = \mathbf{U}\dot{\mathbf{d}}, \tag{2.30}$$

where $\mathbf{U}$ is assembled for non-interacting actions using Eq. (2.13) as follows:

$$\mathbf{U}^{el} = \Big(\mathbf{I}_{2\times 2} - \mathbf{S}\Big)\mathbf{B}\boldsymbol{\Lambda}, \tag{2.31}$$

and for the the interacting action using Eq. (2.15), that results in the following expression:

$$\mathbf{U}^{el} = \left(\mathbf{I}_{2\times 2} - H_1 H_2 \mathbf{R}\right)\mathbf{B}\boldsymbol{\Lambda}. \tag{2.32}$$

Chapter 3
Design Method for Quasi-Static Loading

3.1 Overview

This Chapter presents a method for the topology optimization of nonlinear structural systems composed of beam elements considering inelastic material behavior for quasi-static loading. The method combines topology optimization with a hysteretic FE approach to model the inelastic material behavior and as such original mathematical formulations and analytical sensitivities necessary to employ this modeling framework for the design of structural systems are presented. Nonlinear quasi-static analysis is carried out using the hysteretic beam FE model and an iterative solution scheme. As has been suggested by Kim et al. (2003) and Gömöry et al. (2009) for different applications, the hyperbolic tangent function is suggested as a suitable approximation of the signum function in the hysteretic evolution equations, to ensure these functions are continuous and differentiable everywhere. As such, analytical sensitivities with respect to the design variables, were derived by direct differentiation. Numerical design examples are presented for the quasi-static loading to demonstrate the utility of the method, where the objective of the design is to minimize the volume in a given domain for a given external force(s) subject to a specified system-level displacement constraint, e.g., drift limit (ASCE, 2017). For comparison, linear minimum compliance topology optimization problem is solved to obtain an optimal linear design solution using the optimal volume of the nonlinear design. Nonlinear analysis is performed with the linear minimum compliance design for the same level of external force and the results are compared to that of the nonlinear volume minimization design to study and illustrate the impact of explicitly considering material inelasticity in the optimization problem.

The remainder of this Chapter is organized as follows. Section 3.2 presents the overall methodology, beginning with a discussion of system level equilibrium equation using hysteretic FE modeling approach in the context of beam elements. This discussion is followed by the design formulation for topology optimization of structural systems considering material inelasticity, solution schemes for the nonlinear analysis and sensitivities with respect to the design variables. Section 3.3 presents the numerical examples and associated results whereby the methodology is applied for the design of structural systems for static excitation including discussions of the results and observations. Last, in Section 3.4, a summary and description of the main contribution and findings are provided.

3.2 Methodology

The proposed method consists of three main components, specifically nonlinear structural analysis employing the hysteretic beam FE model, the optimization problem formulation, and the corresponding sensitivities to facilitate gradient-based optimization. Evaluation of the performance of a given system relies on the nonlinear static analysis employing the hysteretic beam FE model and provides the basis for the derivation of the sensitivities, hence important details of the modeling approach are described in the subsequent section for the benefit of the remainder of the Chapter.

3.2.1 System level equation

Following Chapter 2, the element force-deformation relationship in local coordinates using the hysteretic FE can be expressed as:

$$\mathbf{K}^{el}\mathbf{d}^{el} + \mathbf{H}^{el}\mathbf{z}^{el} = \mathbf{f}^{el}. \tag{3.1}$$

After performing the appropriate transformations and assembling the structural system matrices, the global force-displacement equations are expressed as follows:

$$\mathbf{K}\mathbf{d} + \mathbf{H}\mathbf{z} = \mathbf{f}, \tag{3.2}$$

where $\mathbf{K}$ and $\mathbf{d}$ are the stiffness matrix and displacement vector, $\mathbf{H}$ and $\mathbf{z}$ are the hysteretic matrix and the hysteretic vector and $\mathbf{f}$ is a vector of external nodal forces all in global coordinates. Similar to other FE approaches, boundary conditions are imposed in the usual manner to get the system matrices via the typical direct stiffness assembly method. A benefit of this hysteretic FE modeling approach, in comparison to the more typical plasticity approach, is that the matrices $\mathbf{K}$ and $\mathbf{H}$ only need to be evaluated once, at the outset of the nonlinear analysis and otherwise remain constant. In this Chapter, non-interaction model is employed for material nonlinearity.

3.2.2 Optimization problem

The design problem considered here seeks to minimize the volume of the structural system subject to a system-level displacement constraint. Hence, having the nonlinear beam FE model, the volume minimization topology optimization problem considering material inelasticity subject to a system-level displacement constraint can be expressed as:

$$\begin{aligned}
\text{Find}: \quad & a_1, ..., a_N \\
\underset{\mathbf{a}}{\text{Minimize}}: \quad & v = \sum_{s=1}^{N} a_s L_s \\
\text{Subject to}: \quad & \mathbf{Kd} + \mathbf{Hz} = \mathbf{f} \\
& d_v \leq d^* \\
& 0 < \rho_{min} < a \leq \rho_{max},
\end{aligned} \tag{3.3}$$

where v is the volume in the domain, $\mathbf{a}$ is a vector of design variables representing the individual element cross sectional areas and N is the number of elements, for a given iteration in the optimization process. The equilibrium of the structural system and the system-level displacement are imposed as constraints which relate the response of the system to the design variables. Nonlinear static analysis is performed to establish equilibrium of the system and to evaluate the response, that is the displacement at a specific degree of freedom, d_v, here representing the system-level deformation which is constrained to a threshold value d^*. Each element's cross sectional area, a, is also constrained in Eq. (3.3) between ρ_{min} and ρ_{max}. The lower limit ρ_{min} avoids singularity during the optimization process and the upper limit is based on the maximum cross sectional area available for I-shaped sections in American Institute of Steel Construction (2015). An approach for relating the cross sectional area to other geometric properties for I-shaped cross sections suggested by Changizi and Jalalpour (2017b) is adopted in this study and the regression curves for the median range are used for the optimization process.

Gradient-based algorithms guide search efficiently. If gradients are available, then gradient-based algorithms have been shown to be computationally efficient relative to other optimization heuristics, e.g., evolutionary algorithms (Sigmund, 2011). Part of the motivation on using the hysteretic FE modeling includes derivability of analytical sensitivities that could translate into computational efficiency for topology optimization of nonlinear structures. However, with gradient-based algorithms, the design variables must be continuous and for most design problems, the global optima cannot be guaranteed.

3.2.2.1 Nonlinear analysis

Nonlinear static analysis is employed to determine the unknown DOF, $\mathbf{d}$ and $\mathbf{z}$. Each nonlinear static analysis is performed in a step-wise fashion until the specified external force value is attained. A challenge when material inelasticity is considered, is the iterative, and hence computationally expensive analysis, which is often required. For this study, a Newton solution scheme is devised for the hysteretic FE model and the nonlinear static analysis whereby for each force step, the unknowns (that is $\mathbf{d}$ and $\mathbf{z}$) are iteratively updated until the norm of the residual vector falls below the specified tolerance. For the solution scheme, the equilibrium equations and hysteretic evolution equations are combined into a single system of nonlinear equations whereby the unknown displacement and hysteretic DOF are simultaneously updated in an iterative manner. We define a vector, $\mathbf{x}_{i+1}^{j+1}$, that is an augmented set of unknowns containing $\mathbf{d}$ and $\mathbf{z}$ as:

$$\mathbf{x}_{i+1}^{j+1} = \begin{bmatrix} \mathbf{d}_{i+1}^{j+1} \\ \\ \mathbf{z}_{i+1}^{j+1} \end{bmatrix}, \tag{3.4}$$

where i represents the i^{th} force-step and j represents the j^{th} iteration of the i^{th} force step. For a given force step, the vector of unknowns, $\mathbf{x}_{i+1}^{j+1}$, is updated according to the following expression:

$$\mathbf{x}_{i+1}^{j+1} = \mathbf{x}_{i+1}^{j} - \mathbf{J}_v^{-1}\mathbf{g}_v, \tag{3.5}$$

where $\mathbf{J}_v$ and $\mathbf{g}_v$ are the Jacobian matrix and residual vector, respectively, each subsequently defined. For a quasi-static analysis, the rate of change of the hysteretic DOF and strains are approximated using the following backward difference expressions to convert the nonlinear ODEs into a set of algebraic expressions conducive to the Newton update:

$$\dot{\mathbf{z}}_{i+1}^{el} = \frac{\Delta\mathbf{z}^{el}}{\Delta t} = \frac{\mathbf{z}_{i+1}^{el} - \mathbf{z}_{i}^{el}}{\Delta t}, \quad \dot{\boldsymbol{\epsilon}}_{i+1} \quad = \frac{\Delta\boldsymbol{\epsilon}}{\Delta t} = \frac{\boldsymbol{\epsilon}_{i+1} - \boldsymbol{\epsilon}_{i}}{\Delta t}, \tag{3.6}$$

where Δt represents pseudo time that is, nevertheless, eliminated from the equations through algebra. Substituting Eq. (3.6) into Eq. (2.13), the following expression is obtained that relates $\mathbf{z}_{i+1}^{el}$ to $\boldsymbol{\epsilon}_{i+1}$ for the two node beam element:

$$\mathbf{z}_{i+1}^{el} = \mathbf{z}_{i}^{el} + \left(\mathbf{I}_{2\times 2} - \mathbf{S}\right)\Delta\boldsymbol{\epsilon}, \tag{3.7}$$

and the equilibrium equation at step $i+1$ can be written as:

$$\mathbf{K}\mathbf{d}_{i+1}^{j} + \mathbf{H}\mathbf{z}_{i+1}^{j} = \mathbf{f}_{i+1}. \tag{3.8}$$

Thus, the combined system of equations, that is the equilibrium equation (Eq.(3.8)) and the hysteretic evolution equations (Eq.(3.7)) is expressed compactly for the Newton update as:

$$\mathbf{g}_v = \mathbf{q}_v + \mathbf{T}_v\mathbf{x}_{i+1}^{j} - \mathbf{c}_v. \tag{3.9}$$

The quantities $\mathbf{q}_v$, $\mathbf{T}_v$ and $\mathbf{c}_v$ are expressed as follows:

$$\mathbf{q}_v = \begin{bmatrix} \mathbf{0}_{3r\times 1} \\ \mathbf{g}_z \end{bmatrix}, \quad \mathbf{T}_v = \begin{bmatrix} \mathbf{K} & \mathbf{H} \\ -\mathbf{R} & \mathbf{I}_{3r\times 4N} \end{bmatrix}, \quad \mathbf{c}_v = \begin{bmatrix} \mathbf{f}_{i+1} \\ \mathbf{g}_{zc} \end{bmatrix}, \tag{3.10}$$

where r is the number of nodes in the domain. The quantities $\mathbf{g}_z$, $\mathbf{R}$ and $\mathbf{g}_{zc}$ are assembly matrices of the following element level relations:

$$\mathbf{g}_z^e = \mathbf{S}\Delta\boldsymbol{\epsilon}, \quad \mathbf{R}^e = \mathbf{B}\boldsymbol{\Lambda}, \quad \mathbf{g}_{zc}^e = \mathbf{z}_i - \boldsymbol{\epsilon}_i, \tag{3.11}$$

Lastly, the Jacobian matrix, $\mathbf{J}_v$, is evaluated according to Eq. (3.12):

$$\frac{\partial \mathbf{g}_v}{\partial \mathbf{x}_{i+1}^{j}} = \mathbf{J}_v = \mathbf{T}_v + \mathbf{J}_{vn}, \tag{3.12}$$

where $\mathbf{J}_{vn}$ is evaluated using:

$$\mathbf{J}_{vn} = \begin{bmatrix} \mathbf{0}_{(3r)\times(3r+4N)} \\ \mathbf{J}_d \quad \mathbf{J}_z \end{bmatrix}, \tag{3.13}$$

where the matrices $\mathbf{J}_d$ and $\mathbf{J}_z$, are the assembly of the following vectors evaluated at each node, that results in a 2×2 matrix for each element:

$$\mathbf{j}_z^e = \begin{bmatrix} \frac{\partial H_{1u}}{\partial z_u} H_{2u} + H_{1u}\frac{\partial H_{2u}}{\partial z_u} & 0 \\ 0 & \frac{\partial H_{1\phi}}{\partial z_\phi} H_{2\phi} + H_{1\phi}\frac{\partial H_{2\phi}}{\partial z_\phi} \end{bmatrix} \Delta\boldsymbol{\epsilon} \tag{3.14a}$$

$$\mathbf{j}_d^e = \begin{bmatrix} H_{1u}\frac{\partial H_{2u}}{\partial u} & 0 \\ 0 & H_{1\phi}\frac{\partial H_{2\phi}}{\partial \theta} \end{bmatrix} \Delta\boldsymbol{\epsilon}, \tag{3.14b}$$

where as defined previously, $\Delta\boldsymbol{\epsilon} = \boldsymbol{\epsilon}_{i+1}^j - \boldsymbol{\epsilon}_i$. The derivatives in Eq. (3.14), are obtained by differentiation of the H_{1u}, $H_{1\phi}$, H_{2u} and $H_{2\phi}$ functions with respect to displacement and hysteretic DOF, yielding the following expressions:

$$\frac{\partial H_{1u}}{\partial z_u} = n|P_r|^{n-1}\mathrm{sign}(P_r)(1-\alpha_u)Ea/P_c^h \tag{3.15a}$$

$$\frac{\partial H_{1\phi}}{\partial z_\phi} = n|M_r|^{n-1}\mathrm{sign}(M_r)(1-\alpha_\phi)EI/M_c^h \tag{3.15b}$$

$$\frac{\partial H_{2u}}{\partial z_u} = \gamma\zeta(1-\alpha_u)Ea\Delta\epsilon_u \mathrm{sech}(\zeta P^h \Delta\epsilon_u)^2 \tag{3.15c}$$

$$\frac{\partial H_{2\phi}}{\partial z_\phi} = \gamma\zeta(1-\alpha_\phi)EI\Delta\epsilon_\phi \mathrm{sech}(\zeta M^h \Delta\epsilon_\phi)^2 \tag{3.15d}$$

$$\frac{\partial H_{2u}}{\partial u} = \gamma\zeta(P^h\frac{\partial \Delta\epsilon_u}{\partial u})\mathrm{sech}(\zeta P^h \Delta\epsilon_u)^2 \tag{3.15e}$$

$$\frac{\partial H_{2\phi}}{\partial \theta} = \gamma\zeta(M^h\frac{\partial \Delta\epsilon_\phi}{\partial \theta})\mathrm{sech}(\zeta M^h \Delta\epsilon_\phi)^2. \tag{3.15f}$$

Note, assigning an even value to n, removes the absolute value operator from the H_{1u}, $H_{1\phi}$ and their derivatives, resulting in smooth functions without introducing discontinuity in sensitivities. With all associated terms sufficiently defined in Eqs. (3.4) through (3.15), the system of nonlinear equations can be solved for each iteration of the optimization process to determine the DOF of the system, $\mathbf{d}$ and $\mathbf{z}$, for a specified external force, $\mathbf{f}$. Although for quasi-static loading a monotonic analysis is performed for the optimization, the governing equations are the same whether performing a monotonic or cyclic analysis, loading or unloading, and hence, the inelastic deformations, are based on the value of the independent displacements and the hysteretic variables. A pseudo-code for the developed Newton solution algorithm is outlined in Algorithm 1.

3.2.2.2 Plastic moment and signum function approximation

Plastic moment of a section, M_p, is required to evaluate hysteretic bending capacity, M_c^h, that mainly depends on the cross section type and its geometry. For the design examples considered in this study, I-shaped sections are used and M_p is estimated using

Algorithm 1: Pseudo-code for Newton solution algorithm

Initialize: Assemble $\mathbf{R}$, $\mathbf{K}$ and $\mathbf{H}$, set λ (number of force steps), set tol_s (tolerance for convergence of $\mathbf{s}$) and N_j. Start with $\mathbf{d}_0 = [0, ..., 0]^T_{3r\times 1}$ and $\mathbf{z}_0 = [0, ..., 0]^T_{4N\times 1}$ ($\mathbf{x}_0 = [\mathbf{d}_0^T, \mathbf{z}_0^T]^T_{(3r+4N)\times 1}$)

for $i = 1, 2, ..., \lambda$ **do**
  for $j = 1, 2, ..., N_j$ **do**
    for $w = 1, 2, ..., N$ **do**
      Compute and assemble $\mathbf{J}_{vn}$
      Compute and assemble $\mathbf{g}_z$
      Compute and assemble $\mathbf{g}_{zc}$
    end for
    Update the combined system of equations: $\mathbf{g}_v = \mathbf{q}_v + \mathbf{T}_v\mathbf{x}^j_{i+1} - \mathbf{c}_v$
    Update the Jacobian matrix: $\mathbf{J}_v = \mathbf{T}_v + \mathbf{J}_{vn}$
    Solve for: $\mathbf{s} = -\mathbf{J}_v^{-1}\mathbf{g}_v$
    if norm($\mathbf{s}$) $\leq tol_s$
      Convergence met, go to next step, $i + 1$
    else
      Go to next iteration, $j + 1$
    end if
    Update: $\mathbf{x}^{j+1}_{i+1} = \mathbf{x}^j_{i+1} + \mathbf{s}$
  end for
  Update: $\mathbf{x}_i = \mathbf{x}^{j+1}_{i+1}$
end for

the following relations:

$$M_p = M_{pw} + M_{pf}, \quad M_{pw} = \sigma_y(h - 2t_f)^2 t_w/4, \quad M_{pf} = \sigma_y t_f b_f (h - t_f), \tag{3.16}$$

where M_{pw} and M_{pf} are the plastic moments associated with web and flanges of an I-shaped section, respectively. As shown in Eq. (3.16), section properties such as h (section depth), t_w (web thickness), t_f (flange thickness) and b_f (flange width) are required for M_p evaluation, where the relations introduced in Changizi and Jalalpour (2017b) are adopted in this study.

The gradient-based optimization requires sensitivities of the objective function and constraints with respect to the design variables. For computational efficiency, it is preferable to use analytical sensitivities to numerical approximations and this point is one of the motivations for employing the hysteretic beam FE model. However, the exact form of the nonlinear ODEs shown in Eq. (2.13) include the signum function. Hence, a mathematical approximation is introduced in order to obtain analytical sensitivities that

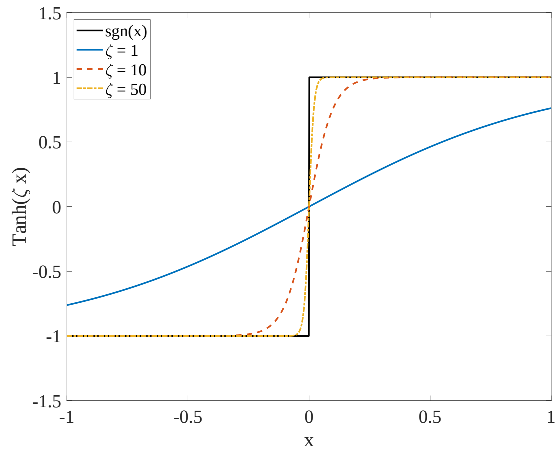

Figure 3.1: Effect of different values of ζ on the shape of hyperbolic tangent comparative to signum function

are continuous and differentiable everywhere. Here, the hyperbolic tangent function is introduced as an approximation for the signum function according to:

$$H_{2u} = \gamma \tanh(\zeta P^h \dot{\epsilon_u}) + \beta \tag{3.17a}$$

$$H_{2\phi} = \gamma \tanh(\zeta M^h \dot{\epsilon_\phi}) + \beta, \tag{3.17b}$$

where ζ is a coefficient that controls the shape of the hyperbolic tangent function in the proximity of zero. Assigning a large numerical value to ζ, closely approximates the signum function shape yet remains differentiable. However, if ζ is very large it can introduce numerical issues during the optimization process because the derivatives in the proximity of 1 and -1 become quite stiff. Hence, we found, through trial and error testing, $\zeta = 50$ to be a sufficient approximation without introducing numerical issues for the optimization process. Effect of setting different ζ values on the shape of hyperbolic tangent is illustrated by the plot in Fig. 3.1.

3.2.2.3 Sensitivities

The use of gradient-based optimization necessitates derivation of sensitivities with respect to the design variable, a. The sensitivity of the objective function is obtained in a straightforward manner and is omitted here for brevity. The main challenge in deriving the sensitivities arises from the nonlinear constraint on the system-level displacement. Sensitivities for the displacement constraint were derived through direct differentiation and begins with the differentiation of the augmented vector, $\mathbf{x}_{i+1}^{j+1}$, with respect to a and continues with the derivation of all subsequent terms to obtain the analytical expressions for the sensitivities. The derivative of system-level displacement constraint is a component of:

$$\frac{\partial \mathbf{x}_{i+1}^{j+1}}{\partial a} = \begin{bmatrix} \frac{\partial \mathbf{d}_{i+1}^{j+1}}{\partial a} \\ \\ \frac{\partial \mathbf{z}_{i+1}^{j+1}}{\partial a} \end{bmatrix}, \tag{3.18}$$

where this derivative is obtained by differentiation of Eq. (3.5) according to:

$$\frac{\partial \mathbf{x}_{i+1}^{j+1}}{\partial a} = \frac{\partial \mathbf{x}_{i+1}^{j}}{\partial a} + \mathbf{J}_v^{-1}\frac{\partial \mathbf{J}_v}{\partial a}\mathbf{J}_v^{-1}\mathbf{g}_v - \mathbf{J}_v^{-1}\frac{\partial \mathbf{g}_v}{\partial a}, \tag{3.19}$$

and the derivative of the Jacobian matrix, $\partial \mathbf{J}_v/\partial a$, is:

$$\frac{\partial \mathbf{J}_v}{\partial a} = \frac{\partial \mathbf{T}_v}{\partial a} + \frac{\partial \mathbf{J}_{vn}}{\partial a}. \tag{3.20}$$

The third term in Eq. (3.19), $\partial \mathbf{g}_v/\partial a$, is obtained by differentiating Eq. (3.9) as follows:

$$\frac{\partial \mathbf{g}_v}{\partial a} = \frac{\partial \mathbf{q}_v}{\partial a} + \frac{\partial \mathbf{T}_v}{\partial a}\mathbf{x}_{i+1}^{j} + \mathbf{T}_v\frac{\partial \mathbf{x}_{i+1}^{j}}{\partial a} - \frac{\partial \mathbf{c}_v}{\partial a}. \tag{3.21}$$

As indicated by Eq. (3.21), the derivatives of the expressions in Eq. (3.10) for $\mathbf{q}_v$, $\mathbf{T}_v$ and $\mathbf{c}_v$ are required and are expressed as:

$$\frac{\partial \mathbf{q}_v}{\partial a} = \begin{bmatrix} \mathbf{0}_{3r\times 1} \\ \frac{\partial \mathbf{g}_z}{\partial a} \end{bmatrix}, \quad \frac{\partial \mathbf{T}_v}{\partial a} = \begin{bmatrix} \frac{\partial \mathbf{K}}{\partial a} & \frac{\partial \mathbf{H}}{\partial a} \\ \mathbf{0}_{4N\times 3r} & \mathbf{0}_{4N\times 4N} \end{bmatrix}, \quad \frac{\partial \mathbf{c}_v}{\partial a} = \begin{bmatrix} \mathbf{0}_{3r\times 1} \\ \frac{\partial \mathbf{g}_{zc}}{\partial a} \end{bmatrix}, \tag{3.22}$$

where $\partial \mathbf{g}_z/\partial a$ is an assembly of the following element level derivatives:

$$\frac{\partial \mathbf{g}_z^e}{\partial a} = \frac{\partial \mathbf{S}}{\partial a}\Delta\boldsymbol{\epsilon} + \mathbf{S}\frac{\partial \Delta\boldsymbol{\epsilon}}{\partial a} \tag{3.23a}$$

$$\frac{\partial \mathbf{S}}{\partial a} = \begin{bmatrix} \frac{\partial H_{1u}}{\partial a}H_{2u} + H_{1u}\frac{\partial H_{2u}}{\partial a} & 0 \\ 0 & \frac{\partial H_{1\phi}}{\partial a}H_{2\phi} + H_{1\phi}\frac{\partial H_{2\phi}}{\partial a} \end{bmatrix}, \tag{3.23b}$$

where the derivatives for functions H_{1u}, $H_{1\phi}$, H_{2u} and $H_{2\phi}$ with respect to design variable, a, are obtained by differentiation of Eqs. (2.7) and (3.17):

$$\frac{\partial H_{1u}}{\partial a} = nP_r^{n-1}\frac{\partial P_r}{\partial a} \tag{3.24a}$$

$$\frac{\partial H_{1\phi}}{\partial a} = nM_r^{n-1}\frac{\partial M_r}{\partial a} \tag{3.24b}$$
$$\frac{\partial H_{2u}}{\partial a} = \gamma\zeta(\frac{\partial P^h}{\partial a}\Delta\epsilon_u + P^h\frac{\partial \Delta\epsilon_u}{\partial a})\text{sech}(\zeta P^h\Delta\epsilon_u)^2 \tag{3.24c}$$
$$\frac{\partial H_{2\phi}}{\partial a} = \gamma\zeta(\frac{\partial M^h}{\partial a}\Delta\epsilon_\phi + M^h\frac{\partial \Delta\epsilon_\phi}{\partial a})\text{sech}(\zeta M^h\Delta\epsilon_\phi)^2. \tag{3.24d}$$

The terms $\partial P_r/\partial a$ and $\partial M_r/\partial a$ in Eq. (3.24) are expressed as:

$$\frac{\partial P_r}{\partial a} = \frac{\frac{\partial P^h}{\partial a}P_c^h - P^h\frac{\partial P_c^h}{\partial a}}{(P_c^h)^2}, \quad \frac{\partial M_r}{\partial a} = \frac{\frac{\partial M^h}{\partial a}M_c^h - M^h\frac{\partial M_c^h}{\partial a}}{(M_c^h)^2}, \tag{3.25}$$

where the derivatives of P^h, P_c^h, M^h and M_c^h with respect to design variables are obtained by differentiation of Eqs. (2.4) and (2.8):

$$\frac{\partial P^h}{\partial a} = (1-\alpha_u)(Ez_u + Ea\frac{\partial z_u}{\partial a}), \quad \frac{\partial P_c^h}{\partial a} = (1-\alpha_u)\sigma_y, \tag{3.26}$$
$$\frac{\partial M^h}{\partial a} = (1-\alpha_\phi)(E\frac{\partial I}{\partial a}z_\phi + EI\frac{\partial z_\phi}{\partial a}), \quad \frac{\partial M_c^h}{\partial a} = (1-\alpha_\phi)\frac{\partial M_p}{\partial a}, \tag{3.27}$$

and the $\partial M_p/\partial a$ term is evaluated by differentiating Eq. (3.16) as follows:

$$\begin{aligned}\frac{\partial M_p}{\partial a} &= \frac{\partial M_{pw}}{\partial a} + \frac{\partial M_{pf}}{\partial a},\\ \frac{\partial M_{pw}}{\partial a} &= \sigma_y\Big(\frac{\partial t_w}{\partial a}(h-2t_f)^2/4 + t_w(h-2t_f)(\frac{\partial h}{\partial a} - 2\frac{\partial t_f}{\partial a})/2\Big)\\ \frac{\partial M_{pf}}{\partial a} &= \sigma_y\Big(\frac{\partial t_f}{\partial a}b_f(h-t_f) + t_f\frac{\partial b_f}{\partial a}(h-t_f) + t_f b_f(\frac{\partial h}{\partial a} - \frac{\partial t_f}{\partial a})\Big).\end{aligned} \tag{3.28}$$

and similarly, $\partial \mathbf{g}_{zc}/\partial a$ is obtained using the element expression given by:

$$\frac{\partial \mathbf{g}_{zc}^e}{\partial a} = \frac{\partial \mathbf{z}_i^{el}}{\partial a} - \frac{\partial \boldsymbol{\epsilon}_i}{\partial a}, \quad \frac{\partial \boldsymbol{\epsilon}_i}{\partial a} = \mathbf{B}\boldsymbol{\Lambda}\frac{\partial \mathbf{d}_i^e}{\partial a}. \tag{3.29}$$

The matrices $\partial \mathbf{K}/\partial a$ and $\partial \mathbf{H}/\partial a$ in Eq. (3.22) are the global assembly of the element derivative matrices according to:

$$\frac{\partial \mathbf{K}^e}{\partial a} = \boldsymbol{\Lambda}^T\frac{\partial \mathbf{K}^{el}}{\partial a}\boldsymbol{\Lambda}, \quad \frac{\partial \mathbf{H}^e}{\partial a} = \boldsymbol{\Lambda}^T\frac{\partial \mathbf{H}^{el}}{\partial a}, \tag{3.30}$$

where the matrices $\partial\mathbf{K}^{el}/\partial a$ and $\partial\mathbf{H}^{el}/\partial a$ are obtained through differentiating Eq. (2.28).

$$\frac{\partial\mathbf{K}^{el}}{\partial a}=E\begin{bmatrix}\frac{\alpha_u}{L} & 0 & 0 & \frac{-\alpha_u}{L} & 0 & 0\\ 0 & \frac{12\frac{\partial I}{\partial a}\alpha_\phi}{L^3} & \frac{6\frac{\partial I}{\partial a}\alpha_\phi}{L^2} & 0 & -\frac{12\frac{\partial I}{\partial a}\alpha_\phi}{L^3} & \frac{6\frac{\partial I}{\partial a}\alpha_\phi}{L^2}\\ 0 & \frac{6\frac{\partial I}{\partial a}\alpha_\phi}{L^2} & \frac{4\frac{\partial I}{\partial a}\alpha_\phi}{L} & 0 & -\frac{6\frac{\partial I}{\partial a}\alpha_\phi}{L^2} & \frac{2EI\alpha_\phi}{L}\\ \frac{-\alpha_u}{L} & 0 & 0 & \frac{\alpha_u}{L} & 0 & 0\\ 0 & -\frac{12\frac{\partial I}{\partial a}\alpha_\phi}{L^3} & -\frac{6\frac{\partial I}{\partial a}\alpha_\phi}{L^2} & 0 & \frac{12\frac{\partial I}{\partial a}\alpha_\phi}{L^3} & -\frac{6\frac{\partial I}{\partial a}\alpha_\phi}{L^2}\\ 0 & \frac{6\frac{\partial I}{\partial a}\alpha_\phi}{L^2} & \frac{2\frac{\partial I}{\partial a}\alpha_\phi}{L} & 0 & -\frac{6\frac{\partial I}{\partial a}\alpha_\phi}{L^2} & \frac{4\frac{\partial I}{\partial a}\alpha_\phi}{L}\end{bmatrix} \tag{3.31}$$

$$\frac{\partial\mathbf{H}^{el}}{\partial a}=E\begin{bmatrix}\frac{(\alpha_u-1)}{2} & 0 & \frac{(\alpha_u-1)}{2} & 0\\ 0 & \frac{\frac{\partial I}{\partial a}(\alpha_\phi-1)}{L} & 0 & -\frac{\frac{\partial I}{\partial a}(\alpha_\phi-1)}{L}\\ 0 & \frac{\partial I}{\partial a}(\alpha_\phi-1) & 0 & 0\\ -\frac{(\alpha_u-1)}{2} & 0 & -\frac{(\alpha_u-1)}{2} & 0\\ 0 & -\frac{\frac{\partial I}{\partial a}(\alpha_\phi-1)}{L} & 0 & \frac{\frac{\partial I}{\partial a}(\alpha_\phi-1)}{L}\\ 0 & 0 & 0 & -\frac{\partial I}{\partial a}(\alpha_\phi-1)\end{bmatrix}, \tag{3.32}$$

where the derivatives of section properties, such as $\partial I/\partial a$, for I-shaped cross-sections are adopted from Changizi and Jalalpour (2017b). The derivative for $\partial\mathbf{J}_{vn}/\partial a$ is expressed using:

$$\frac{\partial\mathbf{J}_{vn}}{\partial a}=\begin{bmatrix}\multicolumn{2}{c}{\mathbf{0}_{(3r)\times(3r+4N)}}\\ \frac{\partial\mathbf{J}_d}{\partial a} & \frac{\partial\mathbf{J}_z}{\partial a}\end{bmatrix}, \tag{3.33}$$

where $\partial\mathbf{J}_z/\partial a$, is the global assembly of the following element level expression obtained by differentiating Eq. (3.14):

$$\begin{aligned}\frac{\partial\mathbf{j}_z^e}{\partial a}=&\begin{bmatrix}\frac{\partial^2 H_{1u}}{\partial a\partial z_u}H_{2u}+\frac{\partial H_{1u}}{\partial z_u}\frac{\partial H_{2u}}{\partial a}+\frac{\partial H_{1u}}{\partial a}\frac{\partial H_{2u}}{\partial z_u}+H_{1u}\frac{\partial^2 H_{2u}}{\partial a\partial z_u} & 0\\ 0 & \frac{\partial^2 H_{1\phi}}{\partial a\partial z_\phi}H_{2\phi}+\frac{\partial H_{1\phi}}{\partial z_\phi}\frac{\partial H_{2\phi}}{\partial a}+\frac{\partial H_{1\phi}}{\partial a}\frac{\partial H_{2\phi}}{\partial z_\phi}+H_{1\phi}\frac{\partial^2 H_{2\phi}}{\partial a\partial z_\phi}\end{bmatrix}\Delta\boldsymbol{\epsilon}\\ &+\begin{bmatrix}\frac{\partial H_{1u}}{\partial z_u}H_{2u}+H_{1u}\frac{\partial H_{2u}}{\partial z_u} & 0\\ 0 & \frac{\partial H_{1\phi}}{\partial z_\phi}H_{2\phi}+H_{1\phi}\frac{\partial H_{1\phi}}{\partial z_\phi}\end{bmatrix}\frac{\partial\Delta\boldsymbol{\epsilon}}{\partial a},\end{aligned} \tag{3.34}$$

and similarly for the $\partial \mathbf{J}_d/\partial a$, the element level expression is obtained by differentiating Eq. (3.14):

$$\frac{\partial \mathbf{j}_d^e}{\partial a} = \begin{bmatrix} \frac{\partial H_{1u}}{\partial a}\frac{\partial H_{2u}}{\partial u} + H_{1u}\frac{\partial^2 H_{2u}}{\partial a \partial u} & 0 \\ 0 & \frac{\partial H_{1\phi}}{\partial a}\frac{\partial H_{2\phi}}{\partial \theta} + H_{1\phi}\frac{\partial^2 H_{2\phi}}{\partial a \partial \theta} \end{bmatrix} \Delta\boldsymbol{\epsilon}$$
$$+ \begin{bmatrix} H_{1u}\frac{\partial H_{2u}}{\partial u} & 0 \\ 0 & H_{1\phi}\frac{\partial H_{2\phi}}{\partial \theta} \end{bmatrix} \frac{\partial \Delta\boldsymbol{\epsilon}}{\partial a}. \tag{3.35}$$

As indicated by Eqs. (3.34) and (3.35), the sensitivities of the functions presented in Eq. (3.15) with respect to design variables are required, where the derivation results in the following expressions:

$$\frac{\partial^2 H_{1u}}{\partial a \partial z_u} = n(1-\alpha_u)E\left((n-1)\frac{\partial P_r}{\partial a}P_r^{n-2}\frac{a}{P_c^h} + \frac{P_r^{n-1}}{P_c^h}\right) \tag{3.36a}$$

$$\frac{\partial^2 H_{1\phi}}{\partial a \partial z_\phi} = n(1-\alpha_\phi)E\left((n-1)\frac{\partial M_r}{\partial a}M_r^{n-2}(M_r)\frac{I}{M_y^h} + M_r^{n-1}\frac{\frac{\partial I}{\partial a}M_y^h - I\frac{\partial M_y^h}{\partial a}}{(M_y^h)^2}\right) \tag{3.36b}$$

$$\frac{\partial^2 H_{2u}}{\partial a \partial z_u} = (1-\alpha_u)E\gamma\zeta\text{sech}(\zeta P^h \Delta{\epsilon_u}^e)^2\left(\Delta\epsilon_u + a\frac{\partial \Delta\epsilon_u}{\partial a}\right.$$
$$\left. -2a\Delta\epsilon_u\tanh(\zeta P^h\Delta{\epsilon_u}^e)(\frac{\partial P^h}{\partial a}\Delta\epsilon_u + P^h\frac{\partial\Delta\epsilon_u}{\partial a})\right) \tag{3.36c}$$

$$\frac{\partial^2 H_{2\phi}}{\partial a \partial z_\phi} = (1-\alpha_\phi)E\gamma\zeta\text{sech}(\zeta M^h \Delta\epsilon_\phi)^2\left(\frac{\partial I}{\partial a}\Delta\epsilon_\phi + I\frac{\partial \Delta\epsilon_\phi}{\partial a}\right.$$
$$\left. -2I\Delta\epsilon_\phi\tanh(\zeta P^h\Delta\epsilon_\phi)(\frac{\partial M^h}{\partial a}\Delta\phi + M^h\frac{\partial\Delta\epsilon_\phi}{\partial a})\right) \tag{3.36d}$$

$$\frac{\partial^2 H_{2u}}{\partial a \partial u} = \gamma\zeta\text{sech}(\zeta P^h \Delta\epsilon_u)^2\left(\frac{\partial P^h}{\partial a}\frac{\partial \epsilon_u}{\partial u} + P^h\frac{\partial^2 \epsilon_u}{\partial a \partial u}\right.$$
$$\left. -2\zeta P^h\frac{\partial\Delta\epsilon_u}{\partial u}\tanh(\zeta P^h\Delta\epsilon_u)(\frac{\partial P^h}{\partial a}\Delta\epsilon_u + P^h\frac{\partial\Delta\epsilon_u}{\partial a})\right) \tag{3.36e}$$

$$\frac{\partial^2 H_{2\phi}}{\partial a \partial \theta} = \gamma\zeta\text{sech}(\zeta M^h \Delta\epsilon_\phi)^2\left(\frac{\partial M^h}{\partial a}\frac{\partial \Delta\epsilon_\phi}{\partial \theta} + M^h\frac{\partial^2 \Delta\epsilon_\phi}{\partial a \partial \theta}\right.$$
$$\left. -2\zeta M^h\frac{\partial\Delta\epsilon_\phi}{\partial \theta}\tanh(\zeta M^h\Delta\epsilon_\phi)(\frac{\partial M^h}{\partial a}\Delta\epsilon_\phi + M^h\frac{\partial\Delta\epsilon_\phi}{\partial a})\right). \tag{3.36f}$$

Eqs. (3.19) - (3.36), and the derivative of the objective omitted, comprise the analytical sensitivities for the volume minimization design formulation.

3.2.3 Solution of the topology optimization process

With the requisite components having been developed in the previous sections, the problem formulation described in Section 3.2 for the topology optimization of frame structures considering material inelasticity is applied following the process depicted by the flow diagram shown in Fig. 3.2. The ground structure approach, widely used for the topology optimization of structures is employed (Dorn, 1964; Bendsoe and Sigmund, 2004). Rather than perform a single phase of optimization and then post-process the results, removing elements with areas less than the minimal constraint value, that could result in a design solution that does not satisfy the constraints, in this study multiple phases of optimization are performed to ensure the final optimized design satisfies the constraints. For each phase of optimization, the gradient-based algorithm employed is the Interior Point algorithm by way of the `fmincon` function in MATLAB (The MathWorks Inc., 2018) with a specified tolerance of 10^{-6} on the objective function and the nonlinear constraint. Following the first phase of optimization, element areas are ranked and those with minimal area are removed from the ground structure, but without exceeding a total elements volume of 5% and an updated FE model is generated accordingly for a subsequent phase of optimization. The limit of 5% of the total volume was found to provide an adequate balance between additional computation and egregious degeneration of the solution. No difference in the final solution was observed when testing lower values for this limit, e.g., 2%. To achieve a converged design solution, subsequent phases of the optimization process (see Fig. 3.2), typically two or three, are performed each starting with the updated design configuration with minimal area elements having been removed. Convergence is achieved when no elements in the optimized design have minimal area, and the design and area proportions remain unchanged from the prior phase of optimization. For each design application, the nonlinear static analysis is carried out using the iterative Newton solution scheme outlined in the previous section. The specified external force is applied in 20 equal force increments.

Due to the non-convex nature of the volume minimization problem, the global optima cannot be guaranteed. However, in an effort to investigate the non-convexity and gain confidence in the optimized solution, a multi-start strategy where initial values of the design variables are randomly assigned (Boese et al., 1994; Martí et al., 2016) is adopted in this study. For each numerical example, an entire optimization process was conducted for five starting cases, that is the set of specified initial cross sectional areas, and the solution from the five optimization processes with the lowest objective function value is considered the best estimate of the global optimal design solution. For each randomized

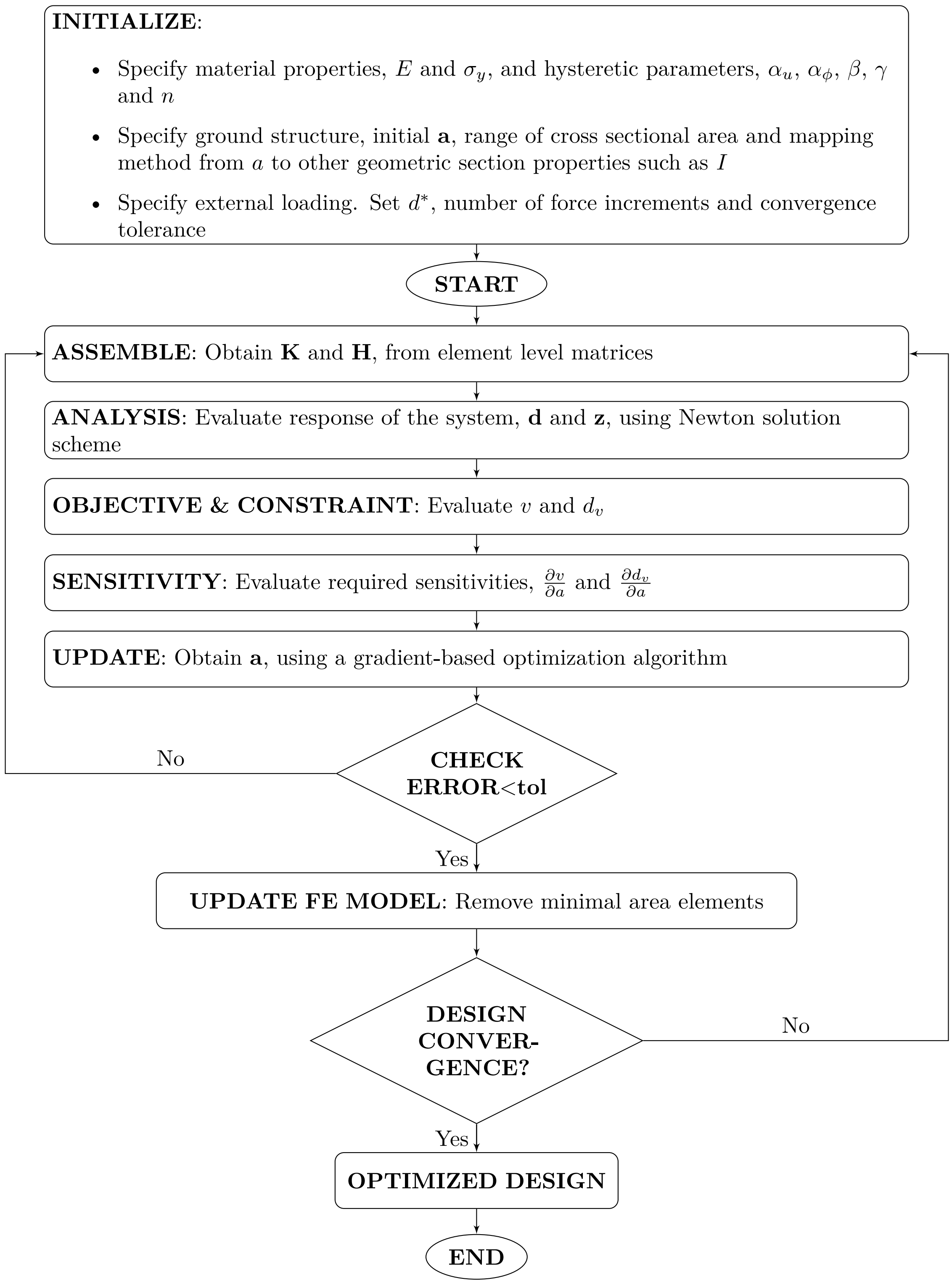

Figure 3.2: Flowchart for topology optimization solution scheme

Axial stress vs axial strain	Normalized moment vs curvature

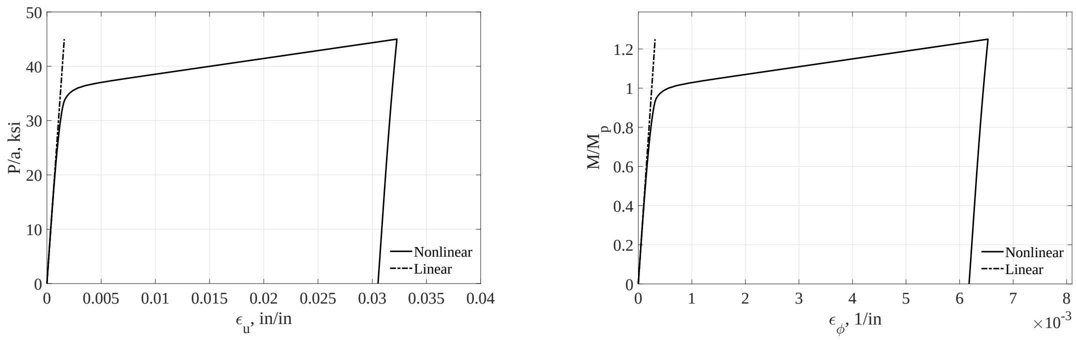

Figure 3.3: Axial stress vs axial strain and normalized moment vs curvature relationships

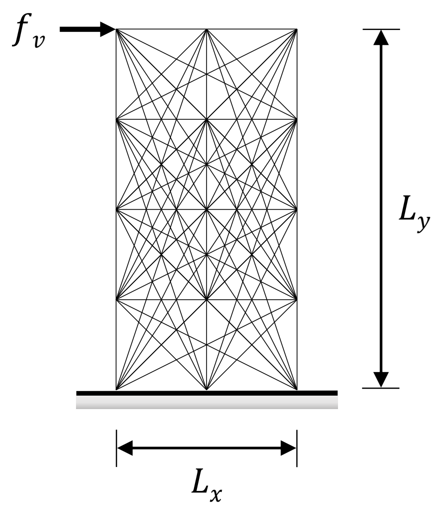

Figure 3.4: Ground structure for the 4×2 frame structure under a lateral external force

start case, the initial cross sectional areas are established by sampling the volume for each element from a uniform distribution, from which the cross sectional area is assigned based upon the elements location in the ground structure. One of the five starting cases assumed the initial cross sectional area of all elements in the ground structure to be equal, referred to as uniform area.

3.3 Numerical examples

The utility of the proposed methodology is demonstrated through two representative numerical examples for the design of structural systems composed of beam elements.

Details pertaining to the two design examples are provided in this section. As previously stated, the ground structure approach is employed in this study, whereby a dense mesh of connected elements is the initial configuration for the considered design examples. The material is assumed to be steel with Young's modulus of $29,000$ ksi and yield stress of 36 ksi. The tolerance for the norm of residual vector, tol_s, in the Newton solution algorithm is set equal to 10^{-6}. The inelastic to elastic ratios, α_u and α_ϕ, are each set equal to 0.01, and exponent, n, for the hysteretic functions is set equal to 2. The constitutive relationship considered is illustrated by the axial stress versus axial strain, and normalized moment versus curvature relationships shown in Fig. 3.3. These relationships are obtained using the hysteretic laws introduced in Chapter 2, and the entire response, that is the loading branch, unloading branch and inelastic deformations, are determined by the hysteretic variables that are governed by the hysteretic evolution equations. Also shown in Fig. 3.3, for reference, is a linear-elastic response.

3.3.1 Example 1: A 4×2 frame structure

The first example is the design of a 4×2 frame structure with a lateral force applied at the top left node of the domain. The ground structure, boundary conditions and direction of applied force are shown in Fig. 3.4. The dimensions of the domain are $L_x = 19.68$ ft (6 m) and $L_y = 39.4$ ft (12 m). This cantilever-type structure with the applied external force at the tip point, has been extensively used for a wide variety of design problems in topology optimization (Sigmund, 2001; Andreassen et al., 2011; Changizi et al., 2017).

Prior to each example, the accuracy of the analytical sensitivities developed in Section 3.2.2.3 were evaluated by comparison, to those obtained from a finite difference approximation. The sensitivity values of the displacement constraint for the 4×2 frame ground structure are shown in Fig. 3.5. As is seen form Fig. 3.5 the derived sensitivities from the two methods agree well with negligible error (less than 0.05%), verifying the accuracy of the analytical sensitivities obtained through the direct differentiation approach. Furthermore, comparisons of the analytical and numerical sensitivities for the 4×2 frame structure for two iterations in the first phase of optimization, at approximately iterations 10 and 20, are shown in Fig. 3.6, and again, the maximum relative error for each sample is less than 0.5%.

The minimum volume design problem subject to displacement constraint is solved for the frame structure shown in Fig. 3.4 for a specified displacement constraint d^* of 11.8 in, equivalent to a drift ratio of 2.5% (i.e., $d^*/L_y = 0.025$) and the specified external force of 500 kips. The optimized design for the $d^* = 0.025L_y$ by starting optimization

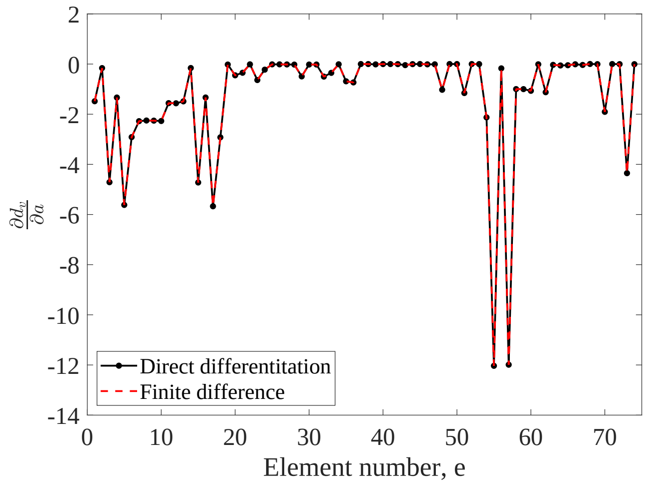

Figure 3.5: Comparison of the results of sensitivity analysis derived with the analytical direct differentiation method and finite difference approximation for the 4×2 frame ground structure

Sample 1	Sample 2
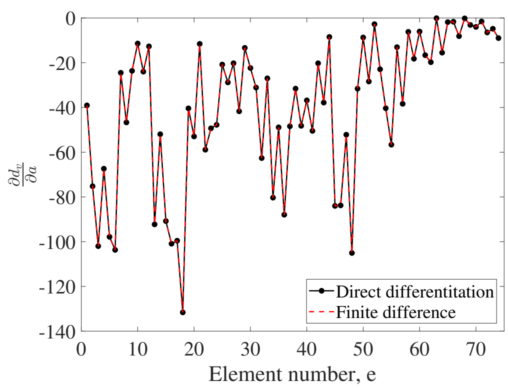	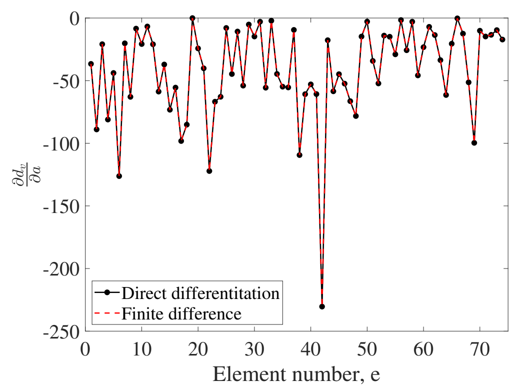

Figure 3.6: Comparison of the results of sensitivity analysis with analytical method and finite difference approximation for two sample iterations in optimization

from the uniform area distribution is shown in Fig. 3.7, where the thickness of the lines comprising the topologies indicates the relative size of the element area and the area values are normalized with respect to the their maximum among the designs. Numerical value adjacent to each element denotes corresponding element number. A volume of $2.3995{\times}10^4$ in^3 was required for the nonlinear optimization / design to satisfy the drift constraint.

In addition to the uniform area starting case, as described in Section 3.2.3, four randomized area starting cases were performed for each numerical example in an attempt to

Nonlinear design, $d^* = 0.025L_y$	Linear design	Force-displacement response
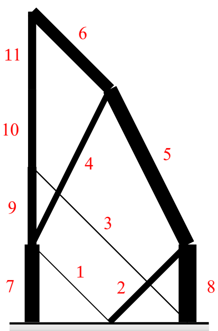	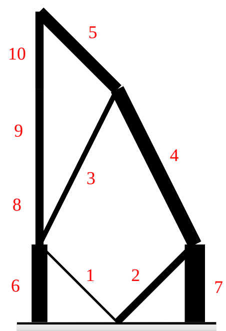	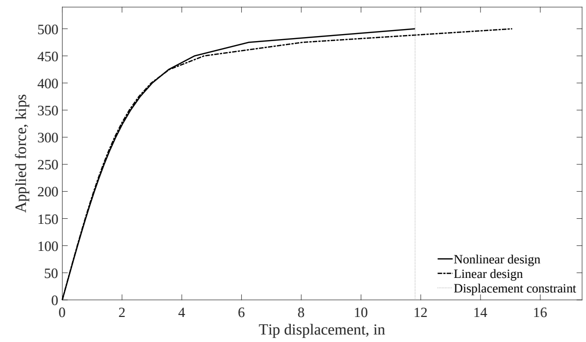

Figure 3.7: Nonlinear minimum volume design for 2.5% system drift ratio and comparative Linear design with the equivalent volume for the 4×2 frame structure along with the force-displacement responses for each optimized design. Numerical values adjacent to structural elements denote the element number

	Case 1	Case 2	Case 3	Case 4
Initial areas	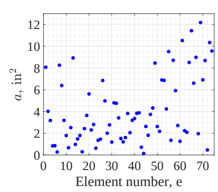	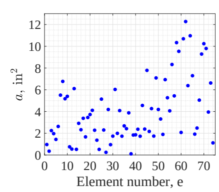	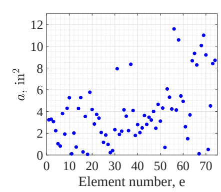	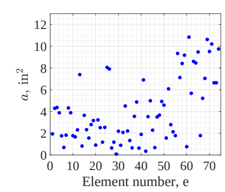
Optimized design	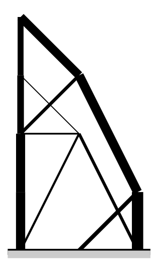	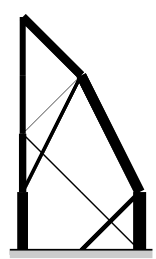	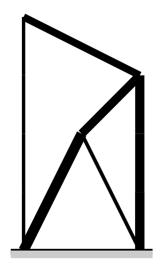	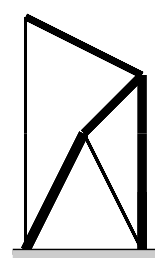
v, in^3	2.4241×10^4	2.4024×10^4	2.4674×10^4	2.4702×10^4
N	13	12	11	11
min(a), in^2	1.98	0.93	6.89	6.92
max(a), in^2	23.31	26.86	21.31	21.33

Figure 3.8: Resulting nonlinear optimized designs for randomized starting cases for the 4×2 frame structure

identify the global optima. The optimized topologies obtained for each of the randomized starting cases, including attributes of the optimized designs, and a plot of the initial randomized areas for the 4×2 frame structure are presented in Fig. 3.8. Numerical values of the initial cross sectional areas for each starting case are tabulated and reported in Appendix A. It can be seen from a comparison of the results shown in Fig. 3.7 with those shown in Fig. 3.8, that since all designs satisfy the displacement constraint, $d^* = 11.81$ in, the nonlinear design shown in Fig. 3.7 is comprised of the lowest volume among the five designs, and hence is considered the best solution.

To investigate the effect of considering material nonlinearity directly in the optimization problem, the best nonlinear design shown in Fig. 3.7, is compared to the best design solutions from two additional optimization problems considering the same domain and external force but assuming the material to be linear-elastic. Specifically, the first linear optimization problem seeks to minimize the compliance for a given volume constraint and the second linear optimization problem seeks to minimize the volume subjected to a drift displacement constraint. These linear design solutions where then evaluated using nonlinear FE analysis described in Section 3.2.2.1 to assess their respective performance and compare this performance to that of the best nonlinear design. Details pertaining to the two linear optimization formulations can be found in Appendix B. For the linear optimization problems, the same multi-start strategy performed for the nonlinear design problem was employed, and the solution with the lowest objective function value was considered the best linear design. Fig. 3.7 shows a comparison of the solution from nonlinear volume minimization problem, denoted Nonlinear design, with the solution of the linear compliance minimization problem, denoted Linear design, and their performance in terms of system force-displacement response when evaluated using nonlinear FE analysis. The Linear design is obtained by setting the optimal volume of the nonlinear design as the volume constraint for the linear compliance problem. From Fig. 3.7 it can be seen, that both designs share a common primary load path, however, the Nonlinear design includes an additional diagonal element in comparison to the Linear design and the proportioning of the individual areas differs between the two designs. For reference, the element with maximum area is from the Linear compliance design solution located at element 7 with an area of 31.18 in^2. Importantly, from the system force-displacement responses shown in Fig. 3.7, the Nonlinear design satisfies the specified constraint (11.8 in), whereas the Linear design with the same volume of material as the Nonlinear design, exceeds the specified constraint, with a displacement of 15.06, equivalent to a drift ratio of 3.2%, or 27.5% larger than the response of the Nonlinear optimized design.

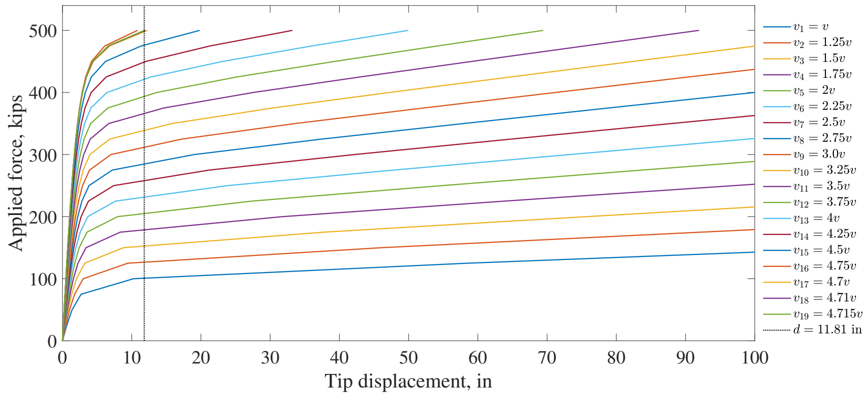

Figure 3.9: Force-displacement responses of the linear volume minimization design by factoring the areas

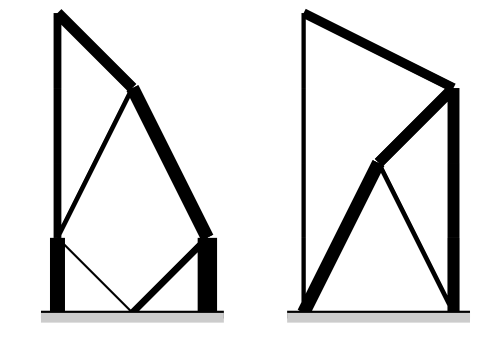

Figure 3.10: Linear optimized topologies obtained from uniform and random starting cases for the 4×2 frame structure

The solution of the second linear optimization problem, that is volume minimization subject to the same displacement constraint (2.5% drift) resulted, in linear design solution with the same general topology as the Linear design shown in Fig. 3.7 but with a volume of $5.1767{\times}10^3$ in^3. As anticipated, this volume is considerably smaller than the optimal volume of the Nonlinear design. Scaling the linear volume of $5.1767{\times}10^3$ in^3 by a factor of 4.715, without changing the proportioning of the element cross sectional areas, results in a design based on the linear optimized topology that satisfies the drift constraint when evaluated by nonlinear quasi-static analysis, illustrated in a step by step analysis shown in Fig. 3.9. Interestingly, $4.715 \times 5.1767 \times 10^3 = 2.4408 \times 10^4$ in^3, exceeds the volume of the nonlinear design of $2.3995{\times}10^4$ in^3. These comparisons illustrate the Nonlinear design either offers better performance for the same volume or lower volume for a given level of performance, by comparison to the two optimized linear designs.

As mentioned above, the same multi-start strategy is employed for the linear design

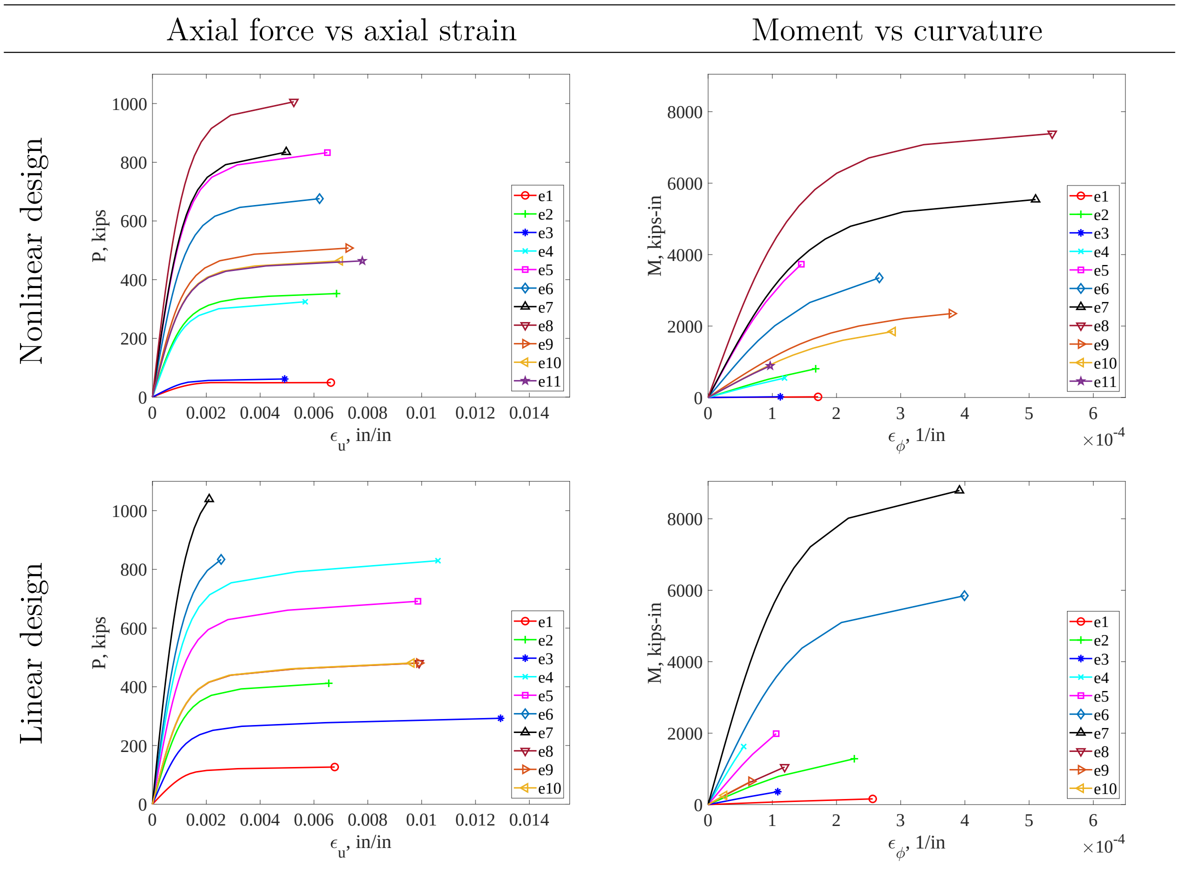

Figure 3.11: Element axial force vs axial strain and moment vs curvature for the nonlinear and linear designs of 4×2 cantilever

problem, where each of the randomized starting cases resulted in two observed design solutions that are shown in Fig. 3.10. With the linear design on the left, that is the best linear solution, the diagonal element in the Nonlinear design (element 3 in Fig. 3.7) did not appear, regardless of the initial guess/randomized starting case. The linear design on the right of Fig. 3.10, however, has a distinctly different topology from the best Nonlinear design.

In addition to system level responses, element level axial force vs axial strain, and bending moment vs curvature, for all the elements present in the Nonlinear and Linear designs are shown in Fig. 3.11. As can be seen through these graphs, element nonlinearity is more evenly distributed in the Nonlinear design, however, in the Linear design, couple of elements remained mostly in the elastic region. These graphs show that the Nonlinear design distributes inealsticity among more number of elements to limit the displacement at the tip point.

Table 3.1: Summary of the performance metrics and design attributes of the Nonlinear volume minimization optimized design and corresponding Linear design for the 4×2 frame structure

	Nonlinear	Linear
	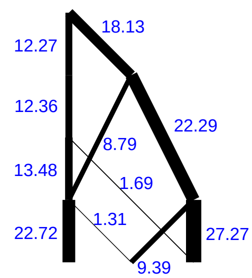	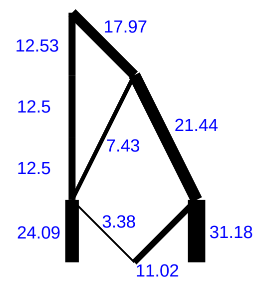
v, in^3	2.3995×10^4	2.3995×10^4
d_v, in	11.81	15.06
E_T, kips-in	4.8863×10^3	4.8198×10^3
N	11	10
min(a), in^2	1.31	3.38
max(a), in^2	27.27	31.18

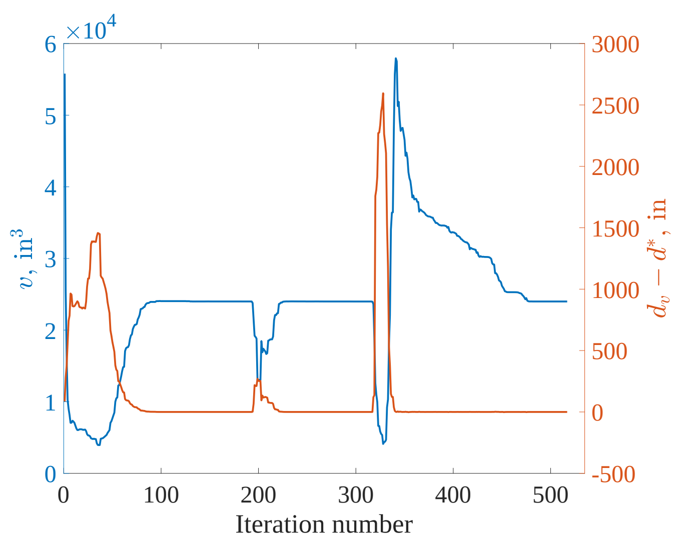

Figure 3.12: Iteration histories of the objective and constraint for the Nonlinear design of 4 × 2 frame structure

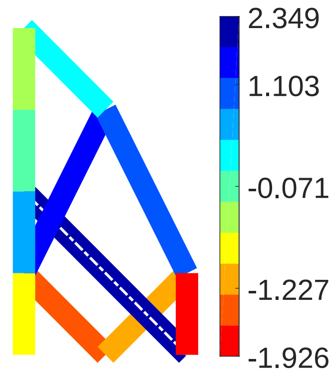

Figure 3.13: Element volume difference plot for the 4×2 frame optimized Nonlinear and Linear designs

A summary of the performance metrics and design attributes, for the Nonlinear and Linear designs is provided in Table 3.1. The cross sectional areas (in^2) for the optimized designs are reported next to each element, from which the different allocation of volume to the common load path between the Nonlinear and Linear designs is apparent. The lateral force resistance of the Nonlinear design, at a given displacement is marginally larger than that of the Linear design and hence the total energy (E_T) absorbed up to the displacement constraint is larger for the Nonlinear design by 1.4%. Moreover, the minimum and maximum cross sectional areas of the Nonlinear design, in comparison to the Linear design, have been reduced.

The objective function and displacement constraint values for each iteration throughout the entire optimization process, following the procedure shown in Fig. 3.2, for the best nonlinear design of the 4×2 frame are shown in Fig. 3.12. The periodic drop and rise of the objective and constraint values correspond to the beginning of each phase of optimization. As can be seen from Fig. 3.12, the value of $d_v - d^*$ is approximately zero at the final phase, illustrating that the optimized Nonlinear design satisfies the specified displacement constraint d^*.

When considering material inelasticity, the distribution of volume differs from the Linear design. To illustrate the difference of volume allocation between the Nonlinear and Linear designs, the element volume difference in terms of percent of total volume is shown using a range of colors in Fig. 3.13. These colors are superimposed on the union of the optimized designs connectivities, and the percent values are reported next to a colorbar. The white dotted line distinguishes the elements that only are present in the Nonlinear design. The difference plot in Fig. 3.13 shows that relative to Linear design, a portion of

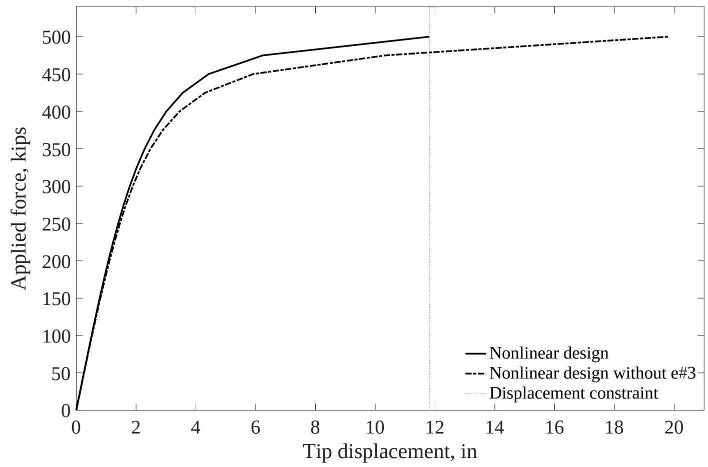

Figure 3.14: Force-displacement responses of the optimized Nonlinear design for 4×2 frame structure with and without element 3

volume from the main load path in the base elements (i.e., 7 and 8) for the Nonlinear design has been reallocated to other elements in the primary load path (i.e., 5 and 6) and to add diagonal elements, or increase the volume of the common diagonal elements (i.e., 3 and 4). The redistribution is, in part, because in the Nonlinear design the moment capacity of the elements is explicitly considered and if reached, supporting diagonal elements are required to limit deformations and hence additional elements appear where unbraced elements form plastic hinges, in particular at the connecting node of elements 9 and 10. These differences in topology and volume allocation enables Nonlinear design to outperform the Linear design.

To illustrate the importance of the diagonal elements, element 3 is removed from the Nonlinear design and an additional nonlinear analysis is performed for the same specified external force. The corresponding force-displacement response for the Nonlinear design with and without element 3 is shown in Fig. 3.14. Although element 3 constitutes only 2.35% of the total volume of the optimized structure, its importance in attaining the specified displacement constraint is significant, as its removal results in a substantial increase (68.6%) in tip displacement relative to the Nonlinear design with element 3 intact and hence is not able to satisfy the displacement constraint.

Additionally, the hysteretic FE model permits assessing the cyclic response of the design and evaluating the inelastic displacements. The optimized Nonlinear design was analyzed for the cyclic force history shown in Fig. 3.15 to obtain the system overall cyclic response also shown in Fig. 3.15 and accordingly, the inelastic deformations can be evaluated.

Cyclic applied loading vs pseudo time	Nonlinear design response

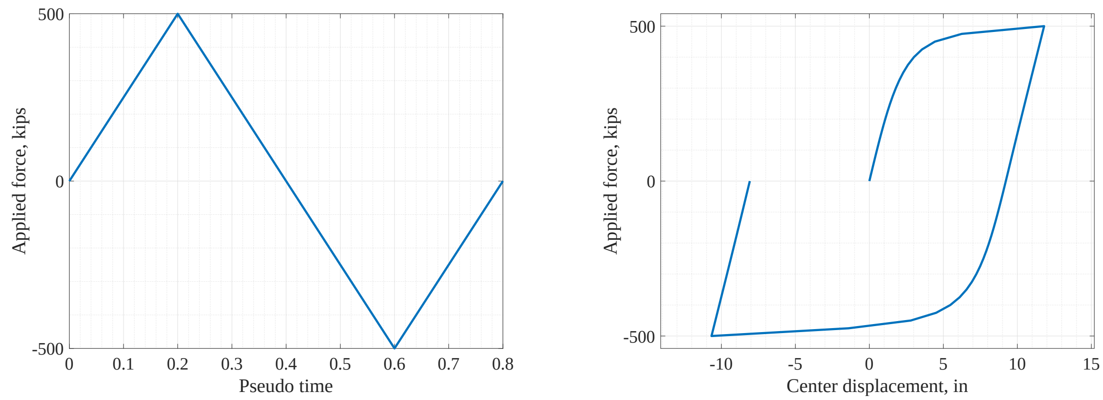

Figure 3.15: Cyclic force history and cyclic response for the Nonlinear design of 4×2 frame

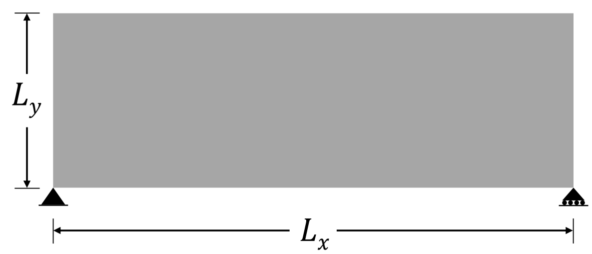

Figure 3.16: Full domain of the beam structure with boundary conditions

3.3.2 Example 2: A 3×2 half beam

The second design example is a 3×2 half beam structure under a vertical external force at the center of the full domain. The beam domain and boundary conditions are shown in Fig. 3.16. Due to the symmetry of the boundary conditions and loading for the full domain, a symmetric design is expected, therefore half of the domain is modelled and used in the optimization process for computational efficiency, where the ground structure and location of the applied force are shown in Fig. 3.17. The dimensions of the half domain are $L_x = 59.05$ ft (18 m) and $L_y = 19.68$ ft (6 m). Similar to Example 1, the minimum volume design problem subject to displacement constraint is solved for a center displacement constraint as $d^* = L_x/200$ and applied external force of 250 kips. This bridge-like structure has been employed in topology optimization for different applications (Sigmund, 2001; Jalalpour et al., 2013; Changizi and Jalalpour, 2018).

As in Example 1, the values of the sensitivities for the displacement constraint

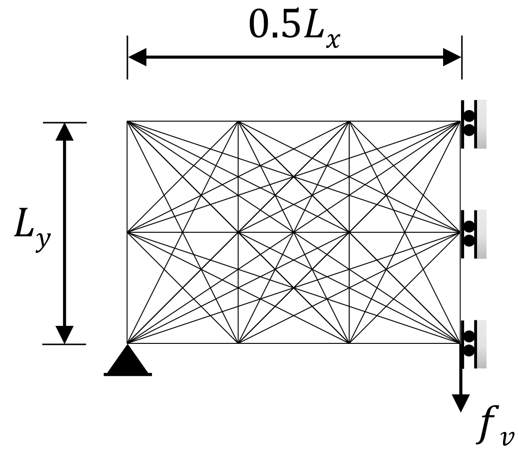

Figure 3.17: Ground structure for the 3×2 half beam structure under a vertical force

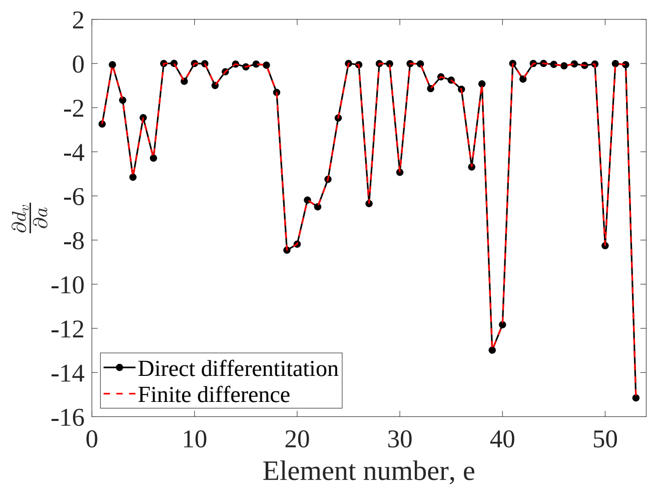

Figure 3.18: Comparison of the results of sensitivity analysis derived with the analytical direct differentiation method and finite difference approximation for the 3×2 half beam ground structure

evaluated using the analytical gradients developed for the hysteretic beam FE modeling approach via the direct differentiation method are compared with numerical sensitivities obtained by finite difference approximation for the 3×2 half beam ground structure. For comparison, these sensitivities are plotted in Fig. 3.18. As with Example 1, the sensitivities agree well with negligible relative error thus providing a verification of the accuracy of the analytical sensitivities obtained through the direct differentiation approach described in Section 3.2.2.3.

Similar to Example 1, the nonlinear design problem is solved for multiple starting cases, including uniform and randomized starting areas. The resulting optimized topologies

Nonlinear design, $d^* = L_x/200$	Linear design	Force-displacement response
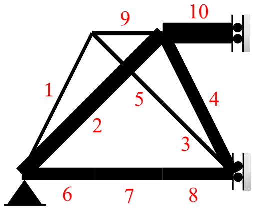	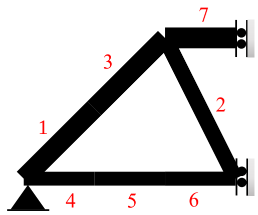	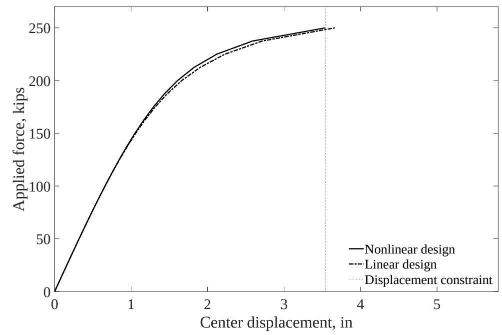

Figure 3.19: Nonlinear minimum volume design for $L_x/200$ center displacement and the comparative Linear design with the equivalent volume for the 3×2 half beam structure along with the force-displacement responses for each optimized design. Numerical values adjacent to the elements indicate the element number.

for uniform and randomized areas are shown in Fig. 3.19 and Fig. 3.20, respectively. Plot of the randomized initial area values for each randomized starting case and design attributes are also presented in Fig. 3.20. Numerical values for the randomized areas for each starting case are tabulated and reported in Appendix A. Again all designs satisfy the displacement constraint of $d^* = L_x/200 = 3.54$ in, so that by comparing the results shown in Fig. 3.19 with those shown in Fig. 3.20, the nonlinear design shown in Fig. 3.19 is comprised of the lowest volume and hence is considered the best nonlinear design solution.

As with Example 1, the best nonlinear topology is compared with the optimized solutions from two linear topology optimization problems. Again a multi-start strategy is employed for both linear topology optimization problems and the linear design reported for each optimization problem is the one with the lowest objective function value that satisfied the constraints from among all the starting cases. These linear design solutions where then evaluated using nonlinear FE analysis described in Section 3.2.2.1 to assess their respective performance and compare this performance to that of the best nonlinear design. The first linear optimization problem seeks to minimize the compliance for a given volume constraint. More specifically, the Linear design is obtained by setting the optimal volume of the nonlinear design as the volume constraint for the linear compliance problem for the purpose of comparison. The Linear design and the associated force-displacement responses obtained from nonlinear quasi-static analysis of the Nonlinear and Linear

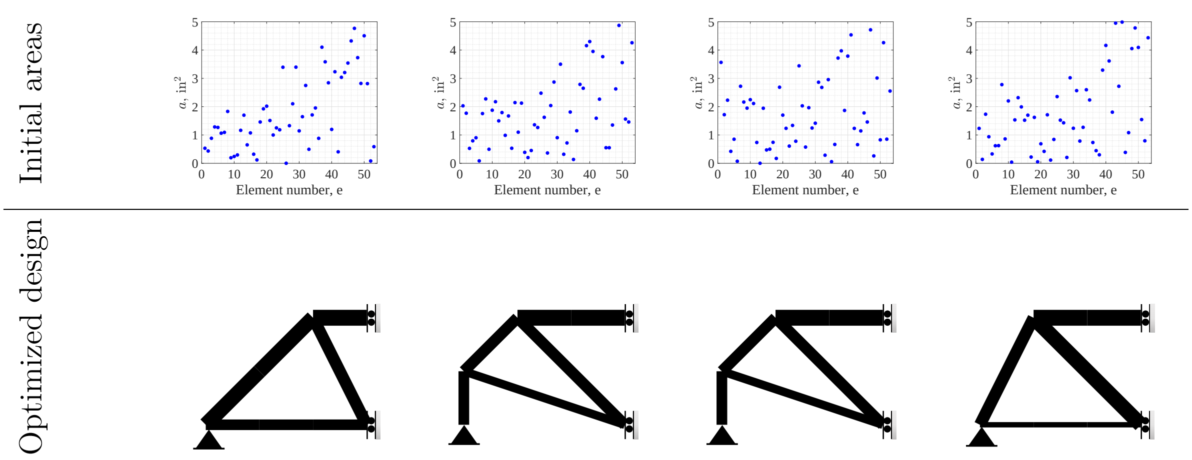

	Case 1	Case 2	Case 3	Case 4
v, in^3	9.2178×10^3	9.2287×10^3	9.2287×10^3	9.2229×10^3
N	7	6	6	7
min(a), in^2	7.09	5.63	5.63	3.57
max(a), in^2	10.62	10.62	10.62	10.60

Figure 3.20: Resulting nonlinear optimized designs for randomized starting cases for the 3×2 half beam structure

designs are shown in Fig. 3.19. For reference the element with maximum area is located in the Linear design solution (element 7). As seen from Fig. 3.19, the Nonlinear topology obtained from the proposed methodology, shows a common primary load path with the Linear design, but includes additional diagonal elements outside of this primary load path. Albeit by less of a margin than with Example 1, as expected, the Nonlinear design satisfies the specified center displacement constraint, whereas the Linear design slightly exceeds the constraint for this example.

The second linear optimization problem seeks to minimize the volume subjected to a drift displacement constraint. Solving the linear volume minimization design problem subject to the displacement constraint d^* of $L_x/200$ resulted in a volume of 4.1016×10^3 in^3 (for details of the linear design problems see Appendix B). The topology for the linear volume minimization problem is similar to that shown in Fig. 3.19 and has been omitted to avoid unnecessary repetition. As expected, this volume is considerably smaller than the optimal volume of the Nonlinear design. Scaling the linear volume by a factor of 2.25 results in a design, based on the linear volume minimization design, that satisfies the displacement constraint when evaluated by nonlinear quasi-static analysis, illustrated in a step by step analysis shown in Fig. 3.21. However, 2.25 times 4.1016×10^3 in^3, or

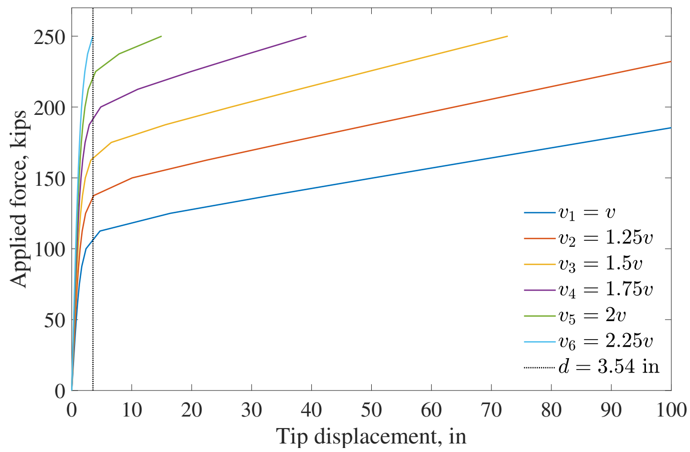

Figure 3.21: Force-displacement responses of the linear volume minimization design by factoring the areas

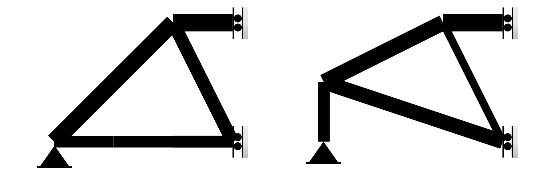

Figure 3.22: Linear optimized topologies obtained from uniform and random starting cases for the 3×2 half beam structure

$9.2286{\times}10^3$ in^3, exceeds the volume of the Nonlinear design of $9.1790{\times}10^3$ in^3. These results are consistent with those observed for the Nonlinear design of the $4{\times}2$ frame structure in Example 1, and again illustrate that the Nonlinear design either offers better performance for the same volume or lower volume for a given level of performance, by comparison to the two linear designs.

Similar to Example 1, results of multi-start strategy for the linear design problem, for the 3×2 half beam structure are shown in Fig. 3.22. The best linear design shown in the right, is distinctively different in a comparison to the sub-optimal design shown on the left side of Fig. 3.22.

Table 3.2 summarizes the results and attributes for the Nonlinear and comparative Linear design solutions for the 3×2 half beam. Again the cross sectional areas (in^2) for the optimized designs are reported next to each element, and the difference in the values of areas are shown. In the Nonlinear design, the volume allocated to the primary load path (i.e., elements 2, 4, 6, 7, 8 and 10) is less than for the Linear design, and a portion of volume is allocated to the supplementary supporting elements (i.e., elements 1, 3, 5

Table 3.2: Summary of the performance metrics and design attributes of the Nonlinear volume minimization optimized design and corresponding Linear design for the 3×2 half beam structure

	Nonlinear	Linear
	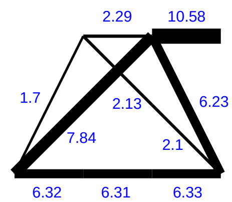	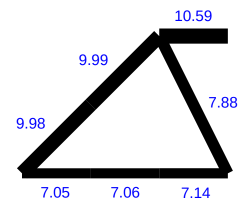
v, in^3	$9.1790{\times}10^3$	$9.1790{\times}10^3$
d_v, in	3.54	3.66
E_T, kips-in	$6.3150{\times}10^2$	$6.2656{\times}10^2$
N	10	7
min(a), in^2	1.70	7.05
max(a), in^2	10.58	10.59

and 9), that is necessary to satisfy the specified design constraint. Again, the Nonlinear design has a marginally higher force resistance for a given displacement and as such results in a larger amount of absorbed energy (E_T) up to the displacement constraint, by comparison to the Linear design, by 0.8%. In the Nonlinear design, the minimum and maximum cross sectional areas have been reduced relative to the Linear design. Similar to Example 1 design, the optimal volume redistribution and increase in the number of elements relative to the Linear design, are the main differentiating features.

The volume difference plot for the half beam optimized Nonlinear and Linear designs is shown in Fig. 3.23. The same range of colors similar to the first example is employed, and white dotted line distinguishes the elements present only in the Nonlinear design. A considerable share of total volume in the common elements, has been allocated to the outer bracing system in the Nonlinear topology, that resulted in lower center displacement given the same amount of volume.

The histories of the objective and displacement constraint for each iteration throughout the optimization process for the Nonlinear design of the 3×2 half beam frame are shown in Fig. 3.24 following the process shown in Fig. 3.2. Again, in the final phase, that is

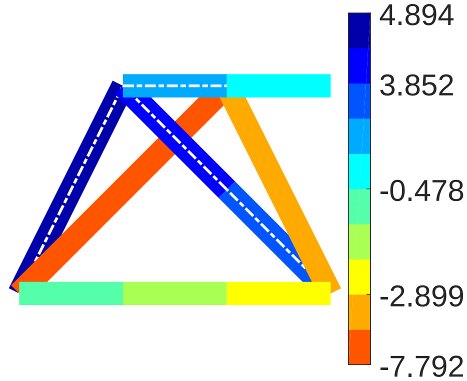

Figure 3.23: Element volume difference plot for the 3×2 half beam optimized Nonlinear and Linear designs

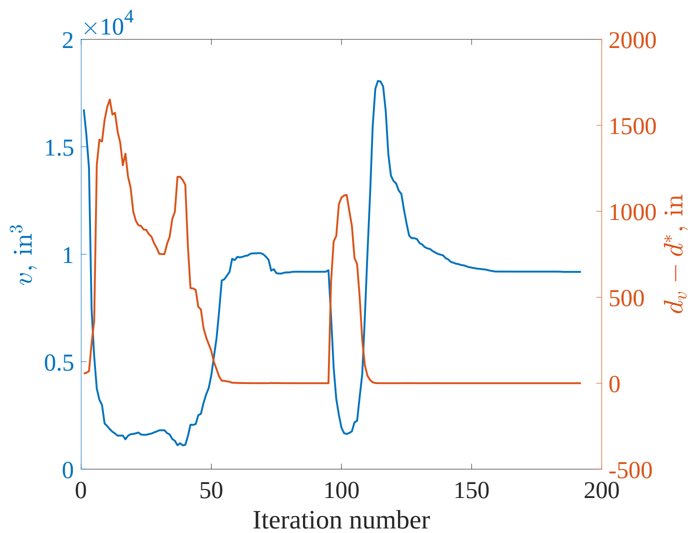

Figure 3.24: Iteration histories of the objective and constraint for the Nonlinear design of 3×2 half beam structure

last iteration, the value of $d_v - d^*$ is approximately zero indicating that the displacement constraint is satisfied at the final stage of optimization. As with Example 1, the periodic drop and rise of the objective and constraint values correspond to the beginning of each phase of optimization.

As previously mentioned, the hysteretic FE modeling permits analysis of the cyclic response and evaluating the inelastic deformations of the system without any change in the formulation. For this example, the cyclic loading shown in Fig. 3.25 is applied to the optimized Nonlinear beam design presented in Fig. 3.19 to obtain the cyclic response of the design and inelastic deformations.

Cyclic applied loading vs pseudo time	Nonlinear design response

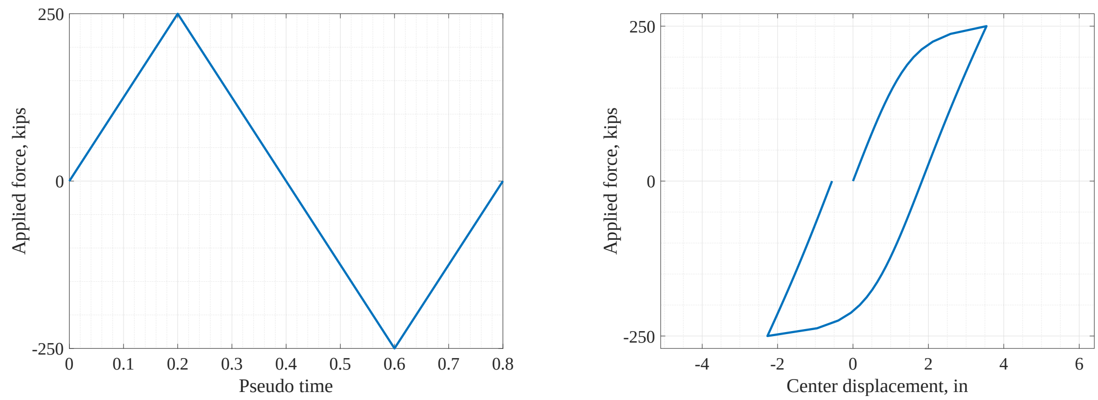

Figure 3.25: Cyclic force history and cyclic response for the Nonlinear design of 3×2 half beam

3.4 Summary and concluding remarks

This Chapter contributes a method for the topology optimization of nonlinear structures based on a hysteretic beam FE model. Two beneficial features of the hysteretic FE modeling approach in the context of topology optimization are that analytical sensitivities could be derived by invoking a mathematical approximation for the signum function and the stiffness and hysteretic matrices need only to be evaluated once for each nonlinear structural analysis. As such, original analytical sensitivities and solution algorithms were presented to combine the hysteretic FE modeling approach and topology optimization. The beam element nonlinearity was modeled using the multiaxial hysteretic laws for the axial and bending moment.

The utility of the method was demonstrated through two numerical design examples. The optimized designs are sought while permitting material inelasticity by way of inelastic deformations in individual elements. Due to the non-convexity of the optimization problem considered in this Chapter, multiple starting cases with randomized initial cross sectional areas were performed and used to initiate the optimization process. For each design example presented, the uniform area starting cases resulted in the best nonlinear design solution. However, it is worth noting, that sampling from a high-dimensional design space subjected to nonlinear constraints in the context of topology optimization is an ongoing research topic. The resulting nonlinear design comprised of elements along a common load path with the comparative linear design. However, the distribution of volume to elements in the common load path varies and additional elements are included in the nonlinear design. These elements are necessary for the design to achieve the specified displacement constraint. While, the primary structural system designs are similar, there are differences between the nonlinear and linear designs that serve important purposes in attaining the overall design objectives, and as has been shown, removing only one element with a small cross sectional area, results in significant displacement increment. Although the optimized topologies from the nonlinear and linear designs share some similar features, in the context of frame structures and beam elements, the findings from this Chapter suggest that the solution obtained from linear-elastic problem formulation is not suitable if inelastic deformations are expected and that the inelastic deformations should be explicitly considered to ensure the designs compliance with the specified requirements.

Chapter 4
Design Method for Dynamic Excitation

4.1 Overview

This Chapter presents a design method for the topology optimization of frame structures composed of nonlinear hysteretic beam elements with multiaxial axial-moment interaction and distributed plasticity subject to time-varying base excitation. The methodology is applied for the design of frame structures where the objective is to minimize the total volume in the domain, such that the maximum of the displacement response, at specified nodes in the domain, satisfy a specified constraint (i.e., drift limit). The maximum of the displacement response at specified nodes throughout the time-varying analysis is estimated using the p-norm. Generally, for the optimization of dynamic problems with time-varying excitation, especially when considering nonlinearity, a computationally efficient time integration solution scheme and gradient-based optimization are considered desirable (Sigmund, 2011). As is common with nonlinear FE analysis, a Newton solution scheme iteratively solves for the unknown DOF for each increment of external force. Since with quasi-static analysis, the number of force steps is typically modest, the computational demands of the Newton method embedded in an optimization scheme is manageable. However, considering time-varying excitation, the computational demands of employing an iterative Newton solution scheme increase significantly, owing to the need to perform iteration at each time step in the dynamic analysis in conjunction with the typically small time steps and duration of the excitation. As such, in this Chapter the concept of topology optimization employing the hysteretic FE modeling approach is considerably extended to the dynamic problem whereby the governing equations are formulated as a system of first order ODEs. Multiaxial interactions are considered through an appropriate yield/capacity function and distributed plasticity is accounted for through hysteretic interpolation functions (Triantafyllou and Koumousis, 2011, 2012b). Constant element matrices, specifically the elastic stiffness and hysteretic matrices, do not require updating throughout the time-varying analysis as the nonlinearities are represented through the hysteretic variables, specifically curvature and axial deformations. The hysteretic variables, evolve according to nonlinear ODEs and, for the case of multiaxial interaction, the specified yield function. Hence, the system level governing dynamic equilibrium equations and hysteretic beam FE formulation can thus be concisely presented together as a system of nonlinear first order ODEs that is solved using the 4th order Runge-Kutta method, without the need of linearization. Analytical sensitivities are derived by direct differentiation and the accuracy is confirmed by comparison to gradients obtained from the finite difference method. The utility of the suggested method is demonstrated through several numerical examples for the design of structural frames subjected to pulse, harmonic and seismic base excitation. As a point of comparison, comparable topology optimization problem(s) assuming linear-elastic material behavior, are solved to obtain optimal linear design solutions. The linear designs are then evaluated using nonlinear dynamic analysis to obtain their response(s) that are then compared to the response/performance of the nonlinear designs. In general, these comparisons show that the nonlinear designs differ in composition and outperform the linear designs, when assessed by nonlinear dynamic analysis.

The remainder of the Chapter is organized as follows. Section 4.2 develops the overall methodology, beginning with the governing nonlinear dynamic equilibrium equations and state-space solution scheme. Following this discussion, the design problem for topology optimization of structural systems considering time-varying excitation and material nonlinearity is introduced and the sensitivities with respect to the design variables are developed. Section 4.3 presents the numerical examples along with a discussion of the results and observations. Lastly, in Section 4.4, a summary and description of the main contributions and findings are provided.

4.2 Methodology

The topology optimization problem formulation and its essential components are described in this section. These include the governing system-level nonlinear dynamic equilibrium equations and their representation in the state-space, the optimization problem formulation and the corresponding sensitivities to facilitate gradient-based optimization.

4.2.1 Nonlinear dynamic equilibrium equations

The governing dynamic equilibrium equations for a multi DOF, nonlinear, system is a set of second order, nonlinear, non-homogeneous ODEs expressed as follows:

$$\mathbf{M}\ddot{\mathbf{d}}_i + \mathbf{C}\dot{\mathbf{d}}_i + \mathbf{K}\mathbf{d}_i + \mathbf{H}\mathbf{z}_i = \mathbf{f}_i, \tag{4.1}$$

where $\mathbf{M}$, $\mathbf{C}$, $\mathbf{K}$ and $\mathbf{H}$ are the mass, damping, stiffness and hysteretic matrices, respectively (Triantafyllou and Koumousis, 2011). Furthermore, $\mathbf{f}_i$ is the external force vector, $\mathbf{d}_i$ is a vector of the displacement DOF and $\mathbf{z}_i$ is a vector of the hysteretic DOF at time-step i. Since the nonlinearities are represented through the hysteretic DOF, $\mathbf{K}$ and $\mathbf{H}$ need to be assembled only at the onset of each transient analysis.

4.2.2 State-space formulation

As mentioned in Chapter 1, a benefit of the elastic and hysteretic stiffness matrices being constant is that the set of second order differential equations shown in Eq. (4.1) can be straightforwardly converted into the state-space form, that is a set of first order nonlinear ODEs that can be augmented by the hysteretic evolution equations, after proper transformation to the global coordinates system as subsequently described, that collectively can be solved using any standard solvers, for example the 4th order Runge-Kutta method, to determine the unknown displacements, velocities, and hysteretic DOF in a step-wise fashion. Although the combined system of equations can be solved using any appropriate first and second order solution schemes (Newmark, 1959; Hughes and Liu, 1978; Chung and Hulbert, 1993), given the evolution equations are first order ODEs, and due to the possibility of expressing the governing dynamic equilibrium equations in state-space format such that the two can be conveniently combined into a system of first order equations, the first order ODE solvers are particularly desirable. As such, we define a vector, $\mathbf{x}_{i+1}$, that is an augmented set of unknowns containing $\mathbf{d}_{i+1}$, $\dot{\mathbf{d}}_{i+1}$ and $\mathbf{z}_{i+1}$ as:

$$\mathbf{x}_{i+1} = \begin{bmatrix} \mathbf{d}_{i+1}^T & \dot{\mathbf{d}}_{i+1}^T & \mathbf{z}_{i+1}^T \end{bmatrix}^T, \tag{4.2}$$

where the subscript $i+1$ represents the $(i+1)$th step. The collection of the equilibrium equations and the hysteretic evolution equations results in the following expression for the state-space formulation:

$$\dot{\mathbf{x}}_i = g(\mathbf{x}_i, t_i) = \mathbf{G}\mathbf{x}_i + \mathbf{b}_i, \tag{4.3}$$

where $\mathbf{G}$ is the system matrix expressed as follows:

$$\mathbf{G} = \begin{bmatrix} \mathbf{0}_{3r\times 3r} & \mathbf{I}_{3r\times 3r} & \mathbf{0}_{3r\times 4N} \\ -\mathbf{M}^{-1}\mathbf{K} & -\mathbf{M}^{-1}\mathbf{C} & -\mathbf{M}^{-1}\mathbf{H} \\ \mathbf{0}_{4N\times 3r} & \mathbf{U} & \mathbf{0}_{4N\times 4N} \end{bmatrix}, \tag{4.4}$$

where $\mathbf{U}$ is the global assembly of element hysteretic evolution equations. In Eq. (4.4), r and N are the number of nodes and total number of elements in the domain, respectively. In state-space form, $\mathbf{b}_i$ represents the input vector and is expressed as:

$$\mathbf{b}_i = \begin{bmatrix} \mathbf{0}_{1\times 3r} & \mathbf{f}_i^T\mathbf{M}^{-T} & \mathbf{0}_{1\times 4N} \end{bmatrix}^T. \tag{4.5}$$

The solution to the transient analysis is obtained using the 4th order Runge-Kutta method where the state vector is updated in a step wise fashion according to:

$$\mathbf{x}_{i+1} = \mathbf{x}_i + \frac{\Delta t}{6}\left(\mathbf{n}_1 + 2(\mathbf{n}_2 + \mathbf{n}_3) + \mathbf{n}_4\right), \tag{4.6}$$

where Δt is the time-step size. The derivatives of the Runge-Kutta 4th order update, $\mathbf{n}_1$ through $\mathbf{n}_4$, in Eq. (4.6) are evaluated using the expression in Eq. (4.3), with the following inputs for each derivative:

$$\begin{aligned} &\mathbf{n}_1 = g\Big(\mathbf{x}_i, t_i\Big), \quad \mathbf{n}_2 = g\Big(\mathbf{x}_i + 0.5\mathbf{n}_1\Delta t, t_i + 0.5\Delta t\Big), \\ &\mathbf{n}_3 = g\Big(\mathbf{x}_i + 0.5\mathbf{n}_2\Delta t, t_i + 0.5\Delta t\Big), \quad \mathbf{n}_4 = g\Big(\mathbf{x}_i + \mathbf{n}_3\Delta t, t_i + \Delta t\Big). \end{aligned} \tag{4.7}$$

The global mass matrix in Eq. (4.4) is an assembly of the concentrated and consistent mass matrices, according to:

$$\mathbf{M} = \hat{\mathbf{M}} + \mathbf{M}_c, \tag{4.8}$$

where $\hat{\mathbf{M}}$ is the diagonal matrix of concentrated mass(es) and the consistent mass matrix, $\mathbf{M}_c$, is assembled from the element matrices. The element consistent mass matrix in local coordinates is expressed as:

$$\mathbf{M}_c^{el} = \frac{\nu a L}{420}\begin{bmatrix} 140 & 0 & 0 & 70 & 0 & 0 \\ 0 & 156 & 22L & 0 & 54 & -13L \\ 0 & 22L & 4L^2 & 0 & 13L & -3L^2 \\ 70 & 0 & 0 & 140 & 0 & 0 \\ 0 & 54 & 13L & 0 & 156 & -22L \\ 0 & -13L & -3L^2 & 0 & -22L & 4L^2 \end{bmatrix}, \tag{4.9}$$

where ν, a and L are material density, cross sectional area, and element length, respectively. The matrix shown in Eq. (4.9) must be transformed to the global coordinates system which is accomplished following the traditional coordinate transformation as:

$$\mathbf{M}_c^e = \mathbf{\Lambda}^T \mathbf{M}_c^{el} \mathbf{\Lambda}. \tag{4.10}$$

The matrix $\mathbf{U}$ in Eq. (4.4), is being assembled from the evolution equations for each element, shown in Eq. (2.32). Finally, $\mathbf{C}$ in Eq. (4.4) represents the viscous damping matrix that, in principle, can be assembled either assuming proportional damping, such as mass or Rayleigh, or through direct equilibrium of the discrete viscous damping elements generally resulting in a non-proportional damping matrix. In either case, the damping matrix then becomes a function of the design variables, $\mathbf{a}$. Although the effect of damping on the topology is the subject of ongoing research, for this study the viscous damping term is neglected.

4.2.3 Optimization problem and sensitivity formulations

As previously mentioned, the design problem considered here seeks to determine the beam element cross sectional areas, $\mathbf{a}$, that minimize the volume of the structural system subject to constraints, including a system-level displacement constraint. As such the topology optimization problem is stated as:

$$\begin{aligned}
\text{Find}: \quad & a_1, ..., a_N \\
\underset{\mathbf{a}}{\text{Minimize}}: \quad & v = \sum_{s=1}^{N} a_s L_s \\
\text{Subject to}: \quad & \mathbf{M}\ddot{\mathbf{d}}_i + \mathbf{K}\mathbf{d}_i + \mathbf{H}\mathbf{z}_i = \mathbf{f}_i \\
& \tilde{d}_{max} = \left(\sum_{j=1}^{n_m} \sum_{i=1}^{n_T} d_{ji}^{p} \right)^{\frac{1}{p}} \leq d_{limit} \\
& 0 < \rho_{min} < a \leq \rho_{max},
\end{aligned} \tag{4.11}$$

where v is the volume in the domain and $\mathbf{a}$ is a vector of design variables representing the individual element cross sectional areas, for a given iteration in the optimization process. In Eq. (4.11), equilibrium of the nonlinear structural system and the system-level displacement are imposed as constraints which relate the response of the system to the design variables. Nonlinear dynamic analysis is performed to establish equilibrium of the system and to evaluate the response using the methods described in the previous subsection. To reduce the complexity of optimization problems with multiple constraints and the computational effort required to obtain a solution, researchers have suggested strategies to aggregate multiple constraints into a single constraint. Among these, two common approaches are the p-norm function (Duysinx and Sigmund, 1998) and the Kreisselmeier–Steinhauser (KS) function (París et al., 2010). The KS-function returns an estimate of the maximum, positive or negative, from a vector of numbers. However, given the context of the design problem shown in Eq. (4.11), where the system displacement, irrespective of whether it is positive or negative, is constrained to a specific threshold value suggests the KS-function is not an appropriate choice, hence the p-norm function is employed in this study that returns an approximation of the maximum of the absolute value of the displacements. The system-level displacement constraint, second in Eq. (4.11), limits the estimated maximum displacement $\tilde{d}_{max}$ of specified DOF in the domain, throughout the transient analysis, to a specified value d_{limit}. This is accomplished by the p-norm function, where n_m is the number of constrained DOF and n_T is the number of time-steps.

Similar to the design problem in Chapter 3, each element's cross sectional area, a, is constrained in Eq. (4.11) between ρ_{min} and ρ_{max}, and the approach for relating the cross sectional area to other geometric properties for I-shaped cross-sections suggested by Changizi and Jalalpour (2017b) is adopted in this study and the regression curves for the median range are used for the numerical examples.

Gradient-based optimization can benefit from analytical sensitivities of the objective function and constraints with respect to the design variables. However, the exact form of the nonlinear ODEs shown in Eq. (2.15) include the signum function. Hence, a mathematical approximation is introduced to facilitate the derivation of analytical sensitivities that are continuous and differentiable everywhere. As introduced in Chapter 3, the signum function in the original expression of the H_2 in Eq. (2.16), is replaced by the hyperbolic tangent function for the interaction model, as follows:

$$H_2 = \gamma \tanh(\zeta \mathbf{m}^{h,T} \dot{\boldsymbol{\epsilon}}) + \beta, \tag{4.12}$$

where ζ is a coefficient that controls the shape of the hyperbolic tangent function in the proximity of zero. Assigning a large numerical value to ζ, closely approximates the signum function shape yet remains differentiable. Similar to the case of multiaxial, non-interaction model employed in Chapter 3, a value of 50 is specified for ζ for all numerical examples.

The equilibrium and displacement constraints being differentiable permits the derivation of analytical sensitivities for gradient-based algorithms which is discussed in the subsequent subsection.

4.2.3.1 Sensitivities

Gradient-based optimization requires sensitivities with respect to the design variables, $\mathbf{a}$, and it is preferable, when possible to use analytical sensitivities. One of the motivating factors for adopting the hysteretic beam FE model for the structural analysis is the possibility to derive such analytical sensitivities with the previously mentioned mathematical approximation for the sgn function. In this section, the sensitivities for the optimization problem presented in Eq. (4.11) are developed, noting that obtaining the sensitivity of the objective function is straightforward and hence is omitted for brevity. The nonlinear transient analysis increases the complexity of deriving the sensitivities, relative to linear static, in particular due to presence of the hystertic DOF, evolution equations, hysteretic matrix and interaction functions for each element. The main challenge in deriving the sensitivities arises from the nonlinear constraint on the system-level displacement.

Differentiating the p-norm with respect to design variable, a, results in:

$$\frac{\partial \tilde{d}_{max}}{\partial a} = \frac{1}{p}\left(\sum_{j=1}^{n_m}\sum_{i=1}^{n_T} d_{ji}^p\right)^{\frac{1-p}{p}} \sum_{j=1}^{n_m}\sum_{i=1}^{n_T} p {d_{ji}}^{p-1}\frac{\partial d_{ji}}{\partial a}, \tag{4.13}$$

where the sensitivities for the displacements at each time-step, $\partial d_{ji}/\partial a$, were derived through direct differentiation of the augmented state vector, $\mathbf{x}_{i+1}$, with respect to a:

$$\frac{\partial \mathbf{x}_{i+1}}{\partial a} = \begin{bmatrix} \frac{\partial \mathbf{d}_{i+1}^T}{\partial a} & \frac{\partial \dot{\mathbf{d}}_{i+1}^T}{\partial a} & \frac{\partial \mathbf{z}_{i+1}^T}{\partial a} \end{bmatrix}^T, \tag{4.14}$$

where the term $\partial \mathbf{x}_{i+1}/\partial a$ is obtained by differentiation of Eq. (4.6) according to:

$$\frac{\partial \mathbf{x}_{i+1}}{\partial a} = \frac{\partial \mathbf{x}_i}{\partial a} + \frac{\Delta t}{6}\left(\frac{\partial \mathbf{n}_1}{\partial a} + 2\left(\frac{\partial \mathbf{n}_2}{\partial a} + \frac{\partial \mathbf{n}_3}{\partial a}\right) + \frac{\partial \mathbf{n}_4}{\partial a}\right), \tag{4.15}$$

and $\partial \mathbf{n}_1/\partial a$ through $\partial \mathbf{n}_4/\partial a$ are obtained by differentiating the state equations as follows:

$$\frac{\partial \dot{\mathbf{x}}_i}{\partial a} = \frac{\partial \mathbf{G}}{\partial a}\mathbf{x}_i + \mathbf{G}\frac{\partial \mathbf{x}_i}{\partial a}, \tag{4.16}$$

that is evaluated separately at the appropriate increments in time according to the 4th order Runge-Kutta method. The term $\partial \mathbf{G}/\partial a$ is obtained by differentiating Eq. (4.4) as follows:

$$\mathbf{G} = \begin{bmatrix} \mathbf{0}_{3r\times 3r} & \mathbf{0}_{3r\times 3r} & \mathbf{0}_{3r\times 4N} \\ -\frac{\partial \mathbf{M}^{-1}}{\partial a}\mathbf{K} - \mathbf{M}^{-1}\frac{\partial \mathbf{K}}{\partial a} & -\frac{\partial \mathbf{M}^{-1}}{\partial a}\mathbf{C} - \mathbf{M}^{-1}\frac{\partial \mathbf{C}}{\partial a} & -\frac{\partial \mathbf{M}^{-1}}{\partial a}\mathbf{H} - \mathbf{M}^{-1}\frac{\partial \mathbf{H}}{\partial a} \\ \mathbf{0}_{4N\times 3r} & \frac{\partial \mathbf{U}}{\partial a} & \mathbf{0}_{4N\times 4N} \end{bmatrix}. \tag{4.17}$$

The matrix $\partial \mathbf{M}^{-1}/\partial a$ in Eq. (4.17) is obtained as follows:

$$\frac{\partial \mathbf{M}^{-1}}{\partial a} = -\mathbf{M}^{-1}\frac{\partial \mathbf{M}_c}{\partial a}\mathbf{M}^{-1}, \tag{4.18}$$

where $\partial \mathbf{M}_c/\partial a$ is the global assembly of the element derivative matrices according to:

$$\frac{\partial \mathbf{M}_c^e}{\partial a} = \mathbf{\Lambda}^T \frac{\partial \mathbf{M}_c^{el}}{\partial a} \mathbf{\Lambda}$$

$$\frac{\partial \mathbf{M}_c^{el}}{\partial a} = \frac{\nu L}{420} \begin{bmatrix} 140 & 0 & 0 & 70 & 0 & 0 \\ 0 & 156 & 22L & 0 & 54 & -13L \\ 0 & 22L & 4L^2 & 0 & 13L & -3L^2 \\ 70 & 0 & 0 & 140 & 0 & 0 \\ 0 & 54 & 13L & 0 & 156 & -22L \\ 0 & -13L & -3L^2 & 0 & -22L & 4L^2 \end{bmatrix}. \tag{4.19}$$

The term $\partial \mathbf{U}/\partial a$ is assembled through the element level expressions, $\partial \mathbf{U}^{el}/\partial a$, and is expressed as:

$$\frac{\partial \mathbf{U}^{el}}{\partial a} = -\left(\frac{\partial H_1}{\partial a} H_2 \mathbf{R} + H_1 \frac{\partial H_2}{\partial a} \mathbf{R} + H_1 H_2 \frac{\partial \mathbf{R}}{\partial a} \right) \mathbf{B\Lambda}, \tag{4.20}$$

where $\partial H_1/\partial a$ is obtained for even values of n as follows:

$$\frac{\partial H_1}{\partial a} = n(\Phi + 1)^{n-1} \frac{\partial \Phi}{\partial a} \tag{4.21}$$

$$\frac{\partial \Phi}{\partial a} = 2.3 P_r \frac{\partial P_r}{\partial a} + 2M_r \frac{\partial M_r}{\partial a} + 3.67 \left(2P_r \frac{\partial P_r}{\partial a} M_r^2 + 2M_r \frac{\partial M_r}{\partial a} P_r^2 \right), \tag{4.22}$$

and the $\partial H_2/\partial a$ term is obtained as:

$$\frac{\partial H_2}{\partial a} = \zeta\gamma \Big(\frac{\partial \mathbf{m}^{h,T}}{\partial a} \dot{\boldsymbol{\epsilon}}_i + \mathbf{m}^{h,T} \frac{\partial \dot{\boldsymbol{\epsilon}}_i}{\partial a} \Big) \mathrm{sech}^2(\zeta \mathbf{m}^{h,T} \dot{\boldsymbol{\epsilon}}_i) \tag{4.23}$$

$$\frac{\partial \mathbf{m}^h}{\partial a} = \begin{bmatrix} \frac{\partial P^h}{\partial a} & \frac{\partial M^h}{\partial a} \end{bmatrix}^T, \quad \frac{\partial \dot{\boldsymbol{\epsilon}}_i}{\partial a} = \mathbf{B\Lambda} \frac{\partial \dot{\mathbf{d}}_i^e}{\partial a}. \tag{4.24}$$

For the sensitivity derivation, the interaction matrix, $\mathbf{R}$, is expressed as:

$$\mathbf{R} = R_f^{-1} \mathbf{R}_s, \quad R_f = \left(\frac{\partial \Phi}{\partial \mathbf{m}^h} \right)^T \mathbf{D} \frac{\partial \Phi}{\partial \mathbf{m}^h}, \quad \mathbf{R}_s = \frac{\partial \Phi}{\partial \mathbf{m}^h} \left(\frac{\partial \Phi}{\partial \mathbf{m}^h} \right)^T \mathbf{D}. \tag{4.25}$$

Thus, the sensitivity of $\mathbf{R}$ can be expressed as:

$$\frac{\partial \mathbf{R}}{\partial a} = -R_f^{-1} \frac{\partial R_f}{\partial a} R_f^{-1} \mathbf{R}_s + R_f^{-1} \frac{\partial \mathbf{R}_s}{\partial a}, \tag{4.26}$$

where the derivatives of the two components in Eq. (4.26) are:

$$\frac{\partial R_f}{\partial a} = \left(\frac{\partial^2\Phi}{\partial a \partial \mathbf{m}^h}\right)^T \mathbf{D} \frac{\partial \Phi}{\partial \mathbf{m}^h} + \left(\frac{\partial\Phi}{\partial \mathbf{m}^h}\right)^T \frac{\partial \mathbf{D}}{\partial a} \frac{\partial \Phi}{\partial \mathbf{m}^h} + \left(\frac{\partial\Phi}{\partial \mathbf{m}^h}\right)^T \mathbf{D} \frac{\partial^2 \Phi}{\partial a \partial \mathbf{m}^h} \tag{4.27}$$

$$\frac{\partial \mathbf{R}_s}{\partial a} = \frac{\partial^2\Phi}{\partial a \partial \mathbf{m}^h} \left(\frac{\partial\Phi}{\partial \mathbf{m}^h}\right)^T \mathbf{D} + \frac{\partial\Phi}{\partial \mathbf{m}^h} \left(\frac{\partial^2\Phi}{\partial a \partial \mathbf{m}^h}\right)^T \mathbf{D} + \frac{\partial\Phi}{\partial \mathbf{m}^h} \left(\frac{\partial\Phi}{\partial \mathbf{m}^h}\right)^T \frac{\partial \mathbf{D}}{\partial a}, \tag{4.28}$$

and the $\partial^2\Phi/\partial a \partial \mathbf{m}^h$ term in Eq. (4.28) is expressed as follows:

$$\frac{\partial^2\Phi}{\partial a \partial \mathbf{m}^h} = \left[2.3\left(\frac{\frac{\partial P^h}{\partial a} P_c^h - 2\frac{\partial P_c^h}{\partial a} P^h}{{P_c^h}^3}\right) + 7.34\left(\frac{2M_r \frac{\partial M_r}{\partial a} P_r}{P_u^h} + \frac{M_r^2 \frac{\partial P_r}{\partial a}}{P_u^h} - \frac{M_r^2 P_r \frac{\partial P_u^h}{\partial a}}{{P_u^h}^2}\right),\right.$$
$$\left. 2\left(\frac{\frac{\partial M^h}{\partial a} M_c^h - 2\frac{\partial M_c^h}{\partial a} M^h}{{M_c^h}^3}\right) + 7.34\left(\frac{2P_r \frac{\partial P_r}{\partial a} M_r}{M_u^h} + \frac{P_r^2 \frac{\partial M_r}{\partial a}}{M_u^h} - \frac{P_r^2 M_r \frac{\partial M_u^h}{\partial a}}{{M_u^h}^2}\right)\right]^T. \tag{4.29}$$

Last, the $\partial \mathbf{D}/\partial a$ is obtained straightforwardly as follows:

$$\frac{\partial \mathbf{D}}{\partial a} = \begin{bmatrix} E & 0 \\ 0 & E\frac{\partial I}{\partial a} \end{bmatrix}. \tag{4.30}$$

Eqs. (4.13) - (4.30), and the derivative of the objective function, omitted for brevity, comprise the analytical sensitivities for the optimization formulation. As can be seen in the presented derivations, the sensitivities of stiffness and hysteretic matrices do not vary with time at each nonlinear transient analysis that results in reduction in computational demand relative to the conventional plasticity approaches, where the tangent stiffness and its corresponding sensitivity need to be updated for each time-step.

4.2.4 Solution of the topology optimization process

With the requisite components developed in the previous sections, the problem formulation presented in Section 5.3.4 for the topology optimization of frame structures considering time-varying excitation and material nonlinearity is carried out using a multi-phase process. The steps for the optimization process are depicted by the flow diagram shown in Fig. 4.1. In this study, the Interior Point algorithm is employed by way of the `fmincon` function in MATLAB (The MathWorks Inc., 2018) with a specified tolerance of 10^{-6} on the objective function and the nonlinear constraint. The nonlinear dynamic analysis is carried out using the state-space equations outlined in Section 5.3.3 and the 4th order Runge-Kutta method. The optimization process begins with the densely connected ground structure with the area equally distributed amongst the many elements. The cross sectional areas, **a**, are constrained to minimum and maximum values of 0.914 and 159 in.^{2}, respectively, which correspond to median quantile of the I-shaped sections in the AISC manual (Changizi and Jalalpour, 2017b). Rather than perform a single phase of optimization and then post-process the results, that is removing elements with areas less than the lower constraint value, that could result in a design solution that does not satisfy the constraints, in this study multiple phases of optimization are performed to ensure the final optimized design satisfies the constraints. Following the first phase of the optimization process, elements with minimal cross sectional area are removed from the initial ground structure, without exceeding 5% of the total optimized volume, and an updated FE model is generated accordingly. Subsequent phases of the optimization process (see Fig. 4.1) are performed using an updated design configuration with minimal area elements from the prior phase having been removed. A converged design solution is achieved when no element in the topology has cross sectional area less than the lower constraint value and the topology connectivity remains unchanged throughout a given phase of optimization. To comply with the 5% removal criteria and to not cause sudden egregious degradation of the current design, the lower constraint value based on the minimum cross sectional area in AISC is gradually imposed so that the value of 0.914 in.^{2} is specified in the final phase of the optimization process. Dependent on the application, as few as two phases might be required to obtain a converged design solution that satisfies the constraints.

4.3 Numerical examples

The utility of the proposed methodology is demonstrated through several numerical examples for the design of structural frames composed of beam elements subject to pulse, harmonic and seismic base excitation. For each example the material is assumed to be steel with a Young's modulus of $29,000$ ksi, yield stress of 36 ksi and unit weight of 0.284 lb/in.^{3}. The inelastic to elastic ratios, α_u and α_ϕ, are set equal to 0.01. The hysteretic exponent n, is set equal to 2 and the exponent of the p-norm constraint, p, set as 40.

4.3.1 Example 1

The first example is the design of the lateral force resisting system for a 3×2 frame structure subject to a sinusoidal pulse base excitation. The ground structure, boundary

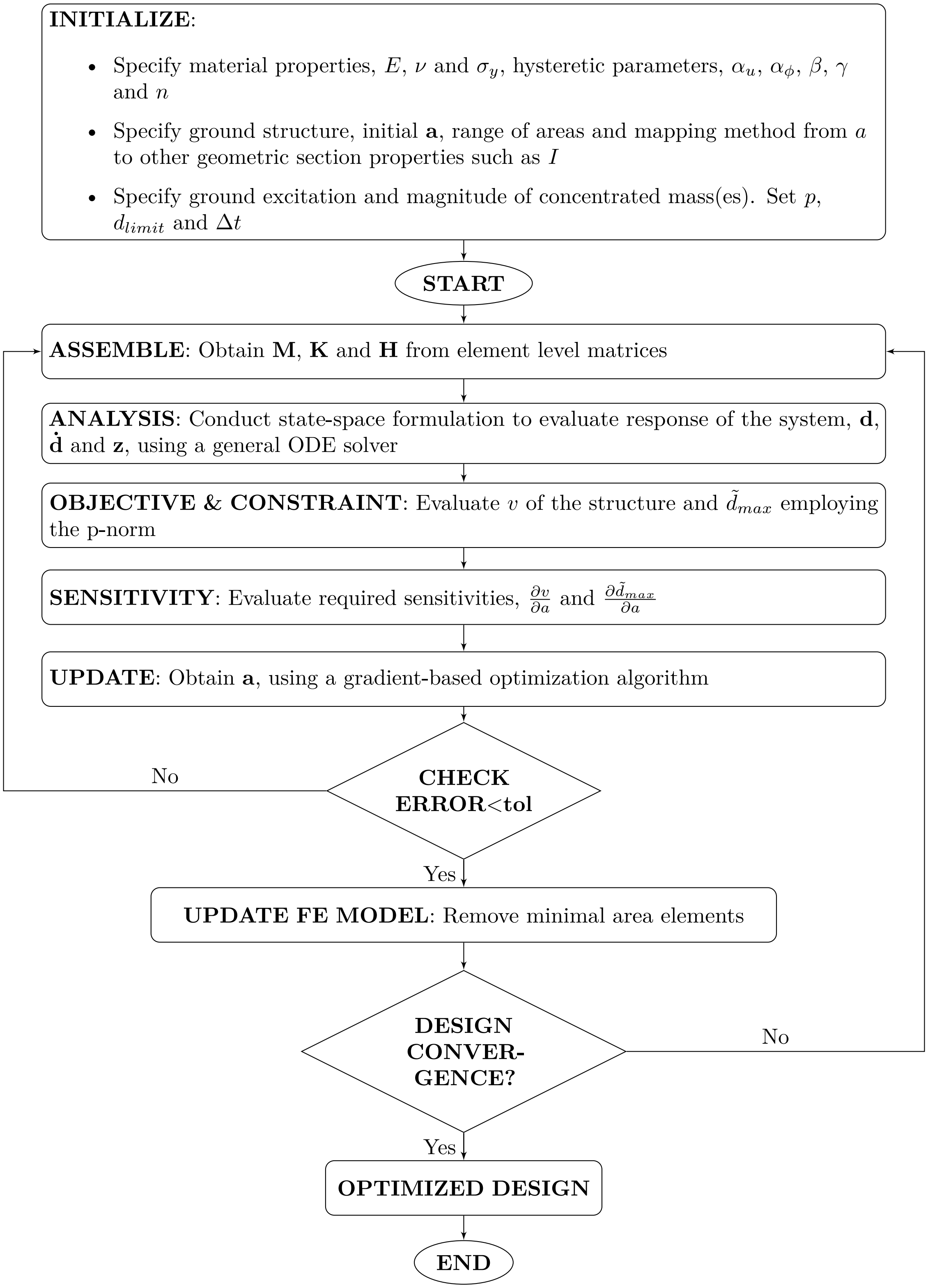

Figure 4.1: Flowchart for topology optimization solution scheme

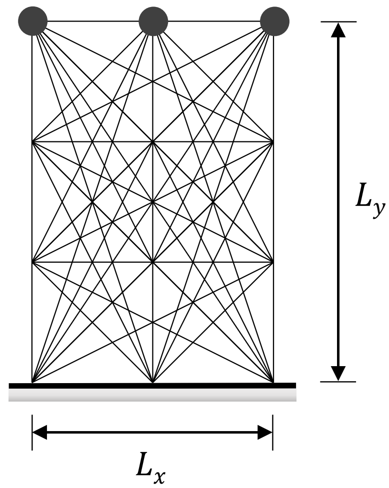

Figure 4.2: Ground structure for the 3×2 frame and position of concentrated masses

conditions, and location of the concentrated masses are shown in Fig. 4.2. The dimensions of the domain are $L_x = 13.12$ ft (4 m) and $L_y = 19.68$ ft (6 m).

The design problem shown in Eq. (4.11) is solved for the 3×2 frame structure, that is the determination of the element cross sectional areas that minimize the total volume subject to equilibrium, maximum displacement, and individual element area constraints. Three concentrated masses, each with magnitude of 100 kips (45.36 metric tonnes) are assigned to the nodes on the top of the domain in addition to individual element mass and mass moment of inertia. For this example, the maximum displacement of the concentrated mass in the middle of the domain, estimated through the p-norm, is constrained to d_{limit} that is set equal to 5.90 in., which is equivalent to a drift ratio of 2.5% (i.e., $d_{limit}/L_y = 0.025$). The time-varying excitation specified for this example is the sinusoidal pulse excitation shown in Fig. 4.3, that has a pulse duration of 1 s and amplitude of 0.25 times the gravitational acceleration constant. The overall duration of the excitation specified for the transient analysis is 2 s to ensure the maximum response was captured and $\Delta t = 0.002$ s to ensure stability of the Runge-Kutta method for all iterations and phases of the optimization process.

Prior to each example, the accuracy of the analytical sensitivities developed in Section 4.2.3.1 were evaluated by comparison to those obtained from a finite difference approximation. A sample comparison of the sensitivity values from the analytical expressions and numerical approximation for the displacement constraint for the 3×2 frame ground structure under pulse excitation are shown in Fig. 4.4. The element numbering is defined such that the elements connected to each node are concatenated in

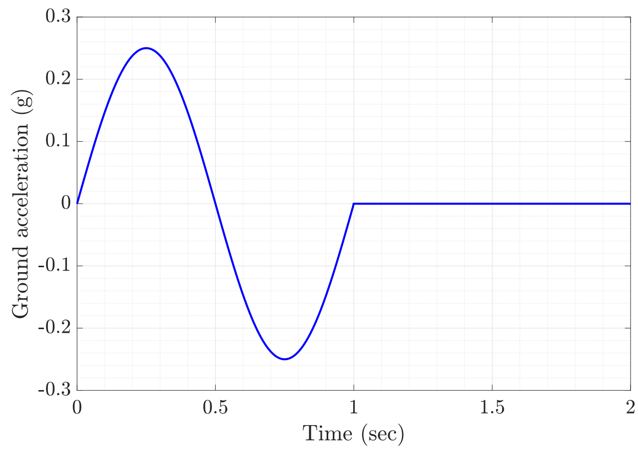

Figure 4.3: Pulse excitation

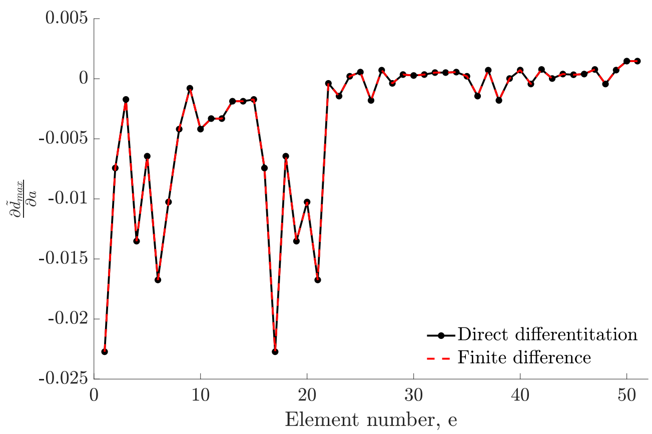

Figure 4.4: Comparison of the results of sensitivity analysis for the p-norm constraint derived with the analytical direct differentiation method and finite difference approximation for the 3×2 frame ground structure

the global element connectivity matrix. Node numbering starts from the bottom left of the domain and continues, row-wise, to the node on the top right. From Fig. 4.4, the derived sensitivities from the two methods can be seen to agree well with negligible error (less than 0.015%), thus verifying the accuracy of the analytical sensitivities obtained through the direct differentiation method in Section 4.2.3.1. For this example, 24 out of 51 elements are nonlinear, i.e., the combination of their internal axial force and bending moment reached the yield surface (Eq. (2.17) being equal to zero) for several time-steps throughout the analysis.

The optimization process was repeated on the 3×2 frame structure for different modeling assumptions of the material behavior, specifically, nonlinear with multiaxial interactions, nonlinear multiaxial, and linear-elastic. Details pertaining to the nonlinear multiaxial model is provided in Chapter 2. The resulting optimized topologies are shown in Fig. 4.5, where the line thickness of the elements comprising the topologies indicate the relative size of the element area, where the area values are normalized with respect to the maximum of all three designs shown. The optimized topology considering axial-moment interaction is shown on the left of Fig. 4.5, with a volume $v_{opt} = 1.4855 \times 10^5$ in.^{3} and multiple bracing elements connecting the middle mass to the supports and supporting elements. Relaxing the interaction between axial and bending moment, results in the optimized topology shown in the middle of Fig. 4.5, with a volume of $v_{opt} = 1.2929 \times 10^5$ in.^{3} and comparatively fewer bracing elements than with the multiaxial interaction case. As intuition would suggest, the multiaxial design requires less volume compared to the multiaxial interaction case to satisfy the displacement constraint, providing a degree of validation of the resulting topologies. The topology obtained from the linear design problem, shown on the right of Fig. 4.5, resembles the nonlinear multaxial design (middle), with the exception of the bracing elements 2 and 3 that have significantly smaller cross sectional area in the linear design than in the multiaxial nonlinear design. The optimal volume of the linear design is $v_{opt} = 1.1344 \times 10^5$ in.^{3}, the lowest of the three, because less volume is required to achieve the displacement constraint when the material remains linear-elastic for this design example. Additional design metrics and attributes, for the nonlinear and linear designs are provided in Fig. 4.5. For this example, the design with the largest volume is associated with nonlinear multiaxial interaction, whereas the design assuming linear-elastic material satisfies the constraint with 9.6% less volume relative to multiaxial interaction design. For each design, the value of the p-norm is approximately equal to $d_{limit} = 5.90$ in. However, due to the nature of the p-norm being an approximation for the actual maximum value, of the displacement response, d_{max}, is ≈ 5.24 in for nonlinear designs and ≈ 5.35 in for the linear design, which is less than $d_{limit} = 5.90$ in. Assigning a larger value to p, could result in closer agreement between $\tilde{d}_{max}$ to the actual maximum response, d_{max}, however, larger values of p can introduce numerical instabilities. In this study, we found a value of 40 to provide reasonable accuracy without introducing numerical instabilities.

The horizontal displacement response of the middle concentrated mass from nonlinear dynamic analysis performed on each of the optimized topologies shown in Fig. 4.5 subject to the pulse excitation shown in Fig. 4.3 are shown in Fig. 4.6. It can be seen from the responses shown in Fig. 4.6, that the maximum displacement for both nonlinear designs, that is multiaxial interaction and multiaxial, are ≈ 5.24 in., effectively satisfying the

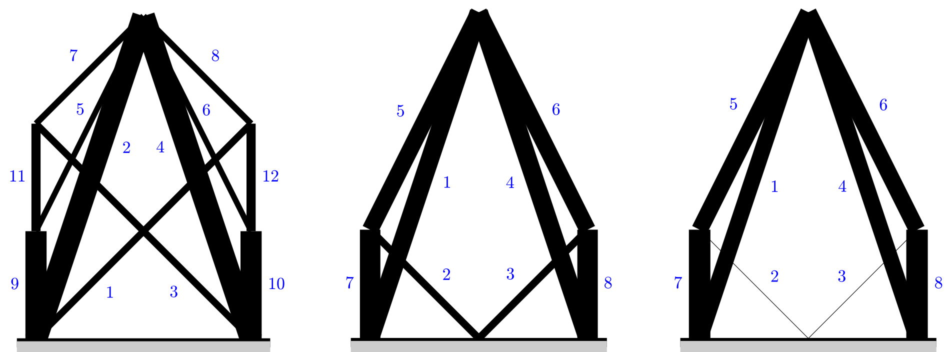

	Nonlinear		
	Multiaxial, interaction	Multiaxial	Linear
v_{opt} (in.^{3})	1.4855×10^5	1.2929×10^5	1.1344×10^5
N	12	8	8
a_{min} (in.^{2})	37.20	47.75	3.67
a_{max} (in.^{2})	149.33	133.81	140.58

Figure 4.5: Minimum volume designs (nonlinear and linear) for 2.5% system drift ratio for the 3×2 frame structure under pulse excitation for concentrated masses equal to 100 kips. Numerical values adjacent to structural elements denote the element number. A summary of design attributes is provided below each optimized structure

displacement constraint d_{limit}, whereas the maximum response of the linear design, when analyzed considering multiaxial interaction, is $\approx$ 7.21 in., significantly exceeding the constraint. The results shown in Chapter-5/Figures. 4.5 and 4.6 illustrate the importance of considering nonlinearity explicitly in the design problem and the effect of the various modeling assumption on the resulting designs in terms of topology, volume, and response.

In addition to the system level responses, element local axial force – axial strain and moment – curvature responses for the nonlinear designs are presented in Fig. 4.7. Also, shown in this figure are the axial-moment responses and yield function for two elements of the nonlinear multiaxial interaction design (Fig. 4.7a) and the nonlinear multiaxial design (Fig. 4.7b). Noting, the axial-moment responses presented are normalized by the hysteretic capacities, P_r and M_r. For both elements there is a combination of inelastic axial and curvature deformations simultaneously occurring and importantly, for the multaxial interaction case, the normalized hysteretic responses remain within or on, the Orbison yield function surface. In contrast, for the nonlinear multiaxial design, the

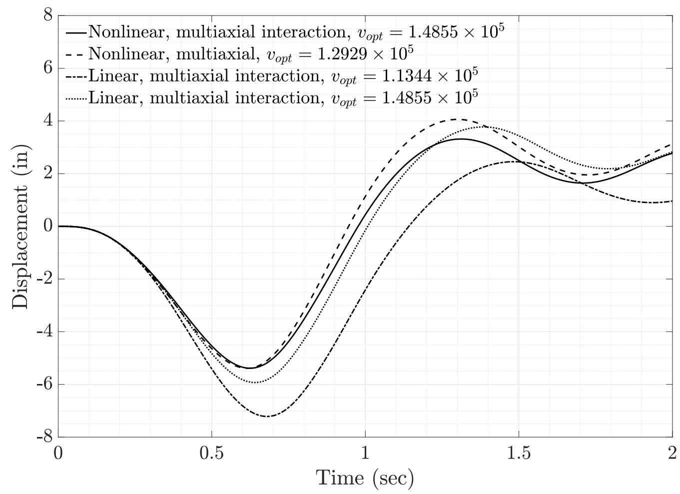

Figure 4.6: Nonlinear system displacement responses for the optimized designs of Example 1

normalized axial-moment responses are not constrained to the Orbison yield function, and hence reach the axial and moment capacities independent of each other thus violating the actual capacity of the element.

To further confirm the optimality of the nonlinear multiaxial interaction design, its volume is set as the constraint for a second linear optimization, details provided in Appendix C, where the objective is to minimize the maximum of the response $\tilde{d}_{max}$. Setting the volume constraint equal to 1.4855×10^5 in.^{3} for the linear design problem, results in a topology similar to that shown for the linear design on the right side of Fig. 4.5, with the only difference being the specific values of cross sectional areas of the elements. The linear design, with $v = 1.4855 \times 10^5$ in.^{3}, was evaluated by performing a nonlinear transient analysis considering multiaxial interaction resulting in a displacement response with a maximum value of $d_{max} = 5.93$ in. as shown in Fig. 4.6, 13% higher than the maximum of the displacement response for the nonlinear multiaxal interaction design. In other words, the linear design with a maximum displacement of 5.93 in. does not perform as well as the nonlinear mulitaxial interaction design with a maximum displacement of 5.24 in., despite the designs having the same volume.

4.3.2 Example 2

Here we present a second example to illustrate the effect of constraining all three concentrated masses. The domain with location of concentrated masses and excitation

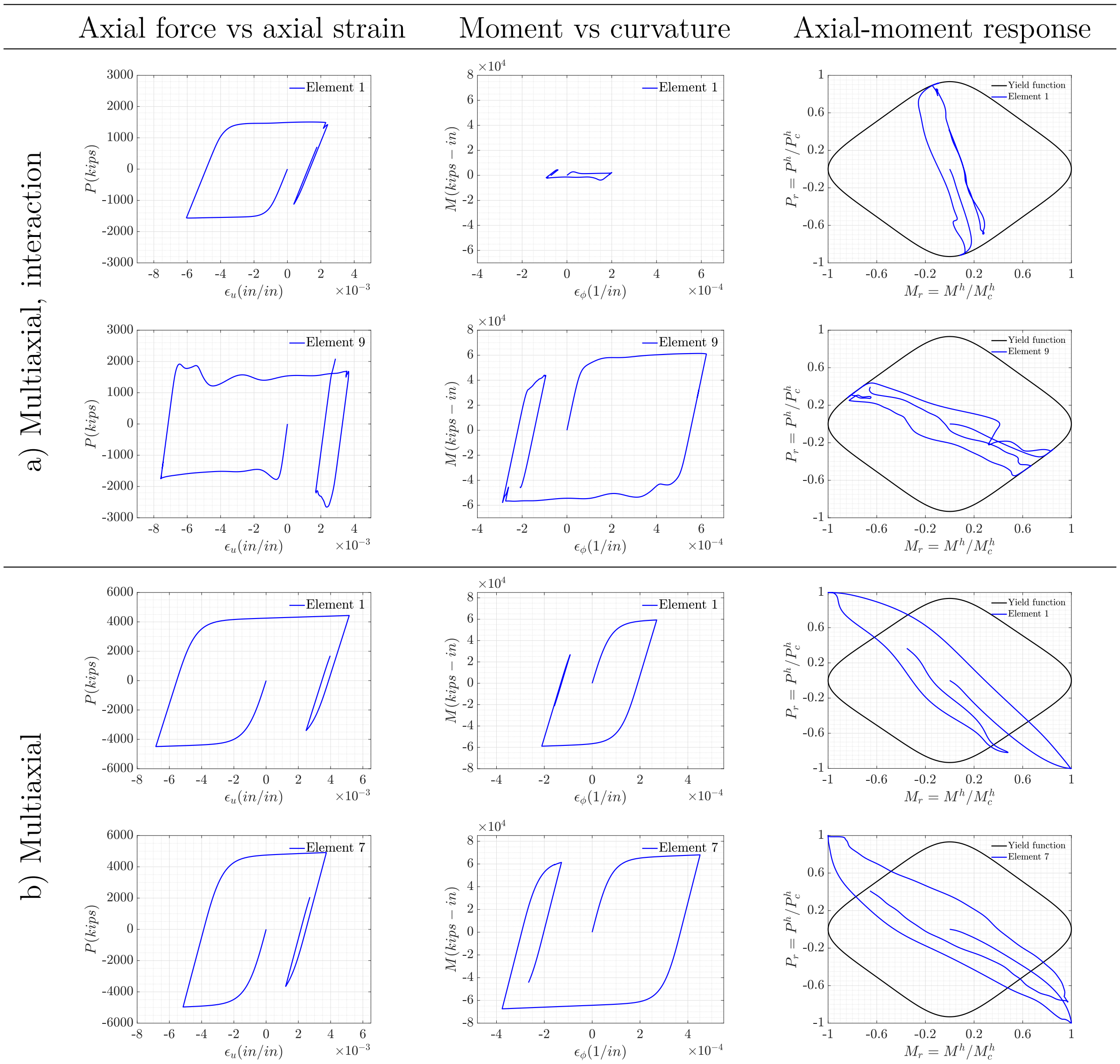

Figure 4.7: Axial force vs axial strain, and moment vs curvature diagrams of two selected elements for multiaxial, interaction (a) and multiaxial (b) nonlinear designs of 3×2 frame structure for 100 kips concentrated masses. Axial-moment response with the Orbison yield function also are shown on the right

are as shown in Chapter-5/Figures. 4.2 and 4.3, respectively. However, for this example, the three horizontal displacements associated to the three concentrated masses are combined into a single p-norm. The magnitude of each concentrated mass is set equal to 25 kips (11.34 tonnes), to prevent reaching the constraint on the maximum cross sectional area. Again, the specified constraint value (d_{limit}) is set equal to 5.90 in., equivalent to 2.5% drift. The resulting optimized topologies that is both nonlinear and linear designs,

	Nonlinear		
	Multiaxial, interaction	Multiaxial	Linear

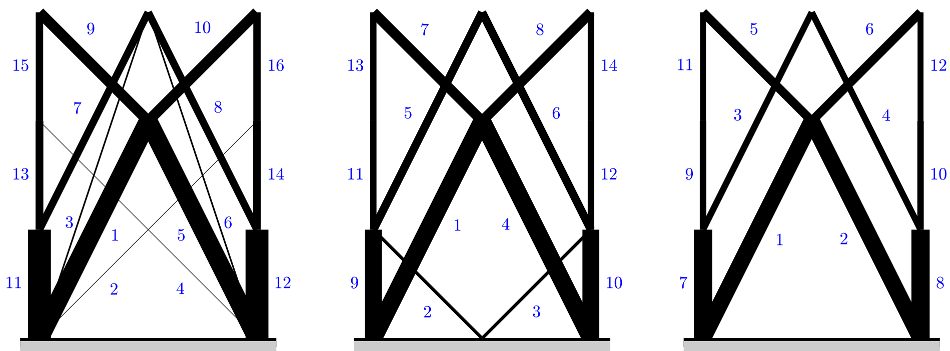

v_{opt} (in.^{3})	1.1449×10^5	1.0294×10^5	9.1288×10^4
N	16	14	12
a_{min} (in.^{2})	3.6	20.14	36.80
a_{max} (in.^{2})	141.25	107.77	112.96

Figure 4.8: Minimum volume designs (nonlinear and linear) for 2.5% system drift ratio for the 3×2 frame structure under pulse excitation for concentrated masses equal to 25 kips. Numerical values adjacent to structural elements denote the element number. A summary of design attributes is provided below each optimized structure

are shown in Fig. 4.8. For this design example, owing to the displacements of the three concentrated masses being constrained, all three designs include elements from the nodes where the concentrated masses are located to the supports and supporting elements to achieve a maximum displacement that satisfies the displacement constraint value, d_{limit}. As was seen from Example 1, in this example the nonlinear multiaxial interaction design is again comprised of the largest number of elements, 16 in total, including several diagonal bracing elements as well as having the largest volume of $v_{opt} = 1.1449 \times 10^5$ in.^{3}. The nonlinear multiaxial design satisfies the displacement constraint with less volume, in comparison to the mutilaxial interaction design, also with fewer elements, 14 in total comprising the optimized topology. Last, on the right, the linear design satisfies the displacement constraint with lowest volume of the three $v_{opt} = 9.1288 \times 10^4$ in.^{3}, and also the fewest number of elements with 12 in total when considering linear-elstic material behavior. Similar to the previous example, additional design metrics and attributes are provided for each design, including minimum and maximum cross sectional areas (a_{min} and a_{max}) in Fig. 4.8.

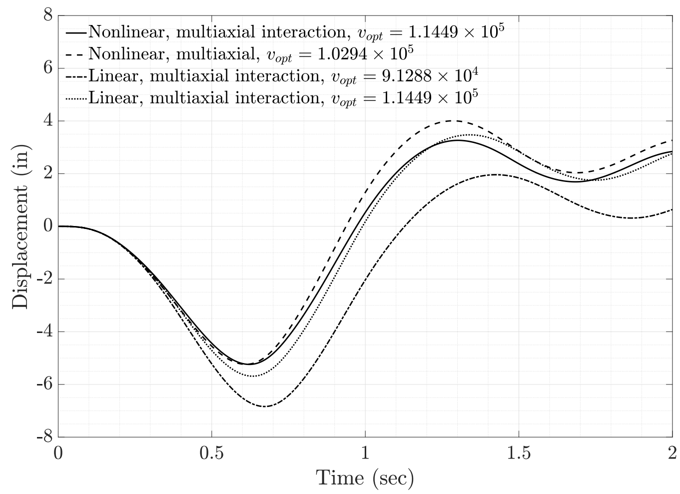

Figure 4.9: Nonlinear system displacement responses for the optimized designs of Example 2

The displacement responses of the concentrated mass exhibiting the actual maximum value, d_{max}, for each of the optimized topologies shown in Fig. 4.8 subject to the same pulse excitation (see Fig. 4.3) are shown in Fig. 4.9. These results are similar to those for Example 1 in that both nonlinear designs exhibit the same maximum displacement $\approx$ 5.23 in., that is again less than the specified constraint (5.90 in.), the difference being attributed due the p-norm being an approximation for the maximum value. As with Example 1, maximum response of the linear design evaluated through a nonlinear analysis with multiaxial interaction is $\approx$ 6.78 in., and significantly exceeds the specified displacement constraint value of 5.90 in.

To illustrate the impact of the modeling assumptions on the local element level responses, the axial force – strain and moment – curvature responses for two elements for each of the nonlinear designs in Fig. 4.8 are presented in Fig. 4.10 along with the normalized axial-moment responses and yield functions. As seen for Example 1, the normalized axial-moment responses for the nonlinear multiaxial interaction design, the values remain within, or on, the yield function surface. In contrast, the normalized axial-moment responses of the elements from the nonlinear multiaxial design violate the interaction surface because the actions are permitted to independently reach their hysteretic capacities.

As with Example 1, to verify importance of different volume allocation and element connectivity on the nonlinear design performance, the volume obtained from the nonlinear multiaxial, interaction design shown in Fig. 4.8, is set as the constraint for the second

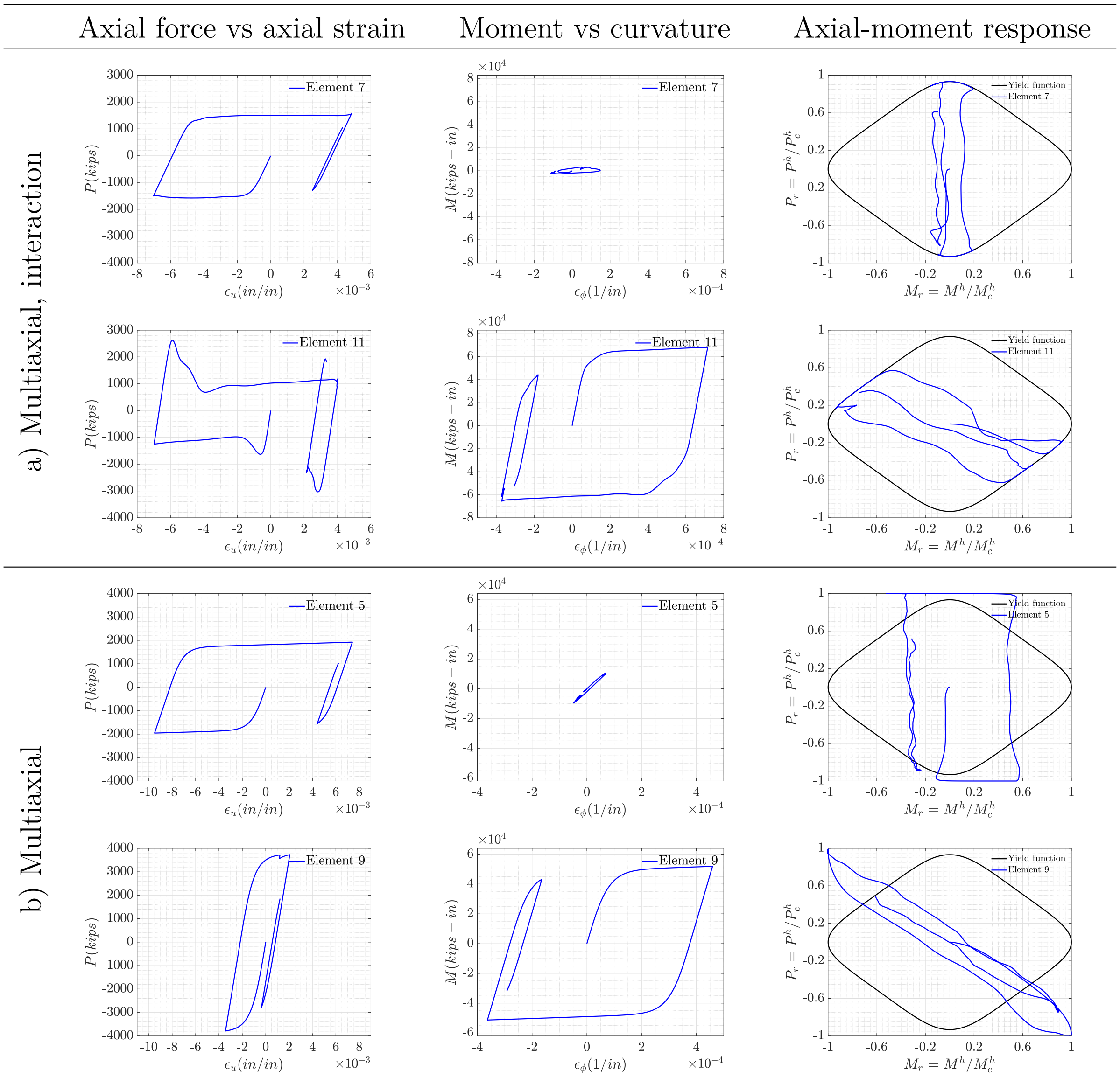

Figure 4.10: Axial force vs axial strain, and moment vs curvature diagrams of two selected elements for multi axial, interaction (a) and multiaxial (b) nonlinear designs of 3×2 frame structure for 25 kips concentrated masses. Axial-moment response with the Orbison yield function also are shown on the right

linear design problem presented in Appendix C by setting the $\tilde{d}_{max}$ as the objective. The result of the linear design problem with the total volume of 1.1449×10^5 in.^{3}, is again similar to the linear topology shown in Fig. 4.8, the only difference is being the specific values of cross sectional areas. The nonlinear interaction analysis is performed on the linear design, as the response is shown in Fig. 4.9, where d_{max} is equal to 5.64 in., 7.6% larger comparative to maximum response of the nonlinear multiaxal, interaction design.

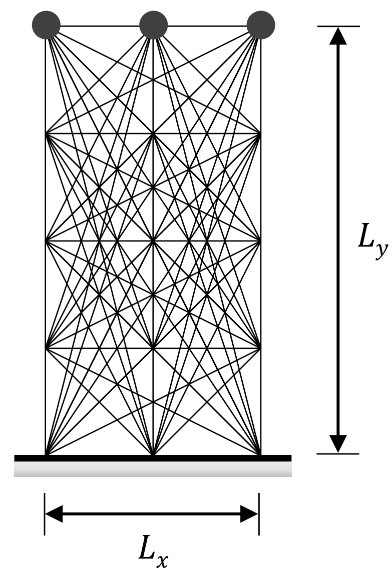

Figure 4.11: Ground structure for the 4×2 frame and position of concentrated masses

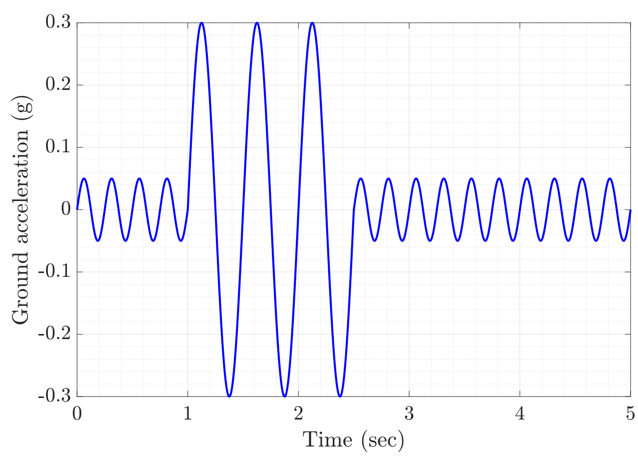

Figure 4.12: Harmonic excitation

Again, the nonlinear analysis of the linear design with $v = 1.1449 \times 10^5$ in.^{3} confirms the optimality of the nonlinear design, where even with the same volume, differences between the nonlinear design composition in comparison to the linear provide better performance.

A comparison of Example 1 and 2 illustrates the effect that constraining the mass(es) horizontal displacements has on the optimized topology. Specifically, if the displacement of a mass is not constrained then it is not necessary to allocate volume to that mass in an attempt to control its motion.

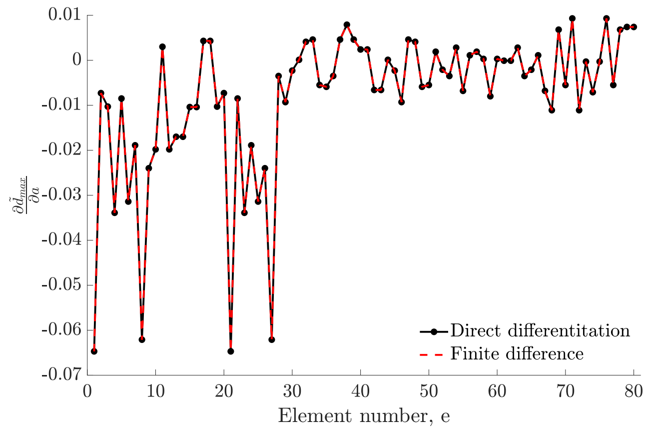

Figure 4.13: Comparison of the results of sensitivity analysis for the p-norm constraint derived with the analytical direct differentiation method and finite difference approximation for the 3×2 frame ground structure

4.3.3 Example 3

For this example, we are considering the design of the lateral force resisting system for a 4×2 frame structure subject to a harmonic base excitation. The ground structure, boundary conditions, and location of the concentrated masses are shown in Fig. 4.11, where the domain has dimensions of $L_x = 13.12$ ft (4 m) and $L_y = 26.25$ ft (8 m).

The volume minimization design problem shown in Eq. (4.11) is solved for the 4×2 frame structure. The magnitude of the three concentrated masses is set equal to 100 kips and are assigned to the nodes on the top of the domain in addition to individual element mass and mass moment of inertia. The estimated maximum through the p-norm function is constrained to d_{limit} of 7.87 in., again equivalent to a drift ratio of 2.5%. The time-varying excitation specified for this example is the harmonic excitation shown in Fig. 4.12 with duration of 5 s and maximum amplitude of 0.3 times the gravitational acceleration constant, with the time-step size equal to $\Delta t = 0.002$ s.

Similar to Example 1, the values of the sensitivities for the displacement constraint evaluated using the direct differentiation method are compared with numerical sensitivities obtained by finite difference approximation for the 4×2 ground structure under harmonic excitation. For comparison, these sensitivities are plotted in Fig. 4.13. As with Example 1, the sensitivities agree well with negligible relative error thus providing a verification of the accuracy of the analytical sensitivities obtained through the direct differentiation method described in Section 4.2.3.1. For this example, 46 out of 81 elements are nonlinear, i.e., the combination of their internal axial force and bending moment reached the yield

	Multiaxial, interaction	Linear
v_{opt} (in.^{3})	2.5223×10^4	2.6905×10^4
N	8	8
a_{min} (in.^{2})	12.61	14.51
a_{max} (in.^{2})	33.76	40.20

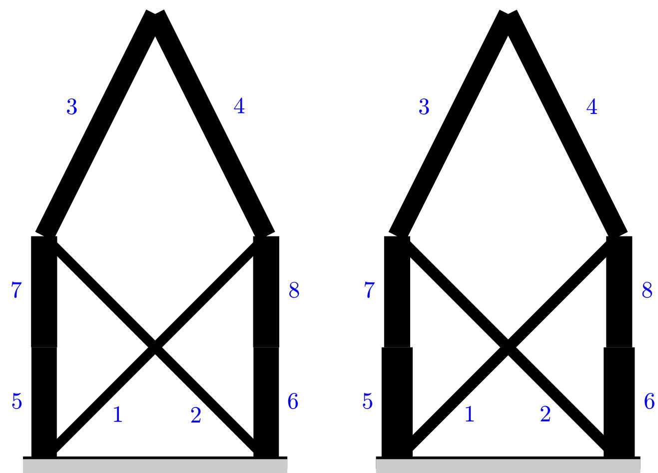

Figure 4.14: Minimum volume designs (nonlinear and linear) for 2.5% system drift ratio for the 4×2 frame structure under harmonic excitation for concentrated masses equal to 100 kips. Numerical values adjacent to structural elements denote the element number. A summary of design attributes is provided below each optimized structure

surface (Eq. (2.17) being equal to zero) for several time-steps throughout the analysis.

The resulting optimized topologies of 4×2 frame structure for nonlinear multiaxial interaction and linear-elastic assumptions are shown in Fig. 4.14. The optimized topology considering axial-moment interaction is shown on the left of Fig. 4.14, with $v_{opt} = 2.52334 \times 10^4$ in.^{3} and the linear design on the right with $v_{opt} = 2.6905 \times 10^4$ in.^{3}. Both optimized designs have the same composition of elements, the difference being the optimal volume and specific values of cross sectional areas. Interestingly, the optimal volume of the nonlinear design is lower than that of the optimal linear design, showing that the linear design problem overestimates the required volume when nonlinearity is considered. This result differs from that observed from Examples 1 and 2, where the volume was underestimated by linear design problem. To illustrate the difference in the proportions of cross sectional areas between the nonlinear and linear designs, the normalized values of cross sectional areas with respect to each design's maximum is reported in Table 4.1.

Table 4.1: Normalized values of cross sectional area with respect to each design maximum area for the optimized designs of 4×2 frame structure

	Element number							
	1	2	3	4	5	6	7	8
Nonlinear multiaxial interaction	0.37	0.37	0.76	0.76	0.97	0.97	1.00	1.00
Linear	0.36	0.36	0.62	0.62	1.00	1.00	0.84	0.84

The minimum area proportions correspond to elements 1 and 2, is common in both designs. However, the maximum proportions occur in two different elements, elements 7 and 8 for the nonlinear design and 5 and 6 for the linear design. Although the overall topologies are similar, however, the results confirm that factoring the areas in linear design to increase the volume, is not adequate when nonlinear design problem suggests different area proportions. Moreover, difference between maximum and other elements is larger in the linear design.

The displacement responses of the middle concentrated mass from nonlinear dynamic analysis performed on the optimized topologies shown in Fig. 4.14 subject to the harmonic excitation are shown in Fig. 4.15. It can be seen from the responses shown in this figure, that the maximum displacement for the nonlinear design, is $\approx$ 7.14 in., effectively satisfying the displacement constraint d_{limit}, whereas the maximum response of the linear design, when analyzed considering multiaxial interaction, is $\approx$ 7.27 in., exceeding the maximum of the nonlinear design, despite the linear design containing 6.7% larger volume.

Similar to Examples 1 and 2, element local axial force – axial strain and moment – curvature hysteretic responses for the nonlinear and linear designs of 4×2 frame structure by performing nonlinear (multiaxial interaction) dynamic analysis are presented in Fig. 4.16 along with the axial-moment responses and yield function for one selected elements of the nonlinear design (Fig. 4.16a) and the linear design (Fig. 4.16b). For both designs, the normalized axial-moment responses remain within, or on, the Orbison yield function surface. It is worth mentioning that the strain energy density in the nonlinear design is slightly larger than the linear design by 3.5%.

4.3.4 Example 4

For the last example, we are considering the design of the lateral force resisting system for a 2×1 frame structure subject to a recorded seismic ground motion. The ground

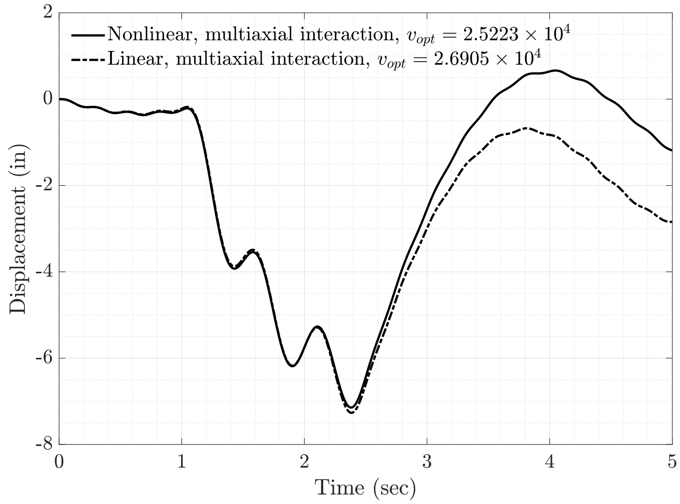

Figure 4.15: Nonlinear system displacement responses for the optimized designs of Example 3

	Axial force vs axial strain	Moment vs curvature	Axial-moment response
a) Nonlinear	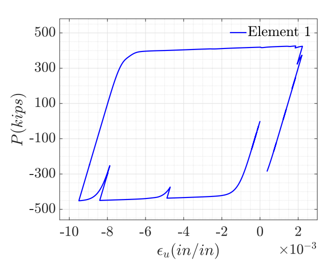	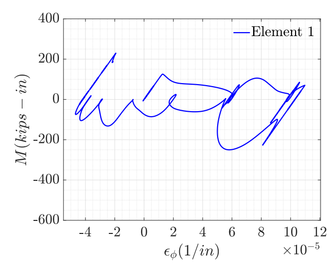	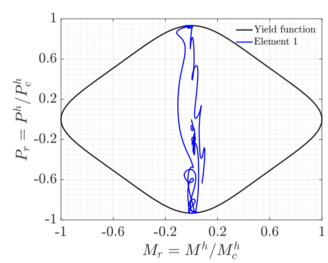
b) Linear	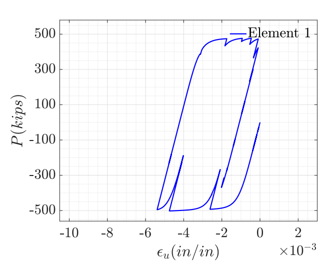	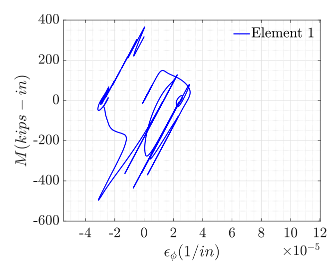	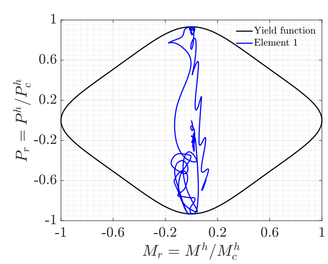

Figure 4.16: Axial force vs axial strain, and moment vs curvature diagrams of one selected element for nonlinear multiaxial, interaction (a) and linear (b) designs for 4×2 frame structure with 100 kips concentrated masses. Axial-moment response with the Orbison yield function also are shown on the right

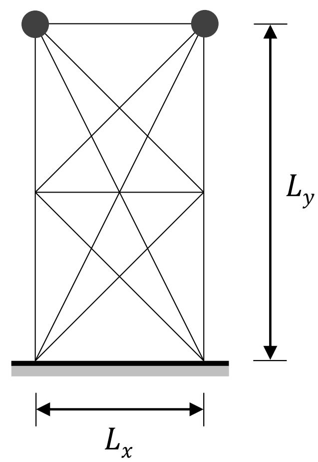

Figure 4.17: Ground structure for the 2×1 frame and position of concentrated masses

structure, boundary conditions, and location of the concentrated masses are shown in Fig. 4.17 with dimensions of $L_x = 6.56$ ft (2 m) and $L_y = 13.12$ ft (4 m).

Two concentrated masses are located at the top corner nodes, each corresponding to a weight of 25 kips, in addition to individual element mass and mass moment of inertia. Similar to the previous examples, the volume minimization design problem shown in Eq. (4.11) is solved for d_{limit} that for this example is equal to 3.94 in., equivalent to a drift ratio of 2.5%. The horizontal displacement of each mass is constrained to d_{limit} by combining the response of each mass in the p-norm function. The time-varying excitation specified for this example is the 1940 El Centro ground motion truncated to 4 s with maximum amplitude of $0.35g$ as shown in Fig. 4.18. Due to rapid fluctuation in the acceleration, and correspondingly in the displacement response, the original El Centro record was interpolated to a time-step size equal to $\Delta t = 0.0005$ s to ensure the maximum response is sufficiently captured by the nonlinear dynamic analysis. To avoid unnecessary computation, the ground motion was truncated after the strong motion portion.

The optimized designs of 2×1 frame structure obtained for the nonlinear multiaxial interaction and linear-elastic assumptions are shown in Fig. 4.19. Similar to Example 3, the element connectivity of both optimized designs are identical, however the volume and specific values of cross sectional areas differ. Specifically, the volume of the nonlinear design is 1.94 times that of the linear design volume.

The system level responses for the optimized designs of the 2×1 frame structure, evaluated using nonlinear dynamic analysis, under the El Centro excitation are presented in Fig. 4.20. Given the optimized designs and mass configuration are symmetric, the

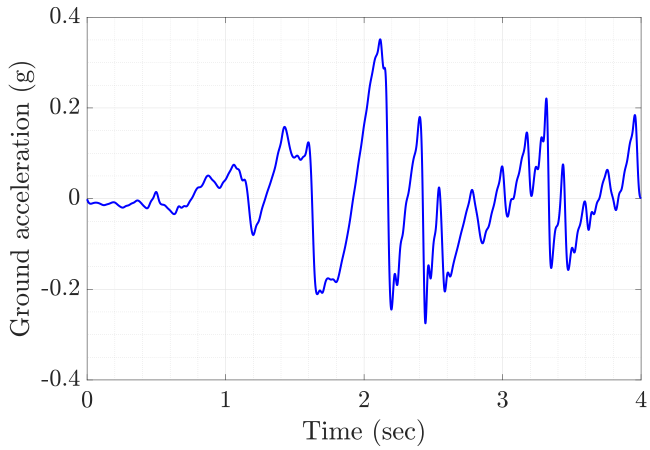

Figure 4.18: El Centro ground motion truncated to 4 seconds

	Multiaxial, interaction	Linear
	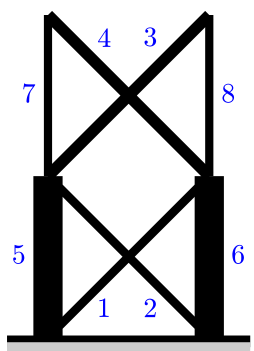	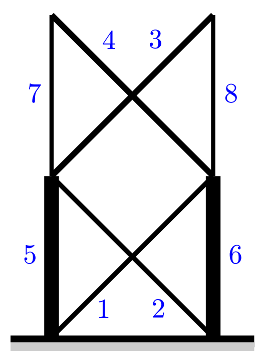
v_{opt} (in.^{3})	1.4706×10^4	0.7567×10^4
N	8	8
a_{min} (in.^{2})	11.60	5.97
a_{max} (in.^{2})	41.32	20.77

Figure 4.19: Minimum volume designs (nonlinear and linear) for 2.5% system drift ratio for the 2×1 frame structure under El Centro ground motion for concentrated masses equal to 25 kips. Numerical values adjacent to structural elements denote the element number. A summary of design attributes is provided below each optimized structure

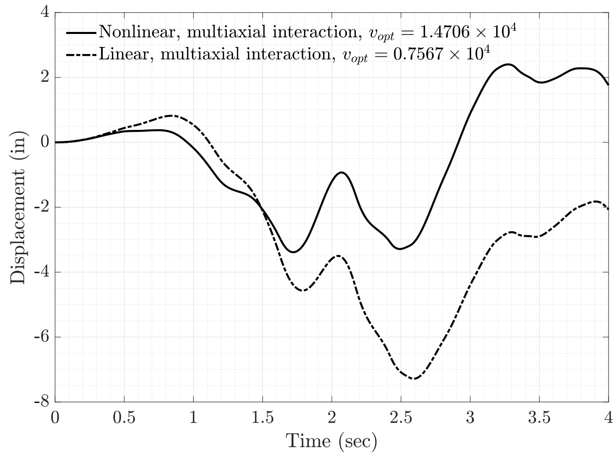

Figure 4.20: Nonlinear system displacement responses for the optimized designs of Example 4

horizontal displacement responses of the masses are nearly identical, as such the response of one of the mass is shown. The maximum displacement of the nonlinear design, is ≈ 3.38 in., effectively satisfying the displacement constraint, $d_{limit} = 3.94$ in., whereas the maximum response of the linear design, when analyzed considering nonlinear multiaxial interaction, is ≈ 7.28 in., exceeding both the d_{limit} and the maximum of the nonlinear design. This example further illustrates, as with Examples 1 & 2, that assuming linear elastic material in the optimization produces a design, that when evaluated by nonlinear dynamic analysis, exceeds the displacement limit d_{limit} and that the material nonlinearity, appropriately accounting for interaction, should be considered in the optimization process.

As with previous examples, element local axial force – axial strain and moment – curvature hysteretic responses for the nonlinear and linear designs of the 2×1 frame structure by performing nonlinear (multiaxial interaction) dynamic analysis are presented in Fig. 4.21 along with the axial-moment responses and yield function for one selected elements of the nonlinear design (Fig. 4.21a) and the linear design (Fig. 4.21b). Again, for both designs, the normalized axial-moment responses remain within, or on, the Orbison yield function surface.

4.4 Summary and concluding remarks

A method for the topology optimization of frame structures composed of nonlinear beam elements subjected to time-varying excitation is presented. The key contributions of the

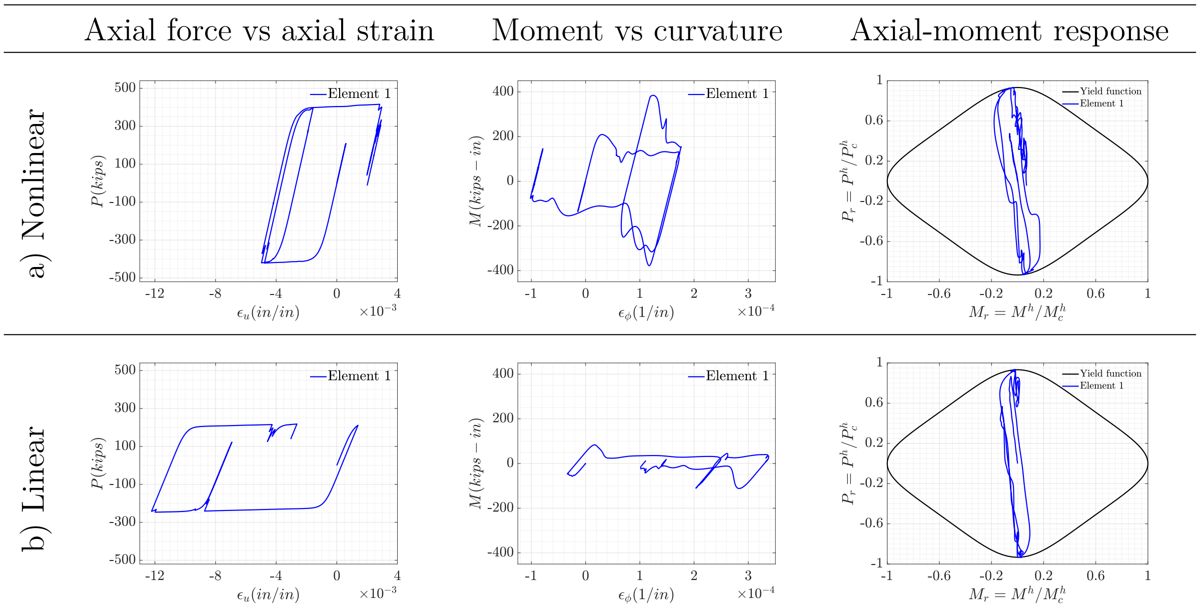

Figure 4.21: Axial force vs axial strain, and moment vs curvature diagrams of one selected element for nonlinear multiaxial, interaction (a) and linear (b) designs for 2×1 frame structure with 25 kips concentrated masses. Axial-moment response with the Orbison yield function also are shown on the right

design method developed in this Chapter are: (i) the integration of a hysteretic beam FE model, that accounts for axial-moment interaction and distributed plasticity, with gradient-based topology optimization including representing the governing nonlinear dynamic and hysteretic equations together in a state-space format that allows for the use of common ODE solvers without the need for any linearization or iteration; (ii) development of the corresponding sensitivities; and (iii) demonstration, through several numerical examples, the importance of considering material nonlinearity, including appropriate interaction and yield functions, for the design of frame structures where inelastic deformations are expected.

A volume minimization design formulation subject to a constraint on the maximum of the displacement response of a specified node(s) in the domain is presented. To ensure the constraint is differentiable, for the development of the analytical gradients, the p-norm operator that approximates the absolute value of the maximum of the entire displacement response is suggested and a mathematical approximation for the signum function in the hysteretic evolution equations is employed. The analysis and design formulations are general and can be suitable for different time-varying excitation as illustrated by the pulse, harmonic and El Centro excitation used in the numerical examples.

The utility of the proposed methodology is illustrated through several numerical examples. Optimized designs for different domains and constraints on the concentrated masses are found considering pulse and harmonic base excitation. For each numerical example the nonlinear design differs from the linear design in composition and/or area allocation. Furthermore, for each numerical example the nonlinear design outperforms the linear design, in terms of displacement response, when evaluated by nonlinear dynamic analysis even for the case when the volumes are the same. Importantly, the nonlinear designs obtained using the hysteretic FE beam model with multiaxial interaction respect the specified yield function. Interestingly, it was observed from one of the numerical examples that the nonlinear design could have an optimal volume less than the solution from a linear optimization problem yet outperform the linear design. This is because the allocation of area/volume not only affects the system's stiffness but also the amount of hysteretic energy dissipated by the design each contributing toward satisfying the specified constraint.

Chapter 5
Design Method for Dynamic Excitation Employing a Model Condensation

5.1 Introduction

When considering topology optimization for the dynamic setting, the material contributes to both the stiffness and inertia of the system and as such can result in a high-dimensional dynamic problem, in terms of DOF, that then increases the complexity of the optimization, in terms of the model evaluations and the design variables contributing to both the inertial and resisting force terms through the gradients. However, in certain applications the mass of the system being designed is order(s) of magnitude less than the supplemental mass the systems is being designed to support, for example, the structural design of building frames. For such cases, considering the consistent mass, that is the mass of the structure in addition to the supplemental mass adds unnecessary complexity and computational cost in the dynamic analysis and the optimization process. This is particularly challenge, when considering nonlinearity, in which the computational cost of the dynamic analysis is even greater than for the linear-elastic condition. For linear systems, traditional Guyan condensation approaches (Guyan, 1965; Rouch and Kao, 1980; McLean and Hahn, 1983; Sawicki and Gawronski, 1997), can be straightforwardly employed to reduce the dimensionality of the dynamic analysis, that is to condense the DOF to only those associated with concentrated mass, thereby neglecting the consistent mass. Guyan condensation is achieved With linear systems through partitioning of the system matrices according to those DOF with concentrated mass and algebraic substitution to reduce the DOF of the governing dynamic equations whereas the stiffness associated with DOF without concentrated mass is considered through an effective stiffness matrix which is a linear combination of sub-matrices of the stiffness matrix of the full system. However, for nonlinear systems, where material inelasticity is modeled according to traditional plasticity theory, condensation is less straightforward because the stiffness matrix is changing at each time step such that a large system of equations with many DOF including those associated with the concentrated and consistent mass of the structural system need to be simultaneously and directly analyzed. Some examples of condensation approaches for nonlinear systems have been suggested including, model reduction with local nonlinearity (Segalman, 2007), solution for von Kármán plates under quasi-steady fluid flow (Brake and Segalman, 2010), and for continuous systems via the augmentation by non-smooth basis functions (Brake and Segalman, 2013). However, these approaches either approximate the nonlinear forces or are tailored to specific applications.

Researchers have suggested various methods to consider material nonlinearity in topology optimization for quasi-static loading from early developments based on elasto-placticity (Maute et al., 1998; Schwarz et al., 2001; Yuge and Kikuchi, 1995), to more recent extensions considering plasticity methods (Nakshatrala et al., 2013; Li et al., 2017). However, for dynamic excitation, challenges corresponding to the optimization methods arise from the time-varying nature of the external forces that complicates the analysis for response evaluation and gradient expressions at each iteration of optimization (Min et al., 1999; Allahdadian et al., 2012; Liu et al., 2015; Zhu et al., 2018). Although some studies have relaxed the linear material assumption for dynamic excitation in topology optimization (Pedersen, 2003, 2004; Nakshatrala and Tortorelli, 2015; Shobeiri, 2019), in these studies, nonlinearity is considered through plasticity formulations, and a Newton type scheme is employed to iteratively update the stiffness matrix, at each time-step, due to the non-constant stiffness matrix until convergence of a residual. Not only does the iterative scheme significantly increases the computational demand, in contrast to linear-elastic material assumption, because the stiffness matrix is changing with respect to the response of the system, a Guyan type condensation can not be straightforwardly implemented because of a lack of uniqueness in recovering the individual elements of the full system matrix. The consequence for design is that the model evaluations consider the full system DOF and the inertial terms of the consistent mass matrix are included in the gradients, both of which increase the computation and complexity of obtaining an optimized solution.

5.2 Overview

In this Chapter, a condensation approach for structural systems considering material nonlinearity with distributed plasticity and multiaxial interaction is presented with particular emphasis on integration with topology optimization for cases where the mass of the structural system is negligible compared to the supplemental mass the system is being designed to support. Condensation of the governing nonlinear dynamic equations is achieved by employing a hysteretic FE beam model (Triantafyllou and Koumousis, 2011, 2012b) where the beam element elastic stiffness matrix and hysteretic matrix are invariant, yet because inelasticity is treated through hysteretic variables thus facilitating a Guyan type condensation yet detailed element level inelastic responses are retained. The condensation approach is employed for the topology optimization of nonlinear structural frames where the objective of the design is to minimize the total volume in the domain such that the maximum of the displacement response, at specified nodes corresponding to concentrated masses in the domain, satisfy a specified displacement constraint (i.e., drift limit). The maximum of the displacement response at specified nodes in the domain throughout the time-varying analysis is estimated using a single p-norm facilitating the derivation of the gradient of the nonlinear constraint. As with previous Chapters, the ground structure approach for the topology optimization of truss and frame structures is employed. Furthermore, the governing dynamic equations are converted to state-space form and combine with the element hysteretic FE evolution equations to form a single system of first order nonlinear ODEs, that can be solved using any appropriate ODE solvers, such as the 4th order Runge-Kutta method, without the need for Jacobian updates and associated iteration at each time step of the dynamic analysis. The effectiveness of the suggested topology optimization method is demonstrated through applications for design of lateral force resisting systems of frame structures each with a unique concentrated mass configuration, domain and excitation. The numerical examples show the dimensionality of the nonlinear dynamic system can be effectively reduced and that, in conjunction with the p-norm, can produce designs that satisfy the displacement constraint. To illustrate the importance of considering material nonlinearity explicitly in design procedure, comparable topology optimization problems assuming linear-elastic material behavior, are solved to obtain optimized linear design solutions. The linear designs are then evaluated by nonlinear dynamic analysis to obtain their response(s) that are then compared to the response/performance of the nonlinear designs. In general, these comparisons show that the nonlinear designs both differ in composition and outperform the linear designs with equivalent volume, when assessed by nonlinear dynamic analysis.

The remainder of this Chapter is organized as follows. Section 5.3 presents the condensation approachology, beginning with the nonlinear dynamic equation of motion, condensation (model reduction) method for nonlinear structural systems and state-space representation of the overall dynamic and hysteretic system to efficiently analyze the reduced set of DOF at each iteration of optimization. This discussion is followed by statement of the optimization problem and the nonlinear displacement constraint strategy with the corresponding sensitivities to facilitate solution by gradient-based optimization routines. Section 5.4 provides several numerical examples to illustrate handling of a single or multiple concentrated masses in the system, limiting their motions via a single p-norm constraint, and the effects of considering nonlinearity explicitly in the design of lateral force resisting systems, and to illustrate the detailed element level inelastic response that is retained in spite of the condensation. Last, Section 5.6 discusses the observations from the presented examples and summarizes the contributions of the proposed method.

5.3 Methodology

This section presents the overall methodology that progresses from governing system-level nonlinear dynamic equilibrium equations, condensation approach and their representation in the state-space format to the optimization problem formulation and the corresponding sensitivities to facilitate employing gradient-based optimization algorithms.

5.3.1 Nonlinear dynamic equilibrium equations

The governing dynamic equilibrium equations for a nonlinear system of multi DOF, is a set of second order, nonlinear, non-homogeneous ODEs expressed as follows (Triantafyllou and Koumousis, 2011):

$$\mathbf{M}\ddot{\mathbf{d}}_i + \mathbf{C}\dot{\mathbf{d}}_i + \mathbf{K}\mathbf{d}_i + \mathbf{H}\mathbf{z}_i = \mathbf{f}_i, \tag{5.1}$$

where $\mathbf{M}$, $\mathbf{C}$, $\mathbf{K}$ and $\mathbf{H}$ are the mass, damping, stiffness and hysteretic matrices, respectively, $\mathbf{f}_i$ is the external force vector, $\mathbf{d}_i$ is a vector of the displacement DOF and $\mathbf{z}_i$ is a vector of the hysteretic DOF at time-step i. The matrix $\mathbf{M}$ can be assembled from elements consistent mass matrices with diagonal matrix of concentrated masses, and matrices $\mathbf{K}$ and $\mathbf{H}$ are assembly of element level matrices according to Eq. (2.29). Since the nonlinearities are represented through the hysteretic DOF, $\mathbf{K}$ and $\mathbf{H}$ need to be assembled only at the onset of each transient analysis and then remain constant thereafter. In this Chapter, the multiaxial interaction model presented in Chapter 2 is employed.

5.3.2 condensation approach

The mass matrix associated with Eq. (5.1) is an assembly of consistent and concentrated mass matrices. To condense the governing equations, those that need to be solved simultaneously, to only those unknown DOF associated with the concentrated masses, the displacement vector is partitioned into concentrated mass DOF and ignored consistent mass DOF as follows:

$$\mathbf{d} = \left[\begin{array}{cc} \mathbf{d}_m^T & \mathbf{d}_s^T \end{array} \right]^T, \tag{5.2}$$

where subscripts m and s correspond to DOF with and without concentrated mass, respectively. As such, the nonlinear dynamic equilibrium equations shown in (5.1) can be expressed, neglecting viscous damping, according to the partitioned displacement vector and its derivatives with respect to time as:

$$\left[\begin{array}{cc} \hat{\mathbf{M}} & 0 \\ 0 & 0 \end{array} \right] \left[\begin{array}{c} \ddot{\mathbf{d}}_m \\ \ddot{\mathbf{d}}_s \end{array} \right] + \left[\begin{array}{cc} \mathbf{K}_{mm} & \mathbf{K}_{ms} \\ \mathbf{K}_{sm} & \mathbf{K}_{ss} \end{array} \right] \left[\begin{array}{c} \mathbf{d}_m \\ \mathbf{d}_s \end{array} \right] + \left[\begin{array}{c} \mathbf{H}_m \\ \mathbf{H}_s \end{array} \right] \mathbf{z} = \left[\begin{array}{c} \mathbf{f}_m(t) \\ \mathbf{f}_s(t) \end{array} \right], \tag{5.3}$$

where $\hat{\mathbf{M}}$ is the global diagonal matrix of concentrated masses. In Eq. (5.3), subscripts represent the set of rows and columns, respectively. Thus, the condensed equations can be expressed as:

$$\hat{\mathbf{M}}\ddot{\mathbf{d}}_m + \mathbf{K}_{mm}\mathbf{d}_m + \mathbf{K}_{ms}\mathbf{d}_s + \mathbf{H}_m\mathbf{z} = \mathbf{f}_m(t) \tag{5.4}$$

$$\mathbf{K}_{sm}\mathbf{d}_m + \mathbf{K}_{ss}\mathbf{d}_s + \mathbf{H}_s\mathbf{z} = \mathbf{f}_s(t). \tag{5.5}$$

Assuming no nodal or inertia forces are associated with the set of s DOF, Eq. (5.5) can be solved for $\mathbf{d}_s$ obtained as:

$$\mathbf{d}_s = -\mathbf{K}_{ss}^{-1} \left(\mathbf{K}_{sm}\mathbf{d}_m + \mathbf{H}_s\mathbf{z} \right). \tag{5.6}$$

Substituting Eq. (5.6) into Eq. (5.4), and factoring the terms results in:

$$\hat{\mathbf{M}}\ddot{\mathbf{d}}_m + \hat{\mathbf{K}}\mathbf{d}_m + \hat{\mathbf{H}}\mathbf{z} = \mathbf{f}_m(t), \tag{5.7}$$

where $\hat{\mathbf{K}}$ and $\hat{\mathbf{H}}$ denote effective stiffness and hysteretic matrices, respectively, and are defined as follows:

$$\hat{\mathbf{K}} = \mathbf{K}_{mm} - \mathbf{K}_{ms}\mathbf{K}_{ss}^{-1}\mathbf{K}_{sm}, \quad \hat{\mathbf{H}} = \mathbf{H}_m - \mathbf{K}_{ms}\mathbf{K}_{ss}^{-1}\mathbf{H}_s. \tag{5.8}$$

Similarly, partitioning the $\mathbf{U}$ and $\dot{\mathbf{d}}$ in Eq. (2.30) based on m and s DOF results in:

$$\dot{\mathbf{z}} = \mathbf{U}_m \dot{\mathbf{d}}_m + \mathbf{U}_s \dot{\mathbf{d}}_s. \tag{5.9}$$

Substituting the derivative of Eq. (5.6) with respect to time, into Eq. (5.9), the following is obtained as:

$$\dot{\mathbf{z}} = \hat{\mathbf{U}} \dot{\mathbf{d}}_m, \tag{5.10}$$

$$\hat{\mathbf{U}} = \left(\mathbf{I} + \mathbf{U}_s \mathbf{K}_{ss}^{-1} \mathbf{H}_s\right)^{-1} \left(\mathbf{U}_m - \mathbf{U}_s \mathbf{K}_{ss}^{-1} \mathbf{K}_{sm}\right). \tag{5.11}$$

The matrices $\mathbf{U}_s$ and $\mathbf{U}_m$ are sub-matrices of $\mathbf{U}$, and are partitioned column-wise.

5.3.3 State-space formulation

The system of second order differential equations shown in (5.7) can be straightforwardly converted into the state-space form, that is a set of first order nonlinear ODEs and augmented with the first order evolution equations, Eq. (5.10), to form a combined system of first order nonlinear ODEs that can be solved using any standard ODE solver, for example the 4th order Runge-Kutta method, to determine the unknown displacements, velocities, and hysteretic DOF in a step-wise fashion. As such, let us define a vector, $\mathbf{x}$, that is comprised of the unknowns $\mathbf{d}_m$, $\dot{\mathbf{d}}_m$ and $\mathbf{z}$ as:

$$\mathbf{x} = \begin{bmatrix} \mathbf{d}_m^T & \dot{\mathbf{d}}_m^T & \mathbf{z}^T \end{bmatrix}^T. \tag{5.12}$$

The combination of the equilibrium equations and the hysteretic evolution equations results in the following expression for the state-space formulation:

$$\dot{\mathbf{x}}_i = g(\mathbf{x}_i, t_i) = \hat{\mathbf{G}} \mathbf{x}_i + \hat{\mathbf{b}}_i, \tag{5.13}$$

where $\hat{\mathbf{G}}$ is the system matrix expressed as follows:

$$\hat{\mathbf{G}} = \begin{bmatrix} \mathbf{0}_{n_m \times n_m} & \mathbf{I}_{n_m \times n_m} & \mathbf{0}_{n_m \times 4N} \\ -\hat{\mathbf{M}}^{-1}\hat{\mathbf{K}} & \mathbf{0}_{n_m \times n_m} & -\hat{\mathbf{M}}^{-1}\hat{\mathbf{H}} \\ \mathbf{0}_{4N \times n_m} & \hat{\mathbf{U}} & \mathbf{0}_{4N \times 4N} \end{bmatrix}. \tag{5.14}$$

In Eq. (5.14), n_m and N are the number of concentrated masses and total number of elements in the domain, respectively. In Eq. (5.13), $\hat{\mathbf{b}}_i$ represents the input vector that for ground excitation can be expressed as:

$$\hat{\mathbf{b}}_i = \begin{bmatrix} \mathbf{0}_{1\times n_m} & \mathbf{f}_m^T\hat{\mathbf{M}}^{-T} & \mathbf{0}_{1\times 4N} \end{bmatrix}^T. \tag{5.15}$$

The solution to the dynamic analysis is obtained using the 4th order Runge-Kutta method where the state vector is updated in a step-wise manner according to:

$$\mathbf{x}_{i+1} = \mathbf{x}_i + \frac{\Delta t}{6}\Big(\mathbf{n}_1 + 2(\mathbf{n}_2 + \mathbf{n}_3) + \mathbf{n}_4\Big), \tag{5.16}$$

where Δt is the time-step and $\mathbf{n}_1$ through $\mathbf{n}_4$ are the derivatives of the state equation, where detailed expressions provided in Eq. (4.7).

5.3.4 Optimization problem and sensitivity formulations

As previously mentioned, the design problem considered in this study seeks to determine the beam element cross sectional areas, $\mathbf{a}$, that minimize the volume of the structural system subject to constraints, including a system-level displacement constraint. As such the topology optimization problem is posed as:

$$\begin{aligned} \text{Find}: \quad & a_1, ..., a_N \\ \underset{\mathbf{a}}{\text{Minimize}}: \quad & v = \sum_{s=1}^{N} a_s L_s \\ \text{Subject to}: \quad & \hat{\mathbf{M}}\ddot{\mathbf{d}}_m + \hat{\mathbf{K}}\mathbf{d}_m + \hat{\mathbf{H}}\mathbf{z} = \mathbf{f}_m \\ & \tilde{d}_{max} = \left(\sum_{j=1}^{n_m}\sum_{i=1}^{n_T}(\lambda_j d_{ji})^p\right)^{\frac{1}{p}} \leq d_{limit} \\ & 0 < \rho_{min} < a \leq \rho_{max}, \end{aligned} \tag{5.17}$$

where v is the volume in the domain and $\mathbf{a}$ is a vector of design variables representing the individual element cross sectional areas. The first constraint in Eq. (5.17) represents equilibrium of the condensed nonlinear system. Nonlinear dynamic analysis is performed to establish equilibrium of the system and to evaluate the response using the methods described in the previous subsection. The second constraint in Eq. (5.17), constrains nodal displacement(s) to a specified value d_{limit}. For the second constraint, the estimated maximum of the value of displacement(s), $\tilde{d}_{max}$, is estimated using the p-norm, where n_T is the number of time-steps specified for the dynamic analysis.

To effectively constrain concentrated masses displacements at different locations,

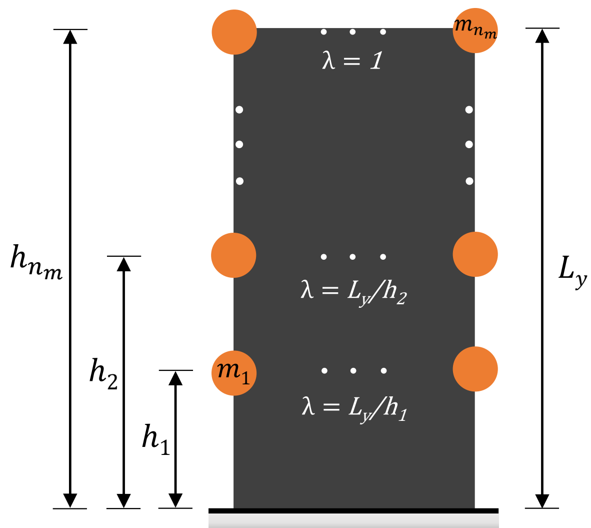

Figure 5.1: Illustration of the suggested strategy to constrain concentrated masses displacements at different heights with respect to the base of the structure using factor λ

relative to the base of the structural system, a constraint can be specified for each mass. However, multiple nonlinear constraints complicate the optimization problem and hence obtaining the solution. Instead, here the displacements of the concentrated masses located at different heights, are constrained through a single constraint, where the concentrated mass(es) maximum height, specifies d_{limit}, and the displacements are multiplied by a factor of $\lambda_j = L_y/h_j$ that appropriately adjusts the different level displacements, all collected in one p-norm. An illustration of this strategy is shown in Fig. 5.1.

The third constraint in Eq. (5.17), constrains each element cross sectional area between ρ_{min} and ρ_{max}, and similarly, the approach suggested by Changizi and Jalalpour (2017b) for I-shaped sections is adopted in this study and the regression curves for the median range are used for the numerical examples.

5.3.4.1 Sensitivities

To employ gradient-based optimization, analytical sensitivities with respect to the design variable, a, are developed via direct differentiation method. The sensitivity of the objective function can be obtained in a straightforward manner and hence is omitted for brevity. As such, the focus of this discussion is on deriving the sensitivities for the system level displacement constraint using the p-norm. Differentiating the p-norm with respect to design variable, a, results in:

$$\frac{\partial \tilde{d}_{max}}{\partial a} = \frac{1}{p}\left(\sum_{j=1}^{n_m}\sum_{i=1}^{n_T}(\lambda_j d_{ji})^p\right)^{\frac{1-p}{p}} p\sum_{j=1}^{n_m}\sum_{i=1}^{n_T}(\lambda_j d_{ji})^{p-1}\frac{\partial(\lambda_j d_{ji})}{\partial a}, \tag{5.18}$$

where $\partial d_{ji}/\partial a$ is derived through direct differentiation of the state vector, $\mathbf{x}$, with respect to a:

$$\frac{\partial \mathbf{x}}{\partial a} = \begin{bmatrix} \frac{\partial \mathbf{d}_m^T}{\partial a} & \frac{\partial \dot{\mathbf{d}}_m^T}{\partial a} & \frac{\partial \mathbf{z}^T}{\partial a} \end{bmatrix}^T, \tag{5.19}$$

where the term $\partial\mathbf{x}/\partial a$ is obtained by differentiation of Eq. (4.6) and updated according to:

$$\frac{\partial \mathbf{x}_{i+1}}{\partial a} = \frac{\partial \mathbf{x}_i}{\partial a} + \frac{\Delta t}{6}\left(\frac{\partial \mathbf{n}_1}{\partial a} + 2\left(\frac{\partial \mathbf{n}_2}{\partial a} + \frac{\partial \mathbf{n}_3}{\partial a}\right) + \frac{\partial \mathbf{n}_4}{\partial a}\right), \tag{5.20}$$

and $\partial\mathbf{n}_1/\partial a$ through $\partial\mathbf{n}_4/\partial a$ are obtained by differentiating the state equation as follows:

$$\frac{\partial \dot{\mathbf{x}}_i}{\partial a} = \frac{\partial \hat{\mathbf{G}}}{\partial a}\mathbf{x}_i + \hat{\mathbf{G}}\frac{\partial \mathbf{x}_i}{\partial a}, \tag{5.21}$$

that is evaluated separately for each derivative according to the 4th order Runge-Kutta method. The derivative of the system matrix, $\partial\hat{\mathbf{G}}/\partial a$, is obtained by differentiating Eq. (5.14) to obtain the following:

$$\frac{\partial \hat{\mathbf{G}}}{\partial a} = \begin{bmatrix} \mathbf{0}_{n_m\times n_m} & \mathbf{0}_{n_m\times n_m} & \mathbf{0}_{n_m\times 4N} \\ -\hat{\mathbf{M}}^{-1}\frac{\partial \hat{\mathbf{K}}}{\partial a} & \mathbf{0}_{n_m\times n_m} & -\hat{\mathbf{M}}^{-1}\frac{\partial \hat{\mathbf{H}}}{\partial a} \\ \mathbf{0}_{4N\times n_m} & \frac{\partial \hat{\mathbf{U}}}{\partial a} & \mathbf{0}_{4N\times 4N} \end{bmatrix}, \tag{5.22}$$

where $\partial\hat{\mathbf{K}}/\partial a$ and $\partial\hat{\mathbf{H}}/\partial a$ are obtained by differentiating Eq. (5.8) to obtain the following:

$$\begin{aligned} \frac{\partial \hat{\mathbf{K}}}{\partial a} &= \frac{\partial \mathbf{K}_{mm}}{\partial a} - \frac{\partial \mathbf{K}_{ms}}{\partial a}\mathbf{K}_{ss}^{-1}\mathbf{K}_{sm} - \mathbf{K}_{ms}\frac{\partial \mathbf{K}_{ss}^{-1}}{\partial a}\mathbf{K}_{sm} - \mathbf{K}_{ms}\mathbf{K}_{ss}^{-1}\frac{\partial \mathbf{K}_{sm}}{\partial a} \\ \frac{\partial \hat{\mathbf{H}}}{\partial a} &= \frac{\partial \mathbf{H}_m}{\partial a} - \frac{\partial \mathbf{K}_{ms}}{\partial a}\mathbf{K}_{ss}^{-1}\mathbf{H}_s - \mathbf{K}_{ms}\frac{\partial \mathbf{K}_{ss}^{-1}}{\partial a}\mathbf{H}_s - \mathbf{K}_{ms}\mathbf{K}_{ss}^{-1}\frac{\partial \mathbf{H}_s}{\partial a}, \end{aligned} \tag{5.23}$$

where the derivatives of partitioned matrices (e.g., $\partial\mathbf{K}_{mm}/\partial a$ and $\partial\mathbf{H}_m/\partial a$) are evaluated from $\partial\mathbf{K}/\partial a$ and $\partial\mathbf{H}/\partial a$. The $\partial\hat{\mathbf{U}}/\partial a$ term in Eq. (5.22) is obtained by differentiation of Eq. (5.11) expressed as:

$$
\begin{aligned}
\frac{\partial \hat{\mathbf{U}}}{\partial a} &= \left(\mathbf{I} + \mathbf{U}_s \mathbf{K}_{ss}^{-1} \mathbf{H}_s\right)^{-1} \left(\frac{\partial \mathbf{U}_s}{\partial a} \mathbf{K}_{ss}^{-1} \mathbf{H}_s + \mathbf{U}_s \frac{\partial \mathbf{K}_{ss}^{-1}}{\partial a} \mathbf{H}_s + \mathbf{U}_s \mathbf{K}_{ss}^{-1} \frac{\partial \mathbf{H}_s}{\partial a}\right) \\
&\quad \times \left(\mathbf{I} + \mathbf{U}_s \mathbf{K}_{ss}^{-1} \mathbf{H}_s\right)^{-1} \left(\mathbf{U}_m - \mathbf{U}_s \mathbf{K}_{ss}^{-1} \mathbf{K}_{sm}\right) + \left(\mathbf{I} + \mathbf{U}_s \mathbf{K}_{ss}^{-1} \mathbf{H}_s\right)^{-1} \\
&\quad \times \left(\frac{\partial \mathbf{U}_m}{\partial a} - \frac{\partial \mathbf{U}_s}{\partial a} \mathbf{K}_{ss}^{-1} \mathbf{K}_{sm} + \mathbf{U}_s \frac{\partial \mathbf{K}_{ss}^{-1}}{\partial a} \mathbf{K}_{sm} + \mathbf{U}_s \mathbf{K}_{ss}^{-1} \frac{\partial \mathbf{K}_{sm}}{\partial a}\right),
\end{aligned}
\tag{5.24}
$$

where $\mathbf{K}_{ss}^{-1}$ term and its derivatives are evaluated prior to each transient analysis due to constant stiffness matrix. The terms $\partial \mathbf{U}_m/\partial a$ and $\partial \mathbf{U}_s/\partial a$ are partitioned from $\partial \mathbf{U}/\partial a$, and are assembled through the element level expressions, $\partial \mathbf{U}^{el}/\partial a$, according to Eq. (4.20). Equations (5.18) - (5.24), and the derivative of the objective function, $\partial v/\partial a$, comprise the analytical sensitivities for use in gradient-based optimization solution algorithms described in the subsequent section.

5.3.5 Solution of the topology optimization process

Solving the design problem presented in Eq. (5.17) considering material nonlinearity and condensation is accomplished using a multi-phase process illustrated by the diagram shown in Fig. 5.2. In the initialization step, the material and hysteretic FE modelling parameters are specified, the domain and ground structure are selected and the initial values for the design variables are chosen. Furthermore, the concentrated mass(es) magnitude and configuration, and the ground excitation are specified. The remainder of the steps follow an iterative procedure, starting with assembling and partitioning the system level stiffness and hysteretic matrices accordingly. The nonlinear dynamic response of the system is obtained through solution of the state-space equations outlined in Section 5.3.3 and the 4th order Runge-Kutta method. The maximum displacement at certain DOF is approximated using the p-norm following the discussion in Section 5.3.4. The sensitivities are evaluated to guide the optimizer to search the next step. For each phase, the Interior Point algorithm is employed by way of the `fmincon` function in MATLAB (The MathWorks Inc., 2018) with a specified tolerance of 10^{-6} on the objective function and the nonlinear constraint. The design process begins with the densely connected ground structure (Bendsoe and Sigmund, 2004) with the initial volume equally distributed amongst the elements. The cross sectional areas, $\mathbf{a}$, are constrained to minimum and maximum values of 0.914 and 159 in.^{2}, respectively, which correspond to median quantile of the I-shaped sections in the AISC manual (Changizi and Jalalpour, 2017b). Following the first phase of the topology optimization process, elements with a cross sectional area

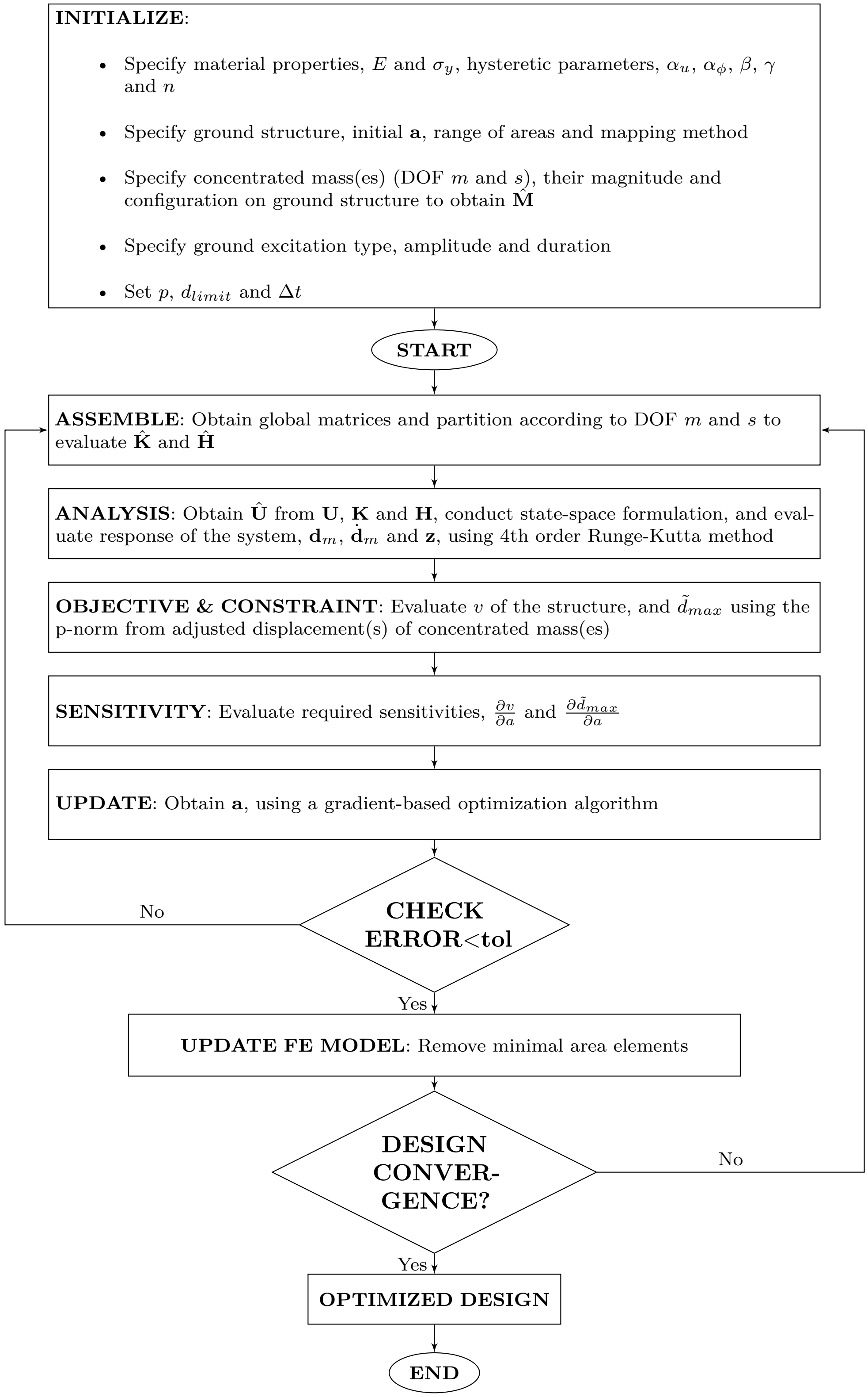

Figure 5.2: Flowchart for topology optimization solution scheme

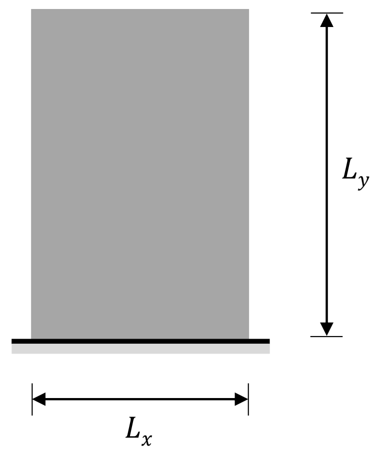

Figure 5.3: Illustration of frame domain and boundary conditions

less than or equal to ρ_{min} are removed from the initial ground structure, without exceeding 5% of the total optimized volume, and the FE model is updated accordingly to begin the second phase of the optimization process. Subsequent phases of the optimization process (see Fig. 5.2) are performed with updated FE model reflecting the current design with minimal area elements having been removed. A converged design solution is achieved when no element in the topology has minimal area and the topology connectivity remains unchanged throughout a given phase of optimization.

5.4 Numerical examples

The condensation approachology in the context of topology optimization is demonstrated through several numerical examples for the design of structural frames composed of beam elements, each example examining different arrangements of concentrated mass(es). For all examples, the material is assumed to be steel with a Young's modulus of $29,000$ ksi and yield stress of 36 ksi. The inelastic to elastic ratios, α_u and α_ϕ, are set equal to 0.01. The hysteretic exponent n, is set equal to 2 and the exponent of the p-norm, p, set as 40. The design domain and boundary conditions are shown in Fig. 5.3. A pulse base excitation, shown in Fig. 5.4, is specified as the input motion with an amplitude, A_p, and period, T_p, and the time step for the Runge Kutta integration is set equal to the time-step of $\Delta t = 0.002$ sec.

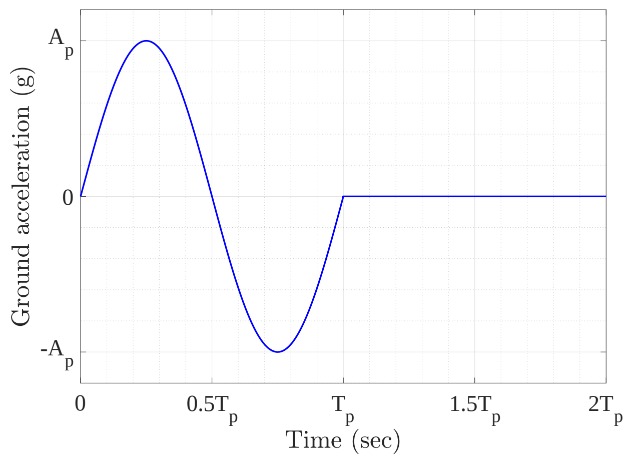

Figure 5.4: General pulse base excitation with amplitude A_p and period T_p

5.4.1 Application 1: 3×2 frame structure

The first application considers the design of the lateral force resisting systems for a frame structure that is discretized into 3 units in height by 2 units in width, herein referred to simply as 3×2, subject to a sinusoidal pulse base excitation shown in Fig. 5.4. For this application, the pulse amplitude is set equal to 0.25 times the gravitational acceleration constant, g, and the pulse period equal to 1 sec. The dimensions for the domain are $L_x = 13.12$ ft (4 m) and $L_y = 19.68$ ft (6 m). The design problem expressed in Eq. (5.17) is solved for a specified displacement constraint, d_{limit}, equal to 5.90 in., which is equivalent to a drift ratio of 2.5% (i.e., $d_{limit}/L_y = 0.025$).

For this domain and discretization, optimized designs are obtained for two mass configurations; a single concentrated mass located at the top, middle, of the domain (example A), and a system consists of two concentrated masses located at the top, corners, of the domain (example B). Each concentrated mass is assigned a value of 25000 lb. The presentation and associated discussion for the optimized designs obtained for each mass configuration are provided in the subsequent subsections.

5.4.1.1 Example A: single concentrated mass

For example A, we consider a single concentrated mass located at the top middle node, as shown on the ground structure in the left side of upper row in Fig. 5.5. As previously discussed, the p-norm is employed to approximate the maximum from the horizontal displacement response of the concentrated mass ($\lambda_1 = 1$). Prior to each example, the accuracy of the analytical sensitivities developed in Section 5.3.4.1 were evaluated by comparison to those obtained from a finite difference approximation. A comparison of the sensitivity values from the analytical expressions and numerical approximation for the displacement constraint on the ground structure under pulse excitation are shown in Fig. 5.6. Similar to comparisons provided in previous Chapters, again the derived sensitivities from the two methods agree well with negligible error, thus verifying the accuracy of the analytical sensitivities obtained through the direct differentiation method in Section 5.3.4.1. Solving the nonlinear formulation presented in Eq. (5.17), the optimized topology shown in the upper row of Fig. 5.5, referred to as the nonlinear design, is obtained. The topology is comprised of 6 elements that correspond to a volume of 3.087×10^4 in.^{3}. Additional attributes are summarized in Table 5.1. The objective function and displacement constraint values for each iteration throughout the entire optimization process, following the procedure shown in Fig. 5.2, for the nonlinear design is shown in Fig. 5.7. The periodic drop and rise of the objective and constraint values corresponds to the beginning of each phase of optimization. As can be seen from Fig. 5.7, the value of $\tilde{d}_{max} - d_{limit}$ is approximately zero at the final phase for each optimization process, illustrating that the optimized nonlinear design satisfies the specified displacement constraint, d_{limit}.

For comparison, two additional optimization problems were solved assuming linear-elastic material behavior. The first, a volume minimization design problem subject to a displacement constraint, again set equal to $d_{limit} = 5.90$ in., and the second a displacement minimization, p-norm as the objective, constrained to the volume of the optimized nonlinear design, 3.087×10^4 in.^{3}. The linear volume minimization design problem is similar to the nonlinear design method shown in Eq. (5.17), and the point of including this design problem for comparison is to compare the optimized topology and its performance when analyzed by nonlinear dynamic analysis. On the other hand, the linear displacement minimization design problem is solved to assess the nonlinear performance of the design obtained given the same volume as the nonlinear design and also to further investigate the optimality of the nonlinear design. Specific details with respect to the formulations for each linear design problem are provided in Appendix B. The optimized topology obtained from the linear volume minimization, referred to as linear design, is shown in Fig. 5.5, which is comprised of 4 elements with volume of 2.527×10^4 in.^{3}, and its attributes are summarized in Table 5.1. The line thickness for the topologies shown in Fig. 5.5 indicates the relative size of the elements cross sectional area normalized with respect to the maximum cross sectional area of the nonlinear and linear designs. From the shown topologies, both the nonlinear and linear optimized designs share a common load path, connecting the concentrated mass to the base supports, however, the nonlinear design includes two additional bracing type elements. The linear optimized design based on p-norm minimization is identical to the linear design for the volume minimization problem, with the exception of the specific values of areas being different and hence is not being shown.

5.4.1.2 Example B: two concentrated masses

For example B, two concentrated masses located at the top corner nodes of the domain are considered as shown on the ground structure in the lower row of Fig. 5.5. This example illustrates two points, first the condensation approach works for multiple concentrated masses and second, the p-norm can be effectively used to constrain the displacements of multiple masses that for this example are at the same height, with respect to the base. The optimized nonlinear design, obtained by constraining the horizontal displacements of both concentrated masses combined in the p-norm ($\lambda_1 = \lambda_2 = 1$), is shown in Fig. 5.5. As with example A, a comparison of the sensitivities derived from analytical expressions and finite difference approximation is shown in Fig. 5.6 that shows negligible error and verifies the accuracy of the sensitivities obtained from direct differentiation method. The topology of the nonlinear design is comprised of 10 elements with a corresponding volume of 6.574×10^4 in.^{3}. Additional attributes are summarized in Table 5.1. The optimization history in terms of the objective function and displacement constraint values for each iteration, for the nonlinear design is shown in Fig. 5.7. The periodic drop and rise of the objective and constraint corresponds to the beginning of each phase of optimization. The value of $\tilde{d}_{max} - d_{limit}$ is approximately zero at the final phase for each optimization process, illustrating that the optimized nonlinear design satisfies the specified displacement constraint, d_{limit}. The optimized linear design is also shown in the lower row of Fig. 5.5 that is comprised of 10 elements corresponding to a volume of 5.583×10^4 in.^{3}. The nonlinear and linear designs mainly differ in the volume allocated to the outer columns and the inner bracing type elements. Similar to example A, the design of linear p-norm minimization is obtained by setting the volume constraint to 6.574×10^4 in.^{3}, and the optimized topology is the same as the linear design shown in Fig. 5.5, with only cross sectional areas being different, and design attributes reported in Table 5.1.

Example	Ground structure and mass configuration	Nonlinear design	Linear design
(A)	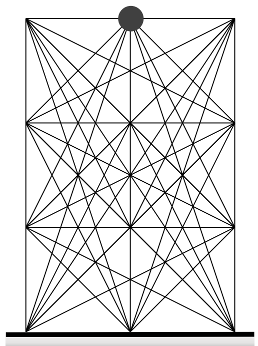	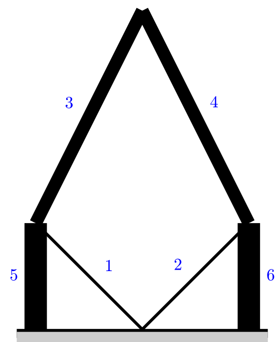	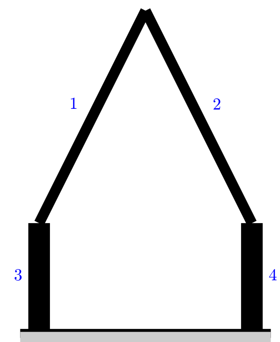
(B)	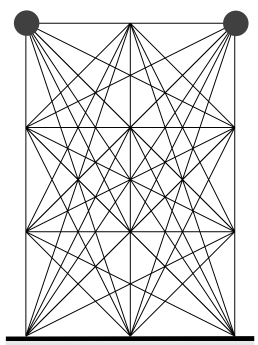	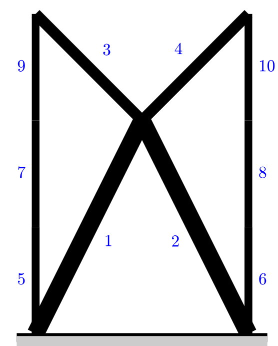	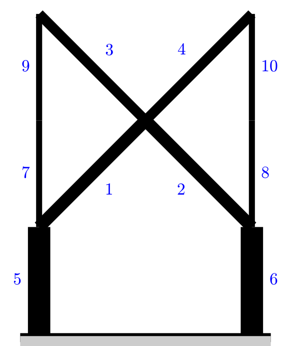

Figure 5.5: Graphical summary of the 3×2 frame structure optimized designs (application 1), including, ground structure with mass configuration and minimum volume designs (nonlinear and linear) for 2.5% system drift ratio under pulse excitation. Numerical values adjacent to structural elements denote the element number

5.4.1.3 Analysis of the results

This section provides a discussion corresponding to the results of nonlinear analysis on the optimized nonlinear and linear designs. To assess the performance of the 3×2 frame structure optimized designs, the horizontal displacement response of the concentrated mass(es) obtained from nonlinear dynamic analysis performed on each of the optimized topologies shown in Fig. 5.5 and the linear p-norm minimization, subject to the pulse excitation, are shown in Fig. 5.8. For the optimized designs of example A, it can be seen from the responses shown in Fig. 5.8, that the maximum displacement for the nonlinear design is 5.38 in., effectively satisfying the displacement constraint of $d_{limit} = 5.90$ in., whereas the maximum response of the linear design, when analyzed,

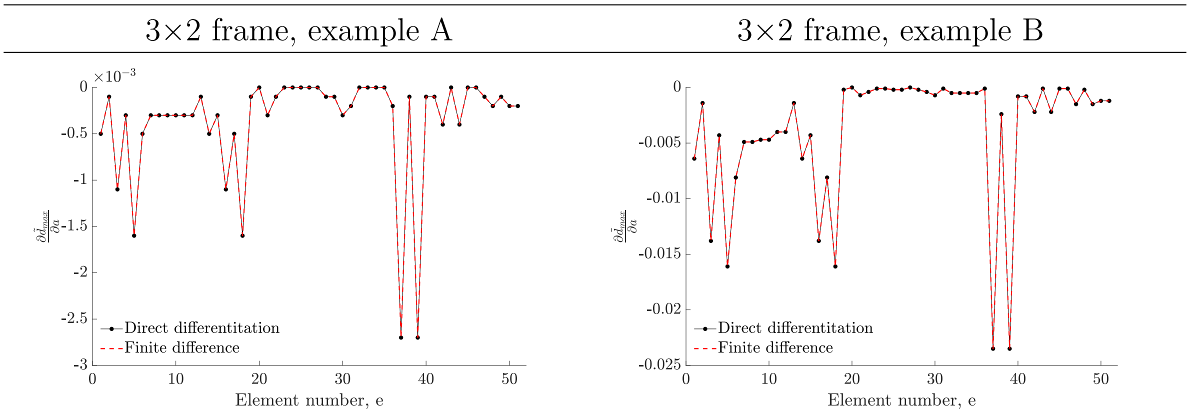

Figure 5.6: Comparison of the results of sensitivity analysis for the p-norm constraint derived with the analytical direct differentiation method and finite difference approximation for the 3×2 frame ground structure

Table 5.1: A summary of design attributes for the optimized designs of 3×2 frame structure

	Example A			**Example B**		
design	**Nonlinear**	**Linear**	**Linear, p-norm minimization**	**Nonlinear**	**Linear**	**Linear, p-norm minimization**
v_{opt} (in.^{3})	3.087×10^4	2.527×10^4	3.087×10^4	6.574×10^4	5.583×10^4	6.574×10^4
N	6	4	4	10	10	10
a_{min} (in.^{2})	10.72	37.21	47.28	41.05	32.28	38.21
a_{max} (in.^{2})	79.89	77.30	90.29	93.68	119.89	131.75

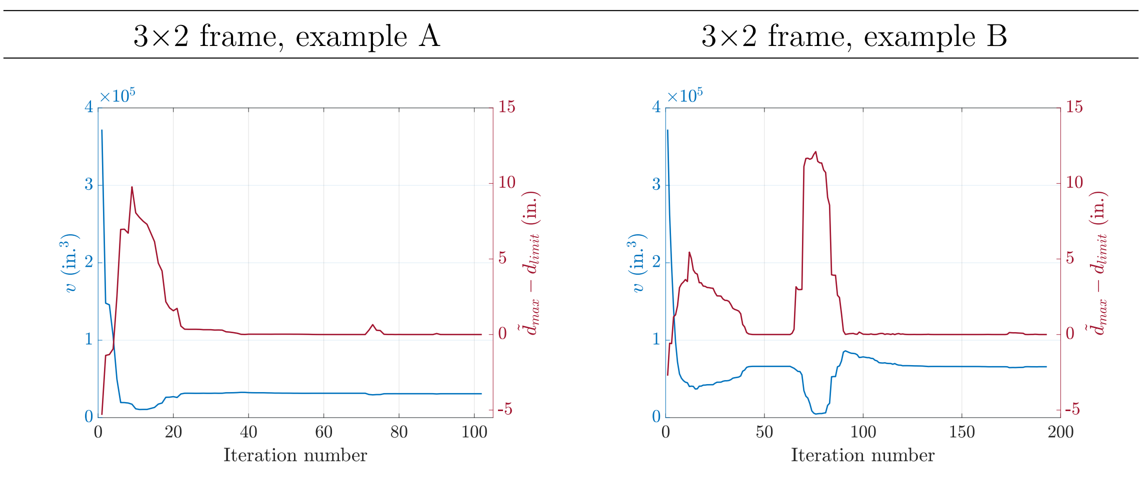

Figure 5.7: Iteration histories of the objective and constraint for the nonlinear designs of Application 1

is 7.05 in., significantly exceeding the constraint. For the optimized designs of example B, the horizontal displacement responses of the two concentrated masses are nearly identical, as such the response of one mass is shown, where the maximum displacement for the nonlinear and linear designs are 5.29 in. and 7.03 in., respectively, which is consistent to the results observed for the responses of the designs for example A. For both examples, when analyzed by nonlinear analysis, the linear designs exhibit maximum lateral displacements exceeding the maximum of the response of the nonlinear designs.

The displacement responses of concentrated mass for the linear p-norm minimization designs (examples A and B) are also shown in Fig. 5.8 to observe the performance when analyzed considering material nonlinearity. For each example, the maximum of the response for the linear p-norm design is relatively less in comparison to the response of the linear volume minimization design due to higher volume increment. However, the maximum of the response, 5.76 in. for example A and 6.35 in. for example B, exceed the maximum of the corresponding nonlinear design. Although the performance improved due to higher volume given, importantly, the volume of the nonlinear design is an unknown quantity prior to performing the nonlinear design optimization.

Along with the system level responses, element local axial force – axial strain and moment – curvature hysteretic responses with the axial-moment responses and yield function for the nonlinear and linear designs of 3×2 frame structure are presented in Chapter-5/Figures 5.9 & 5.10. Note, the axial-moment responses presented are normalized by the hysteretic capacities, P_r and M_r. For all elements analyzed, there is a combination of inelastic axial and curvature deformations simultaneously occurring and the normalized hysteretic responses remain within or on, the Orbison yield function surface. From a qualitative comparison of the elements responses, in the nonlinear designs, elements carry slightly larger axial force and smaller bending moments in comparison to the linear designs whose elements show relatively larger moments capacity.

In summary, the optimized designs and their performance illustrate the importance of considering material nonlinearity explicitly in the design problem and the effects in terms of topology, volume, and response. Furthermore, the condensation approach is shown to handle a single concentrated mass or two concentrated masses in the domain, however it is sufficiently general to handle any number of concentrated masses, though constraining many concentrated masses likely decreases the feasibility space and could make obtaining the optimized design more challenging. The p-norm was shown to effectively constrain the horizontal motion of one or multiple masses to the specified constraint value. As expected, for both examples, A and B, the solution of the nonlinear design problem resulted in a

$3{\times}2$ frame, Example A	$3{\times}2$ frame, Example B

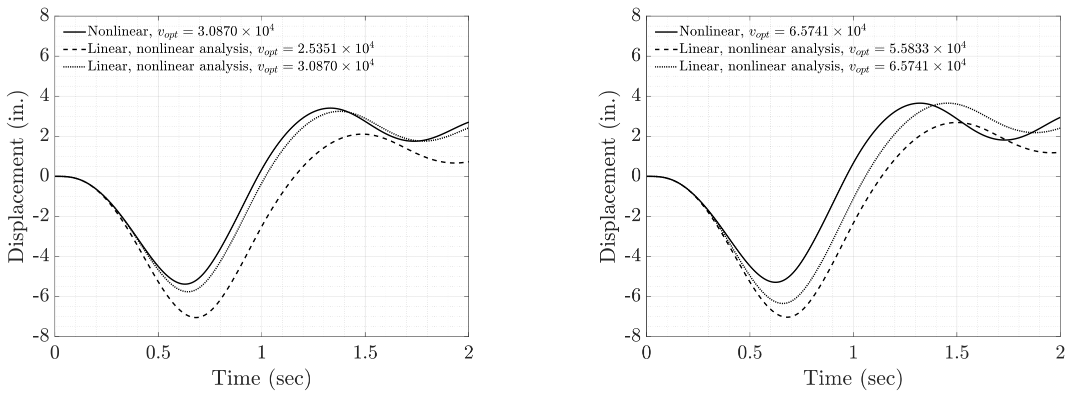

Figure 5.8: Nonlinear system displacement responses for the optimized designs of Application 1

higher volume than that of the linear design. For this application, when analyzing the linear designs by nonlinear analysis, their maximum of the response exceeded that of the nonlinear design. Although the linear and nonlinear topologies showed similar load paths, couple of differences exist between the designs, primarily, the allocation of volume to different elements.

5.4.2 Application 2: 4×2 frame structure

The second application considers the design of the lateral force resisting systems for a 4×2 frame structure subject to pulse base excitation shown in Fig. 5.4, with the amplitude set equal to $0.2g$ and period of 1 sec. For this application, the domain has dimensions of $L_x = 13.12$ ft (4 m) and $L_y = 26.25$ ft (8 m). The approximated maximum using the p-norm is constrained to d_{limit} of 7.87 in., again equivalent to a drift ratio of 2.5%. Two scenarios for the mass configuration are considered; a system consists of two concentrated masses located at the top corners of the domain (example A), and a system of four concentrated masses, where two concentrated masses are located at the top corners of the domain and two others located in the middle edges of the domain (example B). Each concentrated mass is assigned a value of 25000 lb. The presentation and discussion of the optimized designs for each example are provided in the subsequent subsections.

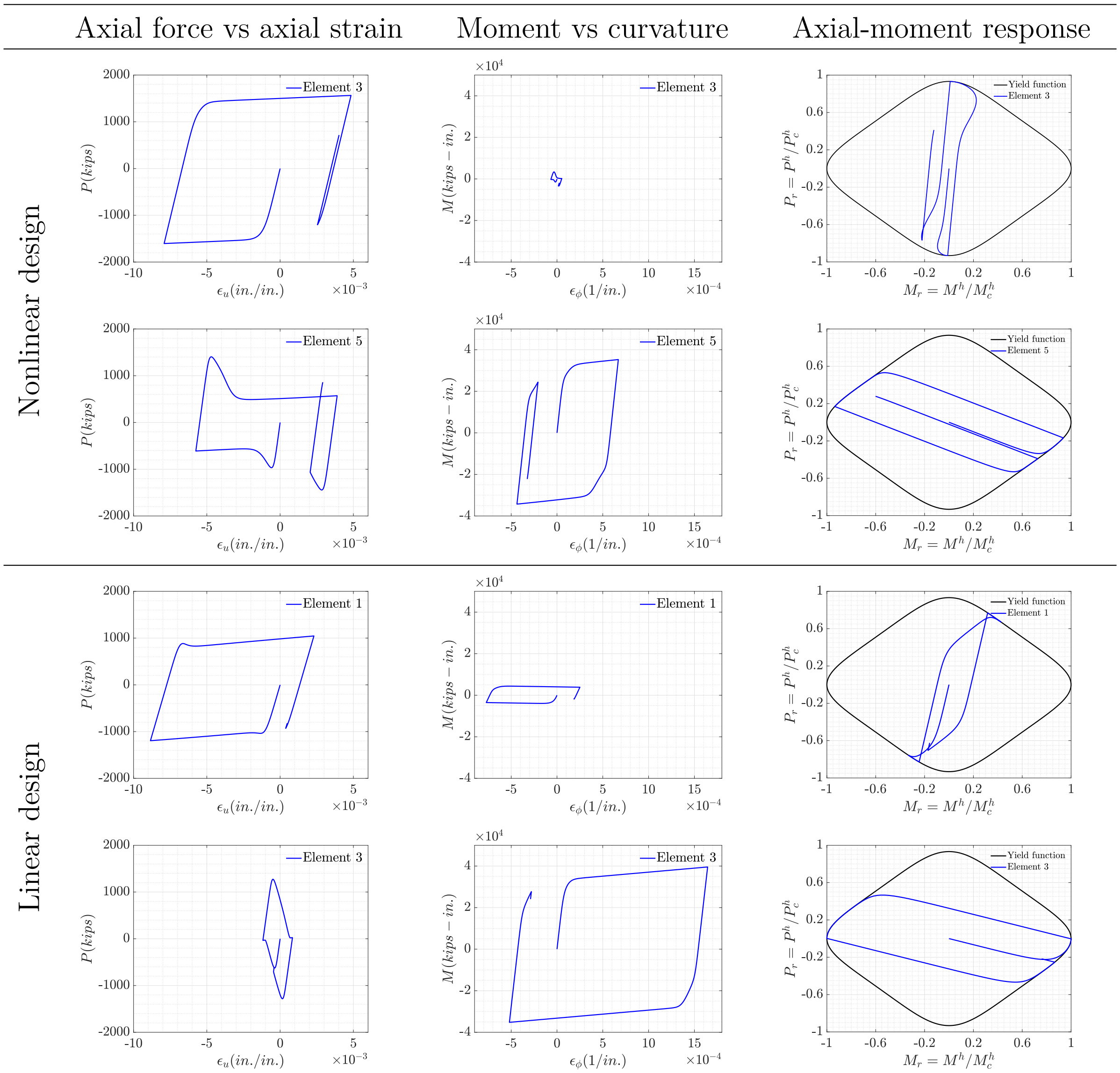

Figure 5.9: Axial force vs axial strain, and moment vs curvature diagrams of two selected elements for the nonlinear and linear designs of 3×2 frame structure for example A. Axial-moment response with the Orbison yield function also are shown on the right

5.4.2.1 Example A: two concentrated masses

For example A, two concentrated masses at the top corner nodes of the domain are considered, as shown on the ground structure in upper row of Fig. 5.11, which is a mass configuration similar to application 1, example B, but for a larger domain and design complexity. The approximated maximum of the displacements, through the p-norm, of the two corner masses is constrained to d_{limit} by combining the response of

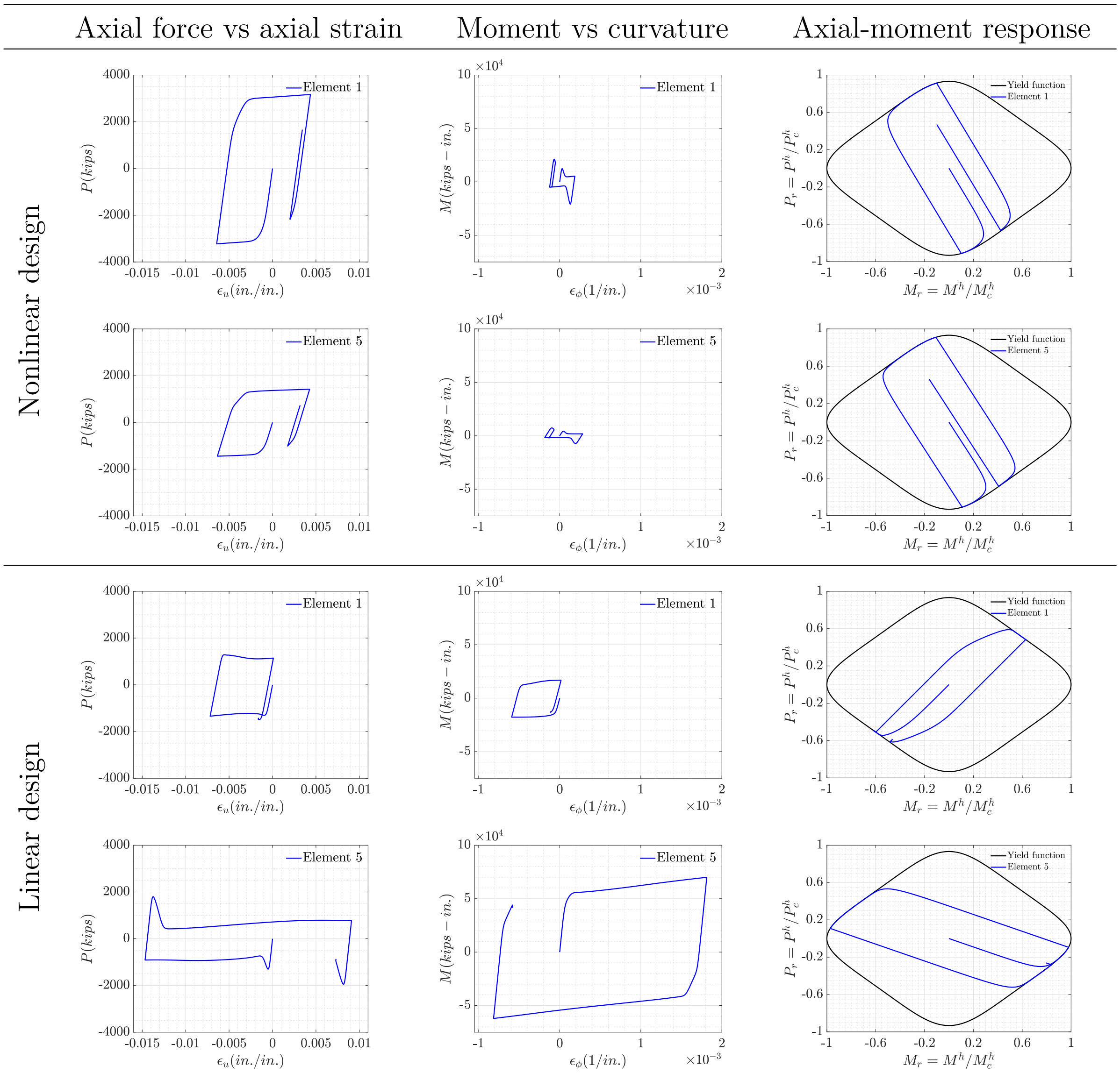

Figure 5.10: Axial force vs axial strain, and moment vs curvature diagrams of two selected elements for the nonlinear and linear designs of 3×2 frame structure for example B. Axial-moment response with the Orbison yield function also are shown on the right

each mass in the p-norm ($\lambda_1 = \lambda_2 = 1$). As with application 1, the accuracy of the analytical sensitivities are confirmed by a comparison to the values of finite different approximation, as shown in Fig. 5.12. The optimized nonlinear design is presented in the upper row of Fig. 5.11 that is comprised of 14 elements with volume of 4.965×10^4 in.^{3}, and additional design attributes are summarized in Table 5.2. The optimization history in terms of the objective and displacement constraint for each iteration throughout the optimization process for the nonlinear design is shown in Fig. 5.13. In the last iteration

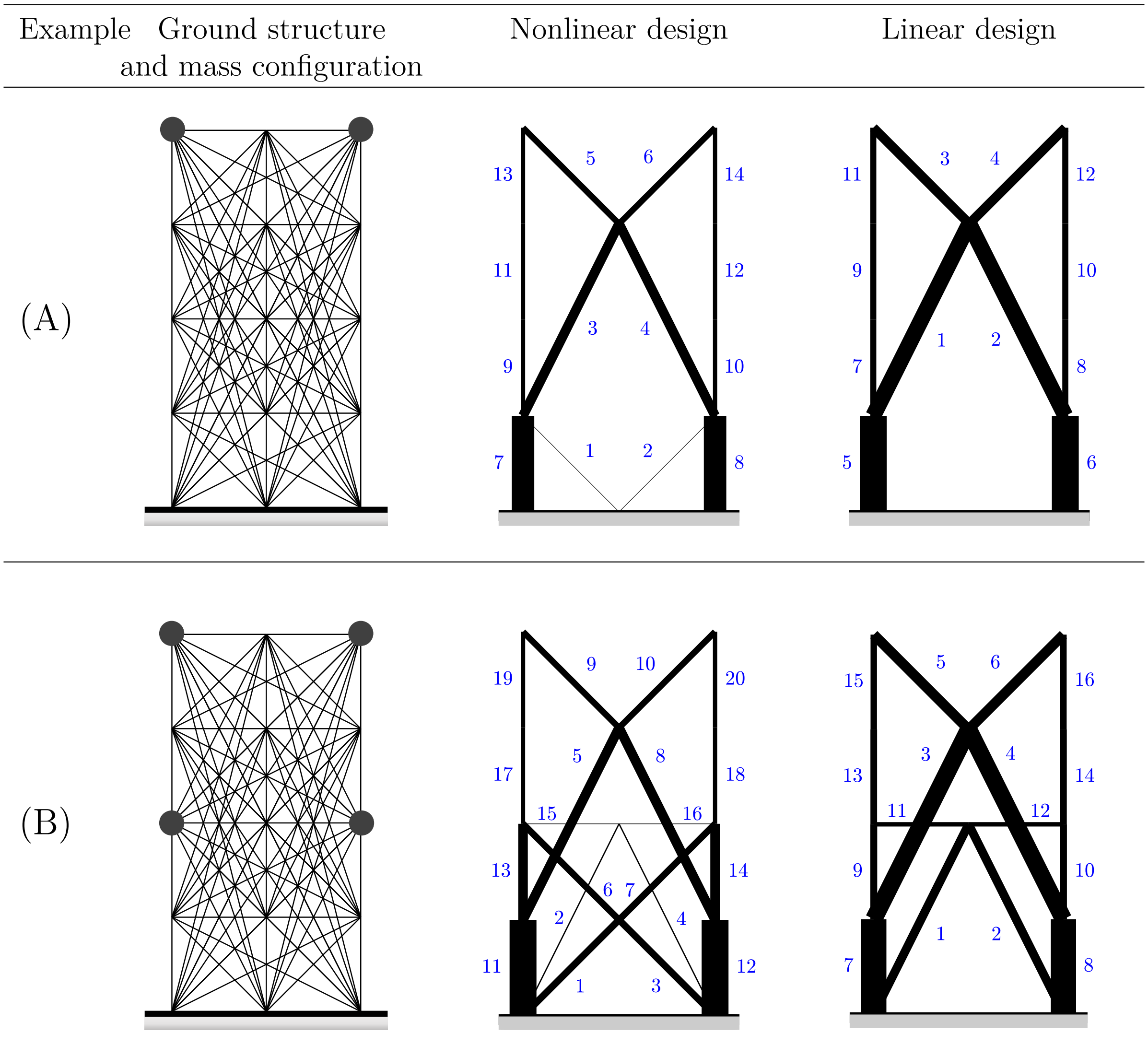

Figure 5.11: Graphical summary of the 4×2 frame structure design (application 2), including, Ground structure with mass configuration and minimum volume designs (nonlinear and linear) for 2.5% system drift ratio under pulse excitation. Numerical values adjacent to structural elements denote the element number

of optimization, the value of $\tilde{d}_{max} - d_{limit}$ is approximately zero that again shows the displacement constraint is satisfied. As with application 1, the occasional drop and rise of the objective and constraint values correspond to the beginning of each phase of optimization.

The optimized linear design is also shown in the upper row of Fig. 5.11 that is comprised of 12 elements and volume of 7.083×10^4 in.^{3}, with additional design attributes reported in Table 5.2. The overall topology of the optimized designs are similar, with

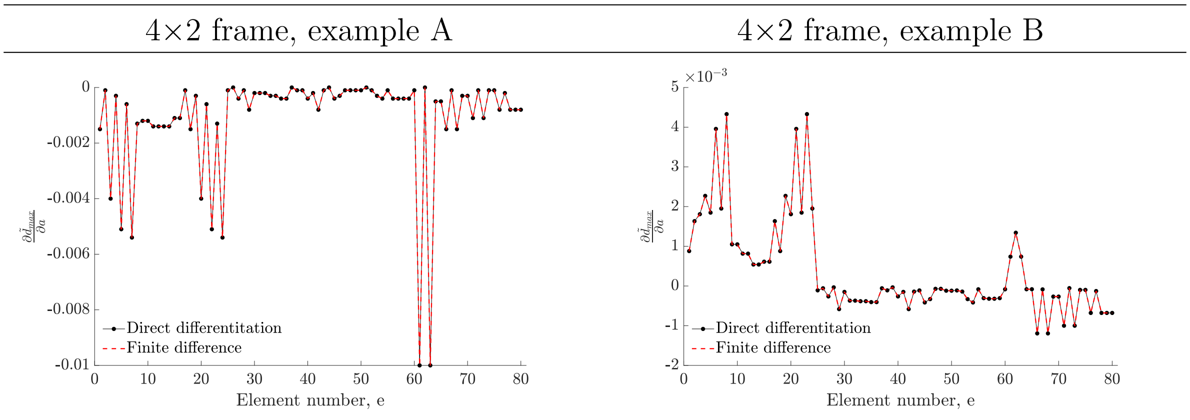

Figure 5.12: Comparison of the results of sensitivity analysis for the p-norm constraint derived with the analytical direct differentiation method and finite difference approximation for the 4×2 frame structure

the exception of the two additional bracing elements present in the nonlinear design. Interestingly, the volume of the nonlinear design is less than the linear design and this can be seen in the topologies by the relative line thickness. Similar to application 1, a linear p-norm minimization subject to volume of the nonlinear design is solved, where again the topology is the same as the linear design shown in Fig. 5.11 with exception of the cross-sectional areas being different, and design attributes reported in Table 5.2.

5.4.2.2 Example B: four concentrated masses

For example B, four concentrated masses are considered, as shown on the ground structure in Fig. 5.11. This example is intended to illustrate that the condensation approach can be effectively used for multiple concentrated masses located at different points in the domain, and that the p-norm can effectively constrain the motions of concentrated masses at different locations relative to the base. Following the approach described in Section 3.4 for constraining multiple concentrated masses placed at different heights relative to the base via a single p-norm (or constraint), the displacements of masses of the middle height are multiplied by $\lambda = 2$ (i.e., $\lambda_1 = \lambda_2 = 2$ and $\lambda_3 = \lambda_4 = 1$), and all scaled responses are combined in the p-norm. Again, and similar to previous examples, the accuracy of the analytical sensitivities are confirmed by a comparison to the values of finite different approximation, as shown in Fig. 5.12. The optimized nonlinear design is presented in the lower row of Fig. 5.11 that is comprised of 20 elements with volume of 8.824×10^4 in.^{3}, and design attributes are summarized in Table 5.2. As with previous examples, the optimization history is shown in Fig. 5.13. The value of $\tilde{d}_{max} - d_{limit}$ is approximately

4×2 frame, example A	4×2 frame, example B
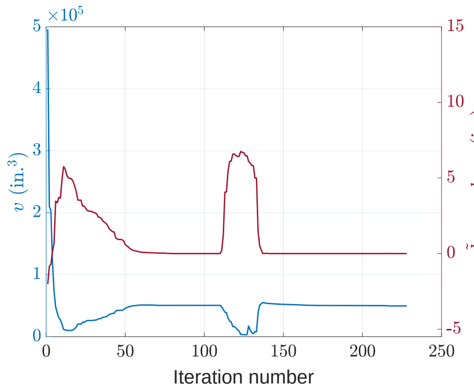	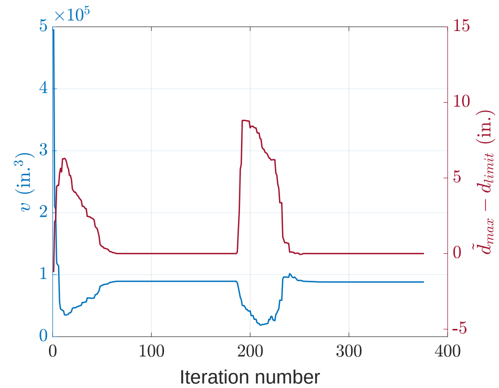

Figure 5.13: Iteration histories of the objective and constraint for the nonlinear designs of 4×2 frame structure

zero at the last iteration, that shows the displacement constraint is satisfied.

The optimized linear design is shown in the lower row of Fig. 5.11, comprised of 16 elements with volume of $11.002{\times}10^4$ in.^{3}, and additional design attributes are summarized in Table 5.2. By a comparison of the nonlinear with the linear designs, in addition to common topology connectivity, a large bracing system is present in the nonlinear topology, specifically elements 1, 3, 6 and 7, connecting the middle masses directly to the base supports providing lateral stiffness. Furthermore, elements 1, 2, 11 and 12 in the linear design, have smaller cross-sectional area size in the nonlinear design, i.e., elements 2, 4, 15 and 16. Again interestingly, and similar to example A, the nonlinear design contains lower volume relative to that of the linear design. The differences between the linear and nonlinear designs, can be attributed to the fact that for the nonlinear design proportioning of element effects both the stiffness and energy dissipation capabilities, whereas for the linear design problem, proportioning effects only the stiffness. Furthermore, for the nonlinear design problem, the axial force and bending moment capacities of the elements are explicitly considered and proportioned accordingly while respecting the yield function which tends to result in relying on diagonal elements with relatively larger axial force capacities to limit deformations. However, the linear design is obtained considering linear-elastic, essentially unlimited and independent axial and moment capacity, where the resisting axial force and bending moment are unconstrained such that flexural stiffness can be an effective means of controlling displacements. The linear optimized design obtained from the p-norm minimization is again not shown for brevity, but the design attributes are summarized in Table 5.2.

Table 5.2: A summary of design attributes for the optimized designs of 4 × 2 frame structure

	Example A			**Example B**		
design	**Nonlinear**	**Linear**	**Linear, p-norm minimization**	**Nonlinear**	**Linear**	**Linear, p-norm minimization**
v_{opt} (in.^{3})	$4.965{\times}10^4$	$7.083{\times}10^4$	$4.965{\times}10^4$	$8.824{\times}10^4$	$11.002{\times}10^4$	$8.824{\times}10^4$
N	14	12	12	20	16	16
a_{min} (in.^{2})	2.52	28.97	20.06	3.29	25.23	1.17
a_{max} (in.^{2})	107.10	128.22	100.57	153.79	144.34	137.27

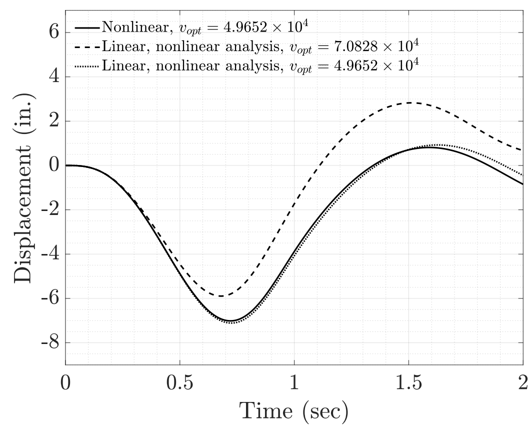

Figure 5.14: Nonlinear system displacement responses for the optimized designs of application 2, example A

Top node	Middle node
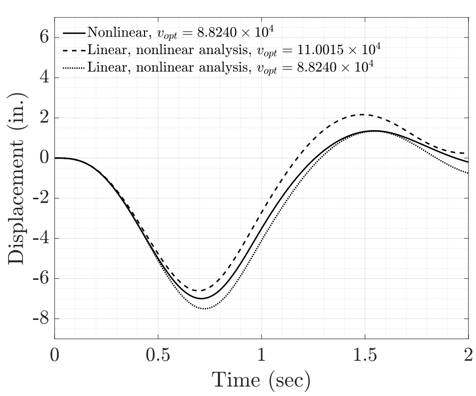	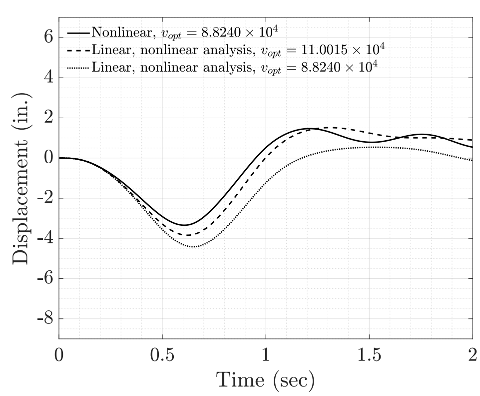

Figure 5.15: Nonlinear system displacement responses for the optimized designs of application 2, example B, for the top and middle nodes

5.4.2.3 Analysis of the results

This subsection provides results and a discussion of the nonlinear analysis performed on each of the optimized designs of application 2. The displacement responses of the concentrated masses obtained from nonlinear dynamic analysis performed on each of the 4×2 frame structure optimized designs subject to the pulse excitation, are shown in Figures 5.14 & 5.15. The results for example A are shown in Fig. 5.14, where the maximum of the response for the nonlinear design is 7.01 in. that again effectively satisfies the specified $d_{limit} = 7.87$ in. The maximum displacement response of the linear design, 5.95 in., is relatively less than the maximum of the response of the nonlinear design, owing to the fact that the linear design contains 43% more volume relative to that of the nonlinear design. The maximum of the response of the linear p-norm minimization design, 7.11 in., slightly exceeds that of the nonlinear design, even though both designs having the same amount of volume, i.e., 4.965×10^4 in.^{3}, the nonlinear design still marginally outperforms that of the linear p-norm minimization design.

For example B, the displacement responses of the top and middle concentrated masses are shown in Fig. 5.15. The maximum of the response of the nonlinear design masses at the top of the domain is 6.99 in., again effectively satisfying the specified constraint. As with example A, the linear design is comprised of a larger volume than the nonlinear design, which when evaluated by nonlinear dynamic analysis, resulted in lower maximum of the response, 6.6 in., that is slightly less than that of the nonlinear design but at the cost of higher volume. The response of the linear p-norm minimization again slightly exceeds that of the nonlinear design, 7.50 in., even though both designs contain same amount of volume, 8.8240×10^4 in.^{3}, illustrating that the nonlinear design outperforms the linear p-norm minimization response. The displacement responses of the concentrated mass located at mid height of the domain, shows that the maximum of the response for the nonlinear design is 3.5 in., less than 3.93 in., that is equivalent to 2.5% drift ratio corresponding to the height of the middle masses, and indicates that the p-norm effectively constrains displacements of concentrated masses at different levels. Interestingly, the maximum response of the mass located at mid height of the domain in the linear design is larger than that of the nonlinear design, in spite of the linear design contains 25% more volume. Last, the maximum of the response corresponding to the design of linear p-norm minimization at both locations, exceeds that of the nonlinear design, noting both designs having the same amount of volume.

Similar to application 1, element local axial force – axial strain and moment – curvature hysteretic responses for the nonlinear and linear designs of 4×2 frame structure

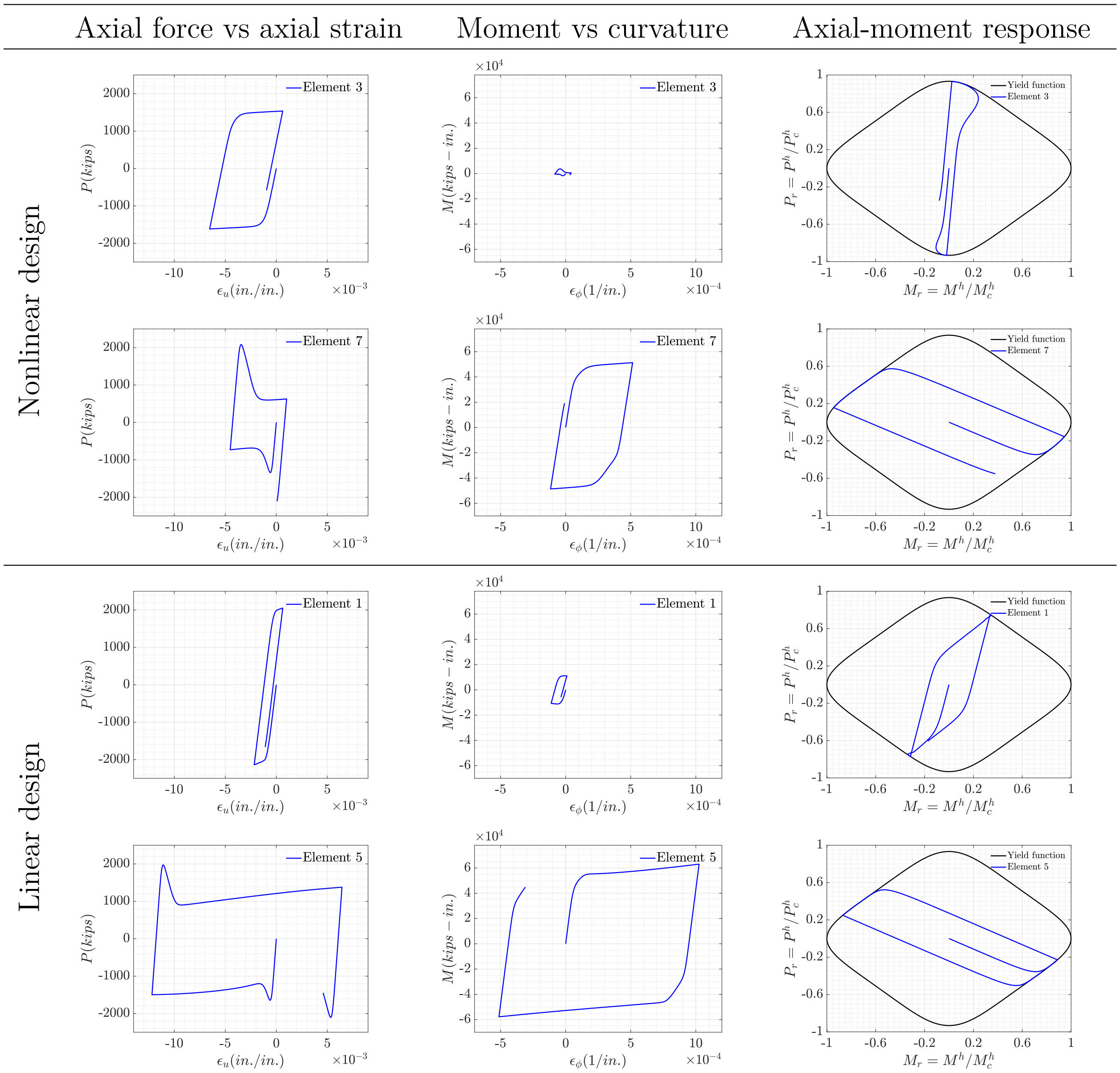

Figure 5.16: Axial force vs axial strain, and moment vs curvature diagrams of two selected elements for the nonlinear and linear designs of 4×2 frame structure for example A. Axial-moment response with the Orbison yield function also are shown on the right

for two mass configurations, by performing nonlinear dynamic analysis are presented in Figures. 5.16 and 5.17 along with the axial-moment responses and yield function for two selected elements. Similar to results of application 1, again, elements in the linear designs tend to have larger bending moments capacities relative to the elements in the nonlinear design and hence have higher moment responses, suggesting in the linear-elastic setting high flexural rigidity is an efficient and effective means of achieving the displacement limit.

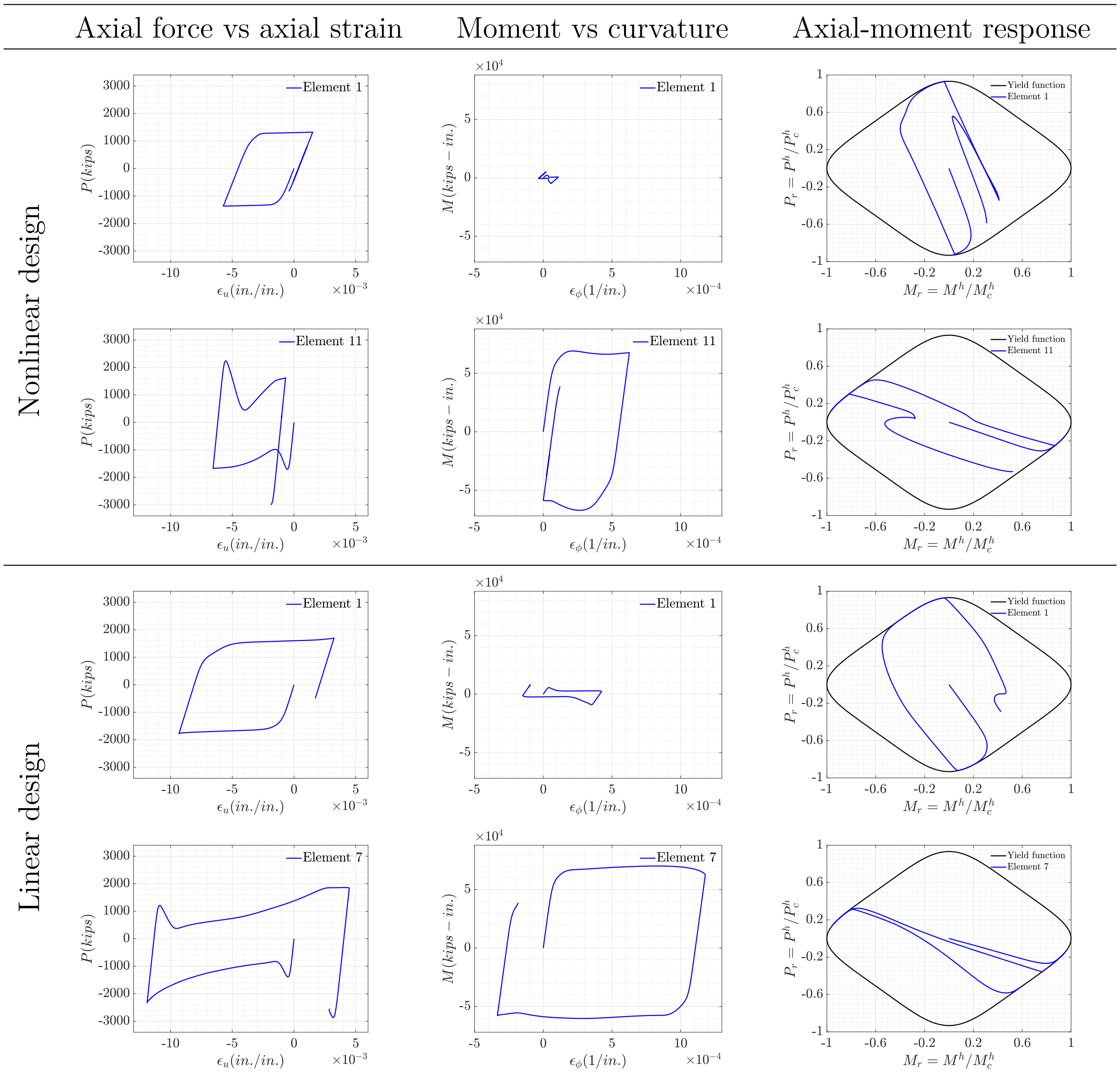

Figure 5.17: Axial force vs axial strain, and moment vs curvature diagrams of two selected elements for the nonlinear and linear designs of 4×2 frame structure for example B. Axial-moment response with the Orbison yield function also are shown on the right

In summary, the presented condensation approach is further shown to handle multiple concentrated masses, in this application at different heights relative to the base and again, the single p-norm effectively constrains the motions of concentrated masses of structural system according to the specified d_{limit}. Interestingly and in contrast to the optimized designs of 3×2 frame structure that for each example, the nonlinear design required larger volume by comparison to the linear design, for the 4×2 frame structure, the nonlinear design satisfies the specified constraint with less volume in comparison to the linear design. For both examples, the topology of the nonlinear design contains more elements relative to the corresponding linear design. A comparison of the optimized designs of application 2 show that the nonlinear design could control the maximum of the response, via combination of stiffness and energy dissipation mechanisms, resulting in less volume relative to the linear design. However, for the linear design formulation, the only way to meet the design requirements, is adding stiffness by means of volume increment. In general fewer number of elements are present in the optimized linear design to limit the maximum displacement when treated as linear-elastic.

5.5 Comparison of the designs obtained with and without condensation approach

In this section, we compare the optimized designs obtained from optimization employing condensation approach developed in this Chapter, to those obtained from the optimization method considering consistent and concentrated masses, presented in Chapter 4, in terms of design attributes and optimization demand.

We consider the 3×2 frame structure with two concentrated masses at the top corner nodes, as shown on the ground structure in Fig. 5.5, subject to pulse excitation with amplitude of $0.25g$ and period of 1 sec. The displacement constraint, d_{limit}, is set equal to 5.90 in, that is equivalent to 2.5% system drift ratio. The optimized design obtained from the two optimization formulations are presented in Fig. 5.18, where the optimized design employing condensation is repeated here for direct and clear comparison, and the optimized design considering both consistent and concentrated masses is shown on the right. Both designs share a common topology, with exception of the two additional bracing elements in the optimized design considering consistent and concentrated masses, with 18% higher amount of volume. This is due to presence of consistent masses at all nodes of the domain, that increases the total inertia forces in the structural system. The linear designs topologies obtained form with and without linear condensation approach are identical, where again the optimized design considering consistent masses, contains relatively larger volume.

With respect to the computational cost associated with each optimized design, the total number of iterations and clock time are also reported in Fig. 5.18. The optimization processes were conducted on a workstation with a Core(i7) CPU@3.20 GHz and 32 GB RAM. Optimization considering consistent and concentrated masses, requires

	Nonlinear	
	Employing condensation	Consistent and concentrated masses
	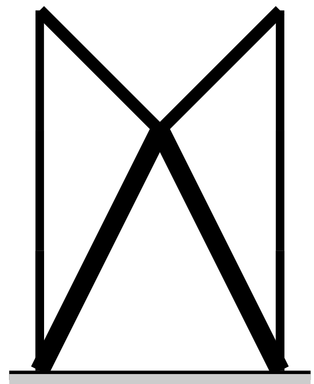	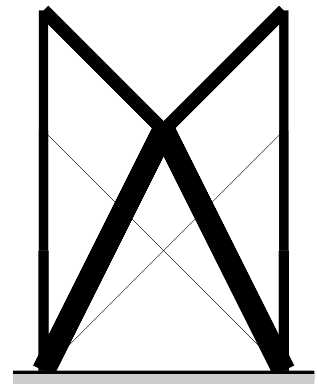
v_{opt} (in.^{3})	6.574×10^4	7.771×10^4
N	10	12
a_{min} (in.^{2})	41.05	2.2
a_{max} (in.^{2})	93.66	113.18
Total clock time	15 hrs & 55 min	18 hrs & 19 min

Figure 5.18: Comparison of the nonlinear designs obtained with and without condensation, for the 3×2 frame structure under pulse excitation for concentrated masses equal to 25 kips. A summary of design attributes and computational costs are provided below each optimized structure

approximately additional 2 hours of computational effort. A possible explanation for this observation is that, by considering consistent mass matrix, the presence of the DOF associated with the structural mass, and derivative of consistent mass matrix in the vector of gradients, complicated the optimization process, relative to the optimization employing condensation approach.

5.6 Summary and concluding remarks

In this Chapter, a method for topology optimization of nonlinear frame structures employing a condensation approach considering time-varying excitation is developed. Central to this method is a hysteretic FE beam model that accounts for material inelasticity, distributed plasticity and multiaxial interaction that because of its constant elastic stiffness matrix and hysteretic matrix facilitates a Guyan type condensation.

The condensation approach permits neglecting the consistent mass, that is the mass of the structure being designed, when the concentrated mass being supported by the structure is much larger, and hence simplifies both the nonlinear dynamic analysis in terms of reducing the DOF and the optimization process in terms of simplifying gradient expressions, relative to when consistent mass matrix is considered. The condensation approach is sufficiently general and capable of considering one or multiple concentrated masses in the domain, while in the presented design problem a single p-norm constrains the motions of the concentrated masses even if at different locations in the domain. The specific design problem considered seeks to minimize the volume of the design subject to a system-level maximum displacement constraint. The maximum of the response at node(s) with concentrated mass is approximated through the p-norm, so as to be differentiable for using gradient-based optimization. Corresponding analytical sensitivities are developed and verified by comparison to those obtained through finite difference approximation.

Several numerical examples are presented to illustrate the effects of constraining one or multiple concentrated mass(es) with different arrangements thereof and the importance of considering material nonlinearity in terms of the performance of the optimized design. These examples showed that a single p-norm effectively constrains the motion(s) of one or multiple concentrated masses in the domain according to the specified constraint.

For each nonlinear design, it has been observed that several of the elements undergo inelastic deformations at the 2.5% drift constraint. From a comparison of the nonlinear designs, to optimized designs obtained from comparable topology optimization formulations assuming linear-elastic material, the nonlinear designs are observed to outperform the linear designs with equivalent or less volume, thus illustrating the importance of explicitly considering inelasticity and multiaxial interaction in the analysis/optimization process. Furthermore, the detailed element level inelastic responses are retained when employing the condensation approach.

Chapter 6
Summary, Concluding Remarks and Future Research

6.1 Summary

This dissertation presents original methods and accompanying mathematical formulations for the topology optimization of nonlinear frame structures consist of beam elements employing a hysteretic FE model. Particularly, a new class of design methods in topology optimization are developed that provides more practical design solutions and realistic physics of the behavior of the design. As such, the nonlinear structural analysis employed in this study is based upon hysteretic FE, and the optimization problem is formulated to minimize the volume of the structural system subject to a system-level displacement constraint, as well as equilibrium and bounds on cross-sectional areas. The widely adopted ground structure approach is employed, where a dense set of connected elements in the domain serves as the starting point. Gradient-based optimization is made possible by the hysteretic FE modeling approach, and a mild mathematical approximation that together permit the derivation of analytical sensitivities. The mathematical approximation replaces the signum function in the hysteretic evolution equations with the hyperbolic tangent, that is continuous and differentiable everywhere. The accuracy of the developed sensitivities for each design method is verified with the corresponding values obtained from finite difference approximation. The suggested design methods are applied for the design of various lateral force resisting systems considering different loading, excitation and supplemental mass configurations, to demonstrate effectiveness of the proposed methods and to investigate impacts of considering nonlinearity explicitly in the design procedure. Comparative design problems considering linear-elastic material are defined and solved, to seek the optimality of the nonlinear designs, and to compare the design attributes and performance, when evaluated using nonlinear analysis.

6.2 Contributions

The primary contribution of this dissertation is a new class of methods for the design of nonlinear frame structures consist of beam elements using topology optimization. In addition to the specific contributions discussed at the end of each Chapter, here the main contributions are outlined:

1. Development of a design method for quasi-static loading, with original mathematical expressions for solution scheme and derivation of sensitivities with respect to design variables.

2. Development of a design method for dynamic base excitation, with the developed sensitivities with respect to design variables and proposing the system-level constraint employing the p-norm, to preserve analytical sensitivities and to approximate the maximum displacement response throughout the transient analysis.

3. Development of a design method and sensitivity derivations for dynamic base excitation employing a Guyan type condensation approach to reduce the dynamic DOF to those associated only with the supplemental mass while preserving detailed information at the local (element) level.

4. Effectively constraining the motions of one or multiple concentrated masses, through a single p-norm, in the domain, specifically when they are located at different heights with respect to the base.

6.3 Key findings

The key findings from the presented applications obtained from the proposed nonlinear design methods are:

1. The nonlinear design(s) satisfy the specified constraint while explicitly accounting for inelastic deformations in the system response.

2. The nonlinear and linear designs often share a similar load path, however, the nonlinear designs typically differ in the number of diagonal elements and the allocation of area to common elements.

3. In general, the nonlinear design outperforms the comparative linear designs, in terms of displacement response, when evaluated by nonlinear analysis even for the case the volumes are identical.

4. The nonlinear design can require less volume than the linear design depending on the problem specifications.

5. In the nonlinear design methods, the axial force and bending moment capacities of the elements are explicitly considered, that tends to result in relying on diagonal elements to limit deformations.

6. From the applications considered, the condensation approach was observed to decrease the computational effort in both the dynamic analysis and optimization procedure in comparison to an equivalent uncondensed, that is the design problem with consistent mass.

7. Based upon the comparisons of the results, it has been shown that the nonlinearity should be explicitly considered to obtain designs that will satisfy the performance expectations.

6.4 Future research perspectives

The focus of this dissertation was on planar frame structures composed of nonlinear Euler-Bernoulli beam elements. Based upon the findings and developments in this study, the following subjects are recommended for future research:

1. Incorporation of shear deformations into the nonlinear modeling framework to consider full interaction between axial, bending and shear, and include Timoshenko beam elements for design of frame structures using topology optimization.

2. Devising the quasi-static solution algorithm as a system of ODEs to solve the unknown displacement and hysteretic DOF more efficiently.

3. Development of a damage resistant design method by introducing damage mechanics, expressed in a tractable way for the optimization.

4. Apply an energy maximization design method to achieve topologies particularly for energy dissipation mechanisms.

5. Investigate the Hessian of Lagrangian function to seed to the optimizer (MATLAB fmincon). Initial attempts were made for the linear compliance design, and little benefits were observed. However this should be further studied at a more fundamental level for the nonlinear design methods.

6. Considering material and geometric nonlinearity simultaneously using the hysteretic FE beam model.

7. In non-convex optimization, there is a need to search for global optima using multi-start strategy. To save computational demand, however, one might consider a more rigorous strategy, for example Homotopy in optimization, that requires defining a simplified alternatives for the actual optimization problem, and then gradually adjust this solution by solving intermediate problems.

8. Investigation of damping effects for dynamic excitation on the optimized nonlinear designs via employing mass proportional, stiffness proportional and Rayleigh damping matrices.

Appendix A
Cross Sectional Areas for Randomized Starting Cases

As described in Chapter 3, a multi-start strategy is performed for design method of quasi-static loading in an attempt seeking the global optima. The specific values of areas for each randomized starting cases of 4×2 frame and 3×2 half beam ground structures for the nonlinear design problem are tabulated in Tables A.1 and A.2, respectively. The element numbering is defined in a way that the elements connected to each node are concatenated in the global element connectivity matrix. Node numbering starts from the left bottom, row-wise, of the domain and continues to the node on the top right.

Table A.1: Values of cross sectional areas (in^2) for the randomized starting cases of the 4×2 frame ground structure

Element number	Case 1	Case 2	Case 3	Case 4
1	8.0706	0.9619	3.2358	2.8014
2	4.0199	0.35266	3.2957	0.83283
3	3.1768	2.2437	3.0726	1.689
4	0.83349	1.9658	2.2373	1.5995
5	0.85705	1.4345	1.0385	0.38898
6	0.27421	2.626	0.82324	0.18225
7	8.2593	5.5058	3.8126	0.80693
8	6.3876	6.7692	1.9223	1.2549
9	3.1885	5.1734	4.295	0.65097
10	1.7917	5.3946	5.2648	2.1031
11	0.67181	0.75303	0.11323	0.082275
12	2.5162	0.54459	2.0223	0.95027
13	8.9293	6.1053	0.73508	0.58404
14	0.97425	0.52031	4.2824	1.9011
15	1.4736	2.9138	5.281	0.37995
16	1.7932	2.3252	0.28257	0.90026
17	0.29909	3.3769	3.5465	1.6023
18	2.4252	1.6676	0.060188	0.49979
19	3.6369	3.4501	5.7728	0.16879
20	5.6182	3.7236	4.1844	0.48448
21	2.299	4.1109	2.8518	0.90211
22	2.8049	2.2801	3.737	0.59814
23	0.62398	1.3635	3.394	0.36814
24	1.3519	0.51589	2.0725	1.3164
25	1.4564	5.1392	1.1638	2.4494
26	6.8521	2.2987	1.8386	3.4494
27	4.9796	0.24653	0.97245	0.99311
28	2.0052	4.1867	0.22328	2.1322
29	2.771	0.95207	0.40373	0.0093546
30	1.189	1.7349	2.3272	0.97855
31	4.796	6.0311	7.9323	2.8721
32	4.7584	1.9922	1.8924	0.52829
33	3.4155	4.0836	2.1923	2.1144
34	1.5153	1.7305	4.1548	1.3682
35	1.2095	2.68	3.5698	1.3251
36	1.6045	2.4215	2.2404	0.80644
37	3.82	3.8784	8.343	2.8416
38	2.0556	0.10857	4.0941	0.74611
39	3.1916	1.8349	1.7976	0.5067
40	3.3557	1.8603	2.7958	0.55999
41	3.8353	2.3699	2.0612	2.0957
42	3.8807	1.7279	2.4946	2.9755
43	0.71382	4.5571	3.6315	0.65863
44	0.13967	2.3843	2.8182	0.9128
45	2.6228	7.7846	3.4745	3.0907
46	1.8151	2.1694	3.2175	1.3939
47	3.7367	4.2653	4.007	2.2475
48	4.3246	1.7397	2.463	0.36516
49	8.4575	7.0896	4.6581	2.9658
50	2.6174	4.1875	3.1157	1.5325
51	2.1735	3.3093	4.3206	0.89255
52	6.9044	1.8942	0.69722	1.7058
53	6.8631	6.9308	6.0744	1.4308
54	4.2338	5.2646	5.3185	1.3592
55	9.506	4.0621	4.2326	4.0589
56	1.3539	8.3242	1.595	0.53273
57	8.7118	5.4395	4.136	4.165
58	5.9215	0.336 1	0.584	4.2646
59	2.7119	9.5344	5.4283	1.7975
60	1.2593	2.0741	4.9356	2.1806
61	0.527	0.689	2.5994	2.9014
62	2.237	2.275	1.5001	3.5534
63	2.0908	6.3792	3.6879	3.7646
64	8.5128	0.966	8.6685	3.8427
65	1.432	7.292	9.3462	1.973
66	6.6027	1.919	8.2827	2.1767
67	8.9821	2.4785	0.11702	4.849
68	1.9632	5.0466	0.067	2.9052
69	2.187	9.2845	1.011	4.3084
70	6.9137	0.238	9.2039	1.4012
71	8.6885	9.7961	0.50929	3.1554
72	0.46736	3.9499	4.5149	2.9832
73	0.343	6.6228	8.4087	4.8851
74	9.569	1.1155	8.7092	0.43555

Table A.2: Values of cross sectional areas (in^2) for the randomized starting cases of the 3×2 half beam ground structure

Element number	Case 1	Case 2	Case 3	Case 4
1	0.53091	2.0298	3.5643	1.2329
2	0.43366	1.7685	1.7167	0.1382
3	0.883	0.52707	2.2287	1.7326
4	1.2843	0.79316	0.42191	0.93694
5	1.2667	0.90156	0.84956	0.33059
6	1.063	0.085274	0.07251	0.61955
7	1.0928	1.7572	2.7203	0.62374
8	1.8322	2.2743	2.1636	2.7794
9	0.19517	0.49549	1.9484	0.8614
10	0.24238	1.8745	2.2464	2.2025
11	0.29572	2.1746	2.1128	0.040158
12	1.1641	1.4984	0.73591	1.5327
13	1.6988	1.7916	0.0012272	2.3168
14	0.65084	0.98742	1.944	1.992
15	1.074	1.6719	0.47219	1.5212
16	0.32028	0.53057	0.49845	1.6992
17	0.11928	2.1438	0.74059	0.22096
18	1.4593	1.0981	0.17242	1.6224
19	1.9231	2.1254	2.6867	0.053104
20	2.017	0.38652	1.7014	0.68823
21	1.5116	0.20232	1.235	0.42074
22	0.99969	0.45191	0.60764	1.7125
23	1.251	1.3595	1.3378	0.11274
24	1.1828	1.2653	0.77897	0.84275
25	3.3927	2.4772	3.4415	2.3559
26	0.0011334	1.6239	2.0295	1.523
27	1.3278	0.36402	0.57301	1.4297
28	2.1015	2.0397	1.9638	0.20689
29	3.3962	2.8702	1.246	3.0203
30	1.1449	0.90435	1.4157	1.2369
31	1.6451	3.4998	2.8631	2.5674
32	2.7492	0.31866	2.6807	0.78537
33	0.49437	0.7187	0.28536	1.2705
34	1.7088	1.8108	2.9557	2.5976
35	1.9546	0.13572	0.057169	2.2366
36	0.88168	1.1491	0.66612	0.73509
37	4.1006	2.7869	3.7176	0.44655
38	3.5837	2.6507	3.9716	0.29984
39	2.8431	4.156	1.8668	3.2915
40	1.1971	4.3001	3.786	4.1633
41	3.2333	3.9509	4.5352	3.6143
42	0.40504	1.5915	1.2331	1.8056
43	3.037	2.2644	0.65871	4.951
44	3.2067	3.7667	1.144	2.7201
45	3.5406	0.55012	1.779	4.9876
46	4.3217	0.54952	1.4592	0.38484
47	4.7659	1.3514	4.7142	1.0826
48	3.7311	2.627	0.26082	4.0527
49	2.821	4.8704	3.0124	4.7804
50	4.504	3.5573	0.82798	4.092
51	2.8145	1.5616	4.2614	1.5454
52	0.082397	1.4594	0.85168	0.79402
53	0.58638	4.258	2.5526	4.4338

Appendix B
Linear Design Problems for Quasi-Static Loading

In Chapter 3, two linear design problems were solved to investigate optimality of the nonlinear designs and compare the optimized topologies. The first, is a well-known traditional compliance minimization design, constrained to the optimized volume obtained from the Nonlinear design, seeking the most stiff structure for a given volume. This design problem is expressed as:

$$\begin{aligned} \text{Find}: &\quad a_1, ..., a_N \\ \underset{\mathbf{a}}{\text{Minimize}}: &\quad c = \mathbf{f}^T \mathbf{d} \\ \text{Subject to}: &\quad \mathbf{Kd} = \mathbf{f} \\ &\quad v = \sum_{s=1}^{N} a_s L_s \leq v_{opt} \\ &\quad 0 < \rho_{min} < a \leq \rho_{max}, \end{aligned} \tag{B.1}$$

where linear equilibrium equation, volume and bounds on cross sectional areas are imposed as the constraints (more information on this design problem can be found in Changizi and Jalalpour (2017a)). The second linear design problem is similar to the nonlinear design problem, where the goal is to minimize the volume of the structural system subject to the same displacement limit, stated as:

$$\begin{aligned} \text{Find}: &\quad a_1, ..., a_N \\ \underset{\mathbf{a}}{\text{Minimize}}: &\quad v = \sum_{s=1}^{N} a_s L_s \\ \text{Subject to}: &\quad \mathbf{Kd} = \mathbf{f} \\ &\quad d_v \leq d^* \\ &\quad 0 < \rho_{min} < a \leq \rho_{max}, \end{aligned} \tag{B.2}$$

where linear equilibrium equation, displacement constraint and bounds on cross sectional areas are the imposed constraints. For both linear design problems, the stiffness matrix is assembled through the element matrix shown in Eq. (2.27) by setting α_u and α_b to 1.

Appendix C
Linear Dynamic Design Problems

As mentioned in Chapter 4, the linear design problems are solved to compare with the nonlinear optimized topologies and their performance. Here, two linear design problems are presented, the first is analogous to the nonlinear design problem, where the goal is to minimize the volume of the structural system subject to the equilibrium and p-norm constraints, stated as:

$$
\begin{aligned}
\text{Find}: \quad & a_1, ..., a_N \\
\underset{\mathbf{a}}{\text{Minimize}}: \quad & v = \sum_{s=1}^{N} a_s L_s \\
\text{Subject to}: \quad & \mathbf{M}\ddot{\mathbf{d}}_i + \mathbf{K}\mathbf{d}_i = \mathbf{f}_i \\
& \tilde{d}_{max} = \left(\sum_{j=1}^{n_m} \sum_{i=1}^{n_T} d_{ji}^p \right)^{\frac{1}{p}} \leq d_{limit} \\
& 0 < \rho_{min} < a \leq \rho_{max}.
\end{aligned}
\tag{C.1}
$$

In Eq. (D.1), linear dynamic analysis is performed to establish equilibrium of the system and to evaluate the response. The p-norm constraint limits the estimated maximum displacement $\tilde{d}_{max}$ throughout the transient analysis, to a specified value of d_{limit}. Similarly, each element's cross sectional area, a, is also constrained between ρ_{min} and ρ_{max}.

Also, to investigate optimality of nonlinear designs, the second linear design problem is solved with the optimal volume obtained from the nonlinear design as a constraint, where the p-norm function is set as the objective. This design problem is defined as:

$$
\begin{aligned}
\text{Find}: \quad & a_1, ..., a_N \\
\underset{\mathbf{a}}{\text{Minimize}}: \quad & \tilde{d}_{max} = \left(\sum_{j=1}^{n_m} \sum_{i=1}^{n_T} d_{ji}^p \right)^{\frac{1}{p}} \\
\text{Subject to}: \quad & \mathbf{M}\ddot{\mathbf{d}}_i + \mathbf{K}\mathbf{d}_i = \mathbf{f}_i \\
& v = \sum_{s=1}^{N} a_s L_s \leq v_{opt} \\
& 0 < \rho_{min} < a \leq \rho_{max},
\end{aligned}
\tag{C.2}
$$

where equilibrium equation, volume and bounds on cross sectional areas are imposed as the constraints.

For both linear design problems, the mass matrix is assembled from the consistent and concentrated mass matrices, and the stiffness matrix is assembled through the element matrix shown in Eq. (2.27) by setting α_u and α_b to 1. The governing linear dynamic equations of motion are expressed in the state-space formulation, and the solution is obtained using the Runge–Kutta method.

Appendix D
Linear Dynamic Design Problems with Condensation

In Chapter 5, the linear dynamic design problems employing linear condensation method are solved to compare with the nonlinear optimized topologies and their performance. The first design problem aims to minimize the volume of the structural system subject to the equilibrium and p-norm constraints, stated as:

$$\begin{aligned}
\text{Find}: \quad & a_1, ..., a_N \\
\underset{\mathbf{a}}{\text{Minimize}}: \quad & v = \sum_{s=1}^{N} a_s L_s \\
\text{Subject to}: \quad & \hat{\mathbf{M}}\ddot{\mathbf{d}}_m + \hat{\mathbf{K}}\mathbf{d}_m = \mathbf{f}_m \\
& \tilde{d}_{max} = \left(\sum_{j=1}^{n_m} \sum_{i=1}^{n_T} (\lambda_j d_{ji})^p \right)^{\frac{1}{p}} \leq d_{limit} \\
& 0 < \rho_{min} < a \leq \rho_{max}.
\end{aligned} \tag{D.1}$$

In Equation (D.1), linear dynamic analysis is performed to establish equilibrium of the system and to evaluate the response. The p-norm constraint limits the estimated maximum displacement $\tilde{d}_{max}$ throughout the transient analysis, to a specified value of d_{limit}. Similarly, each element's cross-sectional area, a, is also constrained between ρ_{min} and ρ_{max}.

Furthermore, to test optimality of nonlinear designs, the second linear design problem is solved with the optimized volume obtained from the nonlinear design as a constraint, where the p-norms is set as the objective. This design problem is defined as:

$$\begin{aligned}
\text{Find}: \quad & a_1, ..., a_N \\
\underset{\mathbf{a}}{\text{Minimize}}: \quad & \tilde{d}_{max} = \left(\sum_{j=1}^{n_m} \sum_{i=1}^{n_T} (\lambda_j d_{ji})^p \right)^{\frac{1}{p}} \leq d_{limit} \\
\text{Subject to}: \quad & \hat{\mathbf{M}}\ddot{\mathbf{d}}_m + \hat{\mathbf{K}}\mathbf{d}_m = \mathbf{f}_m \\
& v = \sum_{s=1}^{N} a_s L_s \leq v_{opt} \\
& 0 < \rho_{min} < a \leq \rho_{max},
\end{aligned} \tag{D.2}$$

where equilibrium, volume and bounds on cross-sectional areas are imposed as the constraints.

For both linear design problems, $\hat{\mathbf{M}}$ stands for the diagonal concentrated mass matrix and the stiffness matrix is assembled through the element level expression shown in Equation (2.27) by setting α_u and α_b to 1. The solution is obtained using the Runge–Kutta method where the hysteretic terms are omitted in state-space formulation.

Bibliography

Alberdi, R., Zhang, G., Li, L., Khandelwal, K., 2018. A unified framework for nonlinear path-dependent sensitivity analysis in topology optimization. International Journal for Numerical Methods in Engineering .

Allahdadian, S., Boroomand, B., 2016. Topology optimization of planar frames under seismic loads induced by actual and artificial earthquake records. Engineering Structures 115, 140–154.

Allahdadian, S., Boroomand, B., Barekatein, A., 2012. Towards optimal design of bracing system of multi-story structures under harmonic base excitation through a topology optimization scheme. Finite Elements in Analysis and Design 61, 60–74.

American Institute of Steel Construction, 2015. Steel Construction Manual Shapes Database. URL: http://www.aisc.org/content.aspx?id=2868.

Andreassen, E., Clausen, A., Schevenels, M., Lazarov, B.S., Sigmund, O., 2011. Efficient topology optimization in matlab using 88 lines of code. Structural and Multidisciplinary Optimization 43, 1–16.

Angeli, D., Ferrell, J.E., Sontag, E.D., 2004. Detection of multistability, bifurcations, and hysteresis in a large class of biological positive-feedback systems. Proceedings of the National Academy of Sciences 101, 1822–1827.

Asadpoure, A., Tootkaboni, M., Guest, J.K., 2011. Robust topology optimization of structures with uncertainties in stiffness–application to truss structures. Computers & Structures 89, 1131–1141.

ASCE, 2017. Minimum Design Loads for Buildings and Other Structures. Asce/-sei 7-16 ed., American Society of Civil Engineers, Reston, VA. URL: https://ascelibrary.org/doi/abs/10.1061/9780784414248, doi:10.1061/9780784414248, arXiv:https://ascelibrary.org/doi/pdf/10.1061/9780784414248.

Aydin, E., Boduroglu, M., Guney, D., 2007. Optimal damper distribution for seismic rehabilitation of planar building structures. Engineering Structures 29, 176–185.

Baber, T.T., Noori, M.N., 1985. Random vibration of degrading, pinching systems. Journal of Engineering Mechanics 111, 1010–1026.

Baber, T.T., Wen, Y.K., 1981. Random vibration hysteretic, degrading systems. Journal of the Engineering Mechanics Division 107, 1069–1087.

Bathe, K.J., 2006. Finite element procedures. Klaus-Jurgen Bathe.

Behrou, R., Guest, J.K., 2017. Topology optimization for transient response of structures subjected to dynamic loads, in: 18th AIAA/ISSMO multidisciplinary analysis and optimization conference, p. 3657.

Bendsøe, M.P., Díaz, A.R., 1994. Optimization of material properties for improved frequency response. Structural optimization 7, 138–140.

Bendsoe, M.P., Kikuchi, N., 1988. Generating optimal topologies in structural design using a homogenization method. Computer Methods in Applied Mechanics and Engineering .

Bendsoe, M.P., Sigmund, O., 2004. Topology optimization: theory, methods and applications. Springer.

Boese, K.D., Kahng, A.B., Muddu, S., 1994. A new adaptive multi-start technique for combinatorial global optimizations. Operations Research Letters 16, 101–114.

Bouc, R., 1967. Forced vibration of mechanical systems with hysteresis in proceedings of the fourth conference on non-linear oscillation. Prague, Czechoslovakia , 315.

Bowman, B., Sans, W., 1985. Partitioning behavior of insecticides in soil-water systems: Ii. desorption hysteresis effects 1. Journal of environmental Quality 14, 270–273.

Brake, M., Segalman, D., 2010. Nonlinear model reduction of von karman plates under quasi-steady fluid flow. AIAA journal 48, 2339–2347.

Brake, M., Segalman, D., 2013. Modelling localized nonlinearities in continuous systems via the method of augmentation by non-smooth basis functions. Proceedings of the Royal Society A: Mathematical, Physical and Engineering Sciences 469, 20130260.

Buhl, T., Pedersen, C.B., Sigmund, O., 2000. Stiffness design of geometrically nonlinear structures using topology optimization. Structural and Multidisciplinary Optimization 19, 93–104.

Casciati, F., 1989. Stochastic dynamics of hysteretic media. Structural safety 6, 259–269.

Cavazzuti, M., Baldini, A., Bertocchi, E., Costi, D., Torricelli, E., Moruzzi, P., 2011. High performance automotive chassis design: a topology optimization based approach. Structural and Multidisciplinary Optimization 44, 45–56.

Changizi, N., Jalalpour, M., 2017a. Robust topology optimization of frame structures under geometric or material properties uncertainties. Structural and Multidisciplinary Optimization 56, 791–807.

Changizi, N., Jalalpour, M., 2017b. Stress-based topology optimization of steel-frame structures using members with standard cross sections: Gradient-based approach. Journal of Structural Engineering 143, 04017078.

Changizi, N., Jalalpour, M., 2018. Topology optimization of steel frame structures with constraints on overall and individual member instabilities. Finite Elements in Analysis and Design 141, 119–134.

Changizi, N., Kaboodanian, H., Jalalpour, M., 2017. Stress-based topology optimization of frame structures under geometric uncertainty. Computer Methods in Applied Mechanics and Engineering 315, 121–140.

Choi, S., Lee, H., Chang, E., 2001. Field test results of a semi-active er suspension system associated with skyhook controller. Mechatronics 11, 345–353.

Chung, J., Hulbert, G., 1993. A time integration algorithm for structural dynamics with improved numerical dissipation: the generalized-α method. Journal of Applied Mechanics, Transactions ASME .

Constantinou, M., Mokha, A., Reinhorn, A., 1990. Teflon bearings in base isolation ii: Modeling. Journal of Structural Engineering 116, 455–474.

Deaton, J.D., Grandhi, R.V., 2014. A survey of structural and multidisciplinary continuum topology optimization: post 2000. Structural and Multidisciplinary Optimization 49, 1–38.

Díaaz, A.R., Kikuchi, N., 1992. Solutions to shape and topology eigenvalue optimization problems using a homogenization method. International Journal for Numerical Methods in Engineering 35, 1487–1502.

Dorn, W., 1964. Automatic design of optimal structures. J. de Mecanique 3, 25–52.

Dunning, P.D., Kim, H.A., Mullineux, G., 2011. Introducing loading uncertainty in topology optimization. AIAA journal 49, 760–768.

Duysinx, P., Bendsøe, M.P., 1998. Topology optimization of continuum structures with local stress constraints. International journal for numerical methods in engineering 43, 1453–1478.

Duysinx, P., Sigmund, O., 1998. New developments in handling stress constraints in optimal material distribution, in: 7th AIAA/USAF/NASA/ISSMO symposium on multidisciplinary analysis and optimization, p. 4906.

Erlicher, S., Point, N., 2004. Thermodynamic admissibility of bouc–wen type hysteresis models. Comptes rendus mecanique 332, 51–57.

Foliente, G.C., 1995. Hysteresis modeling of wood joints and structural systems. Journal of Structural Engineering 121, 1013–1022.

Gomes, F.A., Senne, T.A., 2014. An algorithm for the topology optimization of geometrically nonlinear structures. International Journal for Numerical Methods in Engineering 99, 391–409.

Gomez, F., Spencer, B.F., 2019. Topology optimization framework for structures subjected to stationary stochastic dynamic loads. Structural and Multidisciplinary Optimization 59, 813–833.

Gömöry, F., Vojenčiak, M., Pardo, E., Šouc, J., 2009. Magnetic flux penetration and ac loss in a composite superconducting wire with ferromagnetic parts. Superconductor Science and Technology 22, 034017.

Guest, J., Igusa, T., 2008. Structural optimization under uncertain loads and nodal locations. Comput. Meth. Appl. Mech. Eng. 198, 116–124.

Guest, J.K., Prévost, J.H., 2006. Topology optimization of creeping fluid flows using a darcy–stokes finite element. International Journal for Numerical Methods in Engineering 66, 461–484.

Guyan, R.J., 1965. Reduction of stiffness and mass matrices. AIAA journal 3, 380–380.

Holmberg, E., Torstenfelt, B., Klarbring, A., 2013. Stress constrained topology optimization. Structural and Multidisciplinary Optimization 48, 33–47.

Hughes, T.J., Liu, W., 1978. Implicit-explicit finite elements in transient analysis: Implementation and numerical examples. Journal of Applied Mechanics, Transactions ASME 45, 375–378.

Jalalpour, M., Guest, J.K., Igusa, T., 2013. Reliability-based topology optimization of trusses with stochastic stiffness. Structural Safety 43, 41–49.

James, K.A., Waisman, H., 2014. Failure mitigation in optimal topology design using a coupled nonlinear continuum damage model. Computer Methods in Applied Mechanics and Engineering 268, 614–631.

James, K.A., Waisman, H., 2015. Topology optimization of structures under variable loading using a damage superposition approach. International Journal for Numerical Methods in Engineering 101, 375–406.

Jansen, M., Lombaert, G., Diehl, M., Lazarov, B.S., Sigmund, O., Schevenels, M., 2013. Robust topology optimization accounting for misplacement of material. Structural and Multidisciplinary Optimization 47, 317–333.

Kim, T., Rook, T., Singh, R., 2003. Effect of smoothening functions on the frequency response of an oscillator with clearance non-linearity. Journal of Sound and Vibration 263, 665–678.

Klarbring, A., Strömberg, N., 2013. Topology optimization of hyperelastic bodies including non-zero prescribed displacements. Structural and Multidisciplinary Optimization 47, 37–48.

Kleiber, M., 1993. Shape and non-shape structural sensitivity analysis for problems with any material and kinematic non-linearity. Computer Methods in Applied Mechanics and Engineering 108, 73–97.

Kogiso, N., Ahn, W., Nishiwaki, S., Izui, K., Yoshimura, M., 2008. Robust topology optimization for compliant mechanisms considering uncertainty of applied loads. Journal of Advanced Mechanical Design, Systems, and Manufacturing 2, 96–107.

Lavan, O., Levy, R., 2005. Optimal design of supplemental viscous dampers for irregular shear-frames in the presence of yielding. Earthquake engineering & structural dynamics 34, 889–907.

Le, C., Norato, J., Bruns, T., Ha, C., Tortorelli, D., 2010. Stress-based topology optimization for continua. Structural and Multidisciplinary Optimization 41, 605–620.

Levy, R., Lavan, O., 2006. Fully stressed design of passive controllers in framed structures for seismic loadings. Structural and Multidisciplinary Optimization 32, 485–498.

Li, L., Zhang, G., Khandelwal, K., 2017. Topology optimization of energy absorbing structures with maximum damage constraint. International Journal for Numerical Methods in Engineering 112, 737–775.

Li, L., Zhang, G., Khandelwal, K., 2018. Failure resistant topology optimization of structures using nonlocal elastoplastic-damage model. Structural and Multidisciplinary Optimization , 1–30.

Liu, H., Zhang, W., Gao, T., 2015. A comparative study of dynamic analysis methods for structural topology optimization under harmonic force excitations. Structural and Multidisciplinary Optimization 51, 1321–1333.

Luo, Y., Wang, M.Y., Kang, Z., 2015. Topology optimization of geometrically nonlinear structures based on an additive hyperelasticity technique. Computer methods in applied mechanics and engineering 286, 422–441.

Ma, Z.D., Cheng, H.C., Kikuchi, N., 1994. Structural design for obtaining desired eigenfrequencies by using the topology and shape optimization method. Computing Systems in Engineering 5, 77–89.

Ma, Z.D., Kikuchi, N., Hagiwara, I., 1993. Structural topology and shape optimization for a frequency response problem. Computational mechanics 13, 157–174.

Martí, R., Lozano, J.A., Mendiburu, A., Hernando, L., 2016. Multi-start methods. Handbook of Heuristics , 1–21.

Maute, K., Schwarz, S., Ramm, E., 1998. Adaptive topology optimization of elastoplastic structures. Structural Optimization 15, 81–91.

McLean, L., Hahn, E., 1983. Unbalance behavior of squeeze film damped multi-mass flexible rotor bearing systems. Journal of Tribology, ASME .

Miche, U., 1904. The limits of economy of material in frame structure. Philosophical Magazine 8, 589–597.

Min, S., Kikuchi, N., Park, Y., Kim, S., Chang, S., 1999. Optimal topology design of structures under dynamic loads. Structural optimization 17, 208–218.

Nakshatrala, P., Tortorelli, D., 2015. Topology optimization for effective energy propagation in rate-independent elastoplastic material systems. Computer Methods in Applied Mechanics and Engineering 295, 305–326.

Nakshatrala, P.B., Tortorelli, D., Nakshatrala, K., 2013. Nonlinear structural design using multiscale topology optimization. part i: Static formulation. Computer Methods in Applied Mechanics and Engineering 261, 167–176.

Newmark, N.M., 1959. A method of computation for structural dynamics. Journal of the engineering mechanics division 85, 67–94.

Orbison, J.G., McGuire, W., Abel, J.F., 1982. Yield surface applications in nonlinear steel frame analysis. Computer Methods in Applied Mechanics and Engineering 33, 557–573.

Ozbulut, O.E., Hurlebaus, S., 2011. Optimal design of superelastic-friction base isolators for seismic protection of highway bridges against near-field earthquakes. Earthquake Engineering & Structural Dynamics 40, 273–291.

París, J., Navarrina, F., Colominas, I., Casteleiro, M., 2010. Block aggregation of stress constraints in topology optimization of structures. Advances in Engineering Software 41, 433–441.

Patel, N.M., Kang, B.S., Renaud, J.E., Tovar, A., 2009. Crashworthiness design using topology optimization. Journal of Mechanical Design 131.

Pedersen, C.B., 2003. Topology optimization design of crushed 2d-frames for desired energy absorption history. Structural and Multidisciplinary Optimization 25, 368–382.

Pedersen, C.B., 2004. Crashworthiness design of transient frame structures using topology optimization. Computer methods in applied mechanics and engineering 193, 653–678.

Pedersen, N.L., 2000. Maximization of eigenvalues using topology optimization. Structural and multidisciplinary optimization 20, 2–11.

Ramos, A.S., Paulino, G.H., 2015. Convex topology optimization for hyperelastic trusses based on the ground-structure approach. Structural and Multidisciplinary Optimization 51, 287–304.

Rouch, K., Kao, J., 1980. Dynamic reduction in rotor dynamics by the finite element method. Journal of Mechanical Design, ASME .

Sawicki, J.T., Gawronski, W., 1997. Balanced model reduction and control of rotor-bearing systems. Journal of Engineering for Gas Turbines and Power, ASME .

Schwarz, S., Maute, K., Ramm, E., 2001. Topology and shape optimization for elasto-plastic structural response. Computer Methods in Applied Mechanics and Engineering 190, 2135–2155.

Segalman, D.J., 2007. Model reduction of systems with localized nonlinearities. Journal of Computational and Nonlinear Dynamics .

Shobeiri, V., 2019. Bi-directional evolutionary structural optimization for nonlinear structures under dynamic loads. International Journal for Numerical Methods in Engineering .

Sigmund, O., 1994. Design of material structures using topology optimization. Ph.D. thesis. Technical University of Denmark Denmark.

Sigmund, O., 1997. On the design of compliant mechanisms using topology optimization. Journal of Structural Mechanics 25, 493–524.

Sigmund, O., 2001. A 99 line topology optimization code written in matlab. Structural and multidisciplinary optimization 21, 120–127.

Sigmund, O., 2007. Morphology-based black and white filters for topology optimization. Struct. Multi. Optim. 33, 401–424. doi:10.1007/s00158-006-0087-x.

Sigmund, O., 2011. On the usefulness of non-gradient approaches in topology optimization. Structural and Multidisciplinary Optimization 43, 589–596.

Sigmund, O., Maute, K., 2013. Topology optimization approaches. Structural and Multidisciplinary Optimization 48, 1031–1055.

Sivaselvan, M.V., Reinhorn, A.M., 2000. Hysteretic models for deteriorating inelastic structures. Journal of Engineering Mechanics 126, 633–640.

Song, J., Ellingwood, B.R., 1999. Seismic reliability of special moment steel frames with welded connections: Ii. Journal of Structural Engineering 125, 372–384.

Tcherniak, D., 2002. Topology optimization of resonating structures using simp method. International Journal for Numerical Methods in Engineering 54, 1605–1622.

The MathWorks Inc., 2018. MATLAB- Optimization toolbox, Version 8.1. The MathWorks Inc., Natick, Massachusetts. URL: http://www.mathworks.com/products/optimization/.

Tootkaboni, M., Asadpoure, A., Guest, J.K., 2012. Topology optimization of continuum structures under uncertainty–a polynomial chaos approach. Computer Methods in Applied Mechanics and Engineering 201, 263–275.

Tortorelli, D.A., 1992. Sensitivity analysis for non-linear constrained elastostatic systems. International journal for numerical methods in engineering 33, 1643–1660.

Triantafyllou, S., Koumousis, V., 2012a. Bouc-wen type hysteretic plane stress element. Journal of Engineering Mechanics 138, 235–246.

Triantafyllou, S., Koumousis, V., 2012b. Small and large displacement dynamic analysis of frame structures based on hysteretic beam elements. Journal of Engineering Mechanics 138, 36–49.

Triantafyllou, S., Koumousis, V., 2014. Hysteretic finite elements for the nonlinear static and dynamic analysis of structures. Journal of Engineering Mechanics 140, 04014025.

Triantafyllou, S.P., Koumousis, V.K., 2008. A rod element formulation for the nonlinear dynamic analysis of trusses, in: 6th National Conference on Steel Strucures, Iwannina, Greece, pp. 2–4.

Triantafyllou, S.P., Koumousis, V.K., 2011. An inelastic timoshenko beam element with axial–shear–flexural interaction. Computational Mechanics 48, 713–727.

Tsay, J., Arora, J., 1990. Nonlinear structural design sensivitity analysis for path dependent problems. part 1: General theory. Computer Methods in Applied Mechanics and Engineering 81, 183–208.

Unger, E., Hoke, E., Bailie, C., Nguyen, W., Bowring, A., Heumüller, T., Christoforo, M., McGehee, M., 2014. Hysteresis and transient behavior in current–voltage measurements of hybrid-perovskite absorber solar cells. Energy & Environmental Science 7, 3690–3698.

Vázquez, M., Sinnecker, J., Kurlyandskaya, G., 1999. Hysteretic behavior and anisotropy fields in the magneto-impedance effect, in: Materials Science Forum, Trans Tech Publ. pp. 209–218.

Wallin, M., Jönsson, V., Wingren, E., 2016. Topology optimization based on finite strain plasticity. Structural and multidisciplinary optimization 54, 783–793.

Wen, Y.K., 1976. Method for random vibration of hysteretic systems. Journal of the engineering mechanics division 102, 249–263.

Yoon, G.H., Kim, Y.Y., 2005. Element connectivity parameterization for topology optimization of geometrically nonlinear structures. International journal of solids and structures 42, 1983–2009.

Yuge, K., Kikuchi, N., 1995. Optimization of a frame structure subjected to a plastic deformation. Structural optimization 10, 197–208.

Zhang, G., Li, L., Khandelwal, K., 2017a. Topology optimization of structures with anisotropic plastic materials using enhanced assumed strain elements. Structural and Multidisciplinary Optimization 55, 1965–1988.

Zhang, X., Ramos, A.S., Paulino, G.H., 2017b. Material nonlinear topology optimization using the ground structure method with a discrete filtering scheme. Structural and Multidisciplinary Optimization 55, 2045–2072.

Zhang, X.S., Paulino, G.H., Ramos, A.S., 2018. Multi-material topology optimization with multiple volume constraints: a general approach applied to ground structures with material nonlinearity. Structural and Multidisciplinary Optimization 57, 161–182.

Zhao, J., Yoon, H., Youn, B.D., 2019. An efficient concurrent topology optimization approach for frequency response problems. Computer Methods in Applied Mechanics and Engineering 347, 700–734.

Zhao, X., Wu, B., Li, Z., Zhong, H., 2018. A method for topology optimization of structures under harmonic excitations. Structural and Multidisciplinary Optimization 58, 475–487.

Zhu, J.H., He, F., Liu, T., Zhang, W.H., Liu, Q., Yang, C., 2018. Structural topology optimization under harmonic base acceleration excitations. Structural and Multidisciplinary Optimization 57, 1061–1078.

Vita

Navid Changizi

Education

- **Ph.D.**, Civil and Environmental Engineering
  Pennsylvania State University
- **M.S.**, Civil Engineering
  Cleveland State University
- **B.S.**, Engineering Science, Computational Engineering
  University of Tehran

Journal Articles

1. **Changizi, N.** and Warn, G. P., 2020. Topology optimization of structural frames considering material nonlinearity and time-varying excitation. Accepted for publication in *Structural and Multidisciplinary Optimization*.
2. **Changizi, N.** and Warn, G. P., 2020. Stochastic stress-based topology optimization of structural frames based upon the second deviatoric stress invariant. *Engineering Structures*, 224, p.111186.
3. **Changizi, N.** and Warn, G. P., 2020. Topology optimization of structural systems based on a nonlinear beam finite element model. *Structural and Multidisciplinary Optimization*, pp.1-21.
4. **Changizi, N.** and Jalalpour, M., 2018. Topology optimization of steel frame structures with constraints on overall and individual member instabilities. *Finite Elements in Analysis and Design*, 141, pp.119-134.
5. **Changizi, N.** and Jalalpour, M., 2017. Robust topology optimization of frame structures under geometric or material properties uncertainties. *Structural and Multidisciplinary Optimization*, 56(4), pp.791-807.
6. **Changizi, N.**, Kaboodanian, H. and Jalalpour, M., 2017. Stress-based topology optimization of frame structures under geometric uncertainty. *Computer Methods in Applied Mechanics and Engineering*, 315, pp.121-140.
7. **Changizi, N.** and Jalalpour, M., 2017. Stress-based topology optimization of steel-frame structures using members with standard cross sections: Gradient-based approach. *Journal of Structural Engineering*, 143(8), p.04017078.